TIME-DOMAIN TERAHERTZ SPECTROSCOPY AND ITS APPLICATION TO THE STUDY OF HIGH-T_c SUPERCONDUCTOR THIN FILMS

DISSERTATION

zur Erlangung des Doktorgrades
des Fachbereichs Physik
der Universität Hamburg

vorgelegt von
Maxim A. Khazan
aus Sankt-Petersburg

Hamburg

2002

Gutachter der Dissertation: Prof. Dr. J. Kötzler

Prof. Dr. P. Schmüser

Gutachter der Disputation: Prof. Dr. J. Kötzler

Prof. Dr. U. Merkt

Datum der Disputation: 16.04.2002

Dekan des Fachbereichs Physik und

Vorsitzender des

Promotionsausschusses: Prof Dr. Fr.-W. Büßer

Abstract

The work presents the creation of a time-domain THz instrumentation that enables broadband measurements of complex material functions of both bulk samples and thin films in the frequency range from 100 GHz to 2.5 THz at temperatures 20-300 K. Among other original solutions, a novel convertible scheme has been realized. It allows experiments in classical transmission configuration, as well as THz reflection measurements with quick and easy change of incidence angle of THz radiation from 25 to 80 degrees. Various ways to overcome the problem of phase uncertainty are also proposed and tested. The convertible scheme can serve as a basis for new THz arrangements, e.g., for a time-domain THz ellipsometer.

The setup has been applied to the study of complex THz transmittance of high-T_c superconductor thin films. The measured data on $YBa_2Cu_3O_{6.95}$ films were analyzed in the framework of the two-fluid Drude-London model. The results on $Tl_2Ba_2CaCu_2O_8$, however, were impossible to fit with classical Drude expressions with one frequency-independent scattering rate. The material also exhibited unexpectedly high surface resistance at the frequencies around 1 THz and higher. Moreover, the real part of dielectric function turns positive at higher THz frequencies at $T < T_c$. Above the transition temperature, it stays positive in the whole frequency range of our spectrometer. The phenomenon was also observed with conventional IR spectroscopic means and is probably caused by unusually high phonon contribution to the dielectric permittivity of the material.

Kurzfassung

In dieser Arbeit wird der Aufbau eines Terahertzspektrometers vorgestellt, das zeitaufgelöste, breitbandige Messungen komplexer Materialfunktionen im Frequenzbereich von 100 GHz bis 2.5 THz und bei Temperaturen von 20 bis 300 K ermöglicht. Neben weiteren originären Lösungen wurde ein flexibler Aufbau

realisiert, der sowohl Experimente in klassischer Transmissions-Anordnung als auch THz-Reflektions-Messungen erlaubt. Dabei kann der Einfallswinkel der THz-Strahlung schnell und einfach zwischen 25° und 80° variiert werden.

Verschiedene Verfahren zur Kompensation der Phasenungenauigkeit werden vorgeschlagen und experimentell überprüft. Dieser Aufbau, den wir „Konvertierbares Terahertzspektrometer" genannt haben, kann als Basis für weitere neue Terahertztechniken wie z.B. Terahertzellipsometrie dienen.

Das Spektrometer wurde zur Messung der komplexen Transmission von dünnen Filmen aus Hochtemperatursupraleitern benutzt. Die Daten für $YBa_2Cu_3O_{6.95}$ wurden im Rahmen der Drude-London Zweiflüssigkeitenmodelle analysiert. Die Leitfähigkeit von $Tl_2Ba_2CaCu_2O_8$ konnte allerdings nicht mit der klassischen Drude Formel mit frequenzunabhängiger Streurate gefittet werden. Das Material zeigt auch unerwartet hohe Werte des Oberflächenwiderstands bei Frequenzen um 1 THz und höher. Darüber hinaus wird der reale Teil der dielektrischen Funktion für $T < T_c$ positiv bei hohen Terahertzfrequenzen. Oberhalb der Übergangstemperatur bleibt es positiv im ganzen Frequenzbereich unseres Spektrometers. Das Phänomen wurde auch mit Hilfe der konventionellen Infrarotspektroskopie beobachtet und wird wahrscheinlich von einem ungewöhnlich hohen Phononenbeitrag verusacht.

CONTENTS

I. INTRODUCTION

After their advent in the mid-1960s[1], there has been a spectacularly rapid progress in ultrafast lasers[2] over the last four decades (Fig. I.1). Together with the successes in semiconductor technology and non-linear optics it has lead in 1970s to the birth of a new area of applied physics known as optoelectronics or photonics.
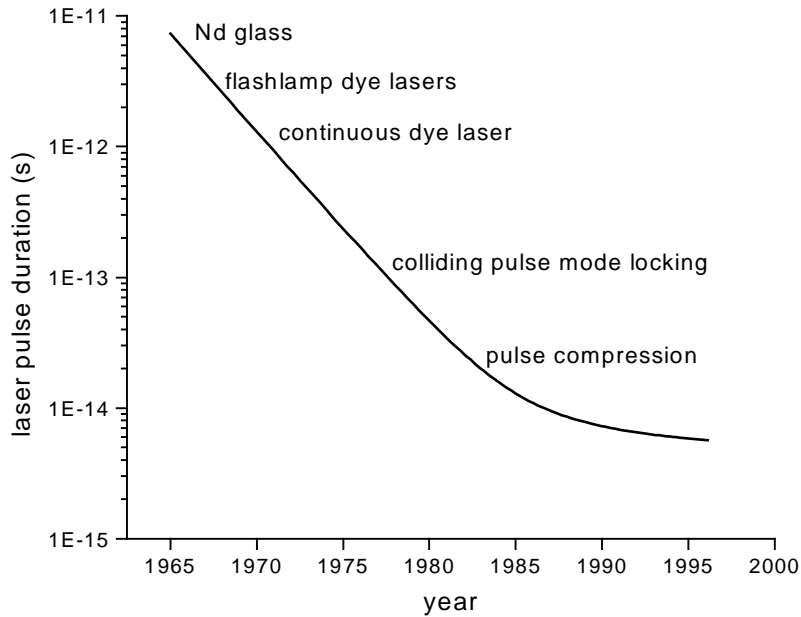
Fig. I.1. *Progress in ultrafast lasers: laser pulse width versus year.*

One of the most fascinating photonic spectroscopic applications, the time-domain terahertz spectroscopy (TDTS), is now barely 15 years old. It has appeared in mid 80s in the pioneering works of D.H. Auston and coworkers[3,4] and has become a technique applicable to materials research in early 90s[5,6]. Now TDTS is a rapidly developing measurement technique constantly finding new applications in various areas of materials science such as precise gas sensing[7,8] and measurements of material constants of solids ranging from ferroelectrics[9] to semiconductors[10] and superconductors[11,12]. In some areas like investigation of very hot samples, e.g. flame, TDTS is the only applicable far-infrared spectroscopic technique[13]. Far infrared imaging based on TDTS is currently an extremely promising way of non-destructive method for testing samples from packaged goods to artworks and biological tissues[14].

Terahertz (1 THz $= 10^{12}$ Hz) frequencies i.e. frequencies from tens of GHz to few THz, lay between the operation ranges of classical microwave and infrared spectroscopy (Fig. I.2) and thus cannot be effectively covered by any of these techniques. TDTS fills this gap enabling the study of materials properties in the part of the electromagnetic spectrum that is of a particular interest for the materials science.

As the TDTS is a new measurement technique, today's market of scientific instruments cannot offer a reasonably priced time-domain THz spectrometer. On the contrary, such systems throughout the world are normally hand-made and are a subject of constant development and improvement.

The main goals of this doctoral work was the creation of a reliable time-domain THz spectrometer applicable for the use in various areas of materials research and the study of high-T_c superconductor (HTS) thin films by the means of TDTS.

Properties of HTS at THz frequencies are of great interest, both from the point of view of the fundamental and applied research. In HTS, the quasi-particle scattering rates fall into the THz frequency range at temperatures below the T_c. The interest to HTS at THz frequencies is also stimulated by needs of the perspective THz electronics applications[15]. In this sense HTS are interesting rather in the form of thin films than bulk pieces.

A number of promising HTS materials still have their superconductivity characteristics scarcely explored in the THz range e.g. the Tl-Ba-Ca-Cu-O (TBCCO) system. Furthermore, there is a lack of data on their phonon spectra in the range. At THz frequencies, thallium cuprates exhibit some unusual properties which are especially clear observable at temperatures near and above T_c. Being good conductors they nevertheless reveal very strong dielectric contribution to the complex conductivity.

Study of the patterned high-T_c superconductor thin films is a new and extremely exciting area of research. Patterned structures characterized by the dimensions which are comparable to or shorter than the phase coherence length of the superconducting

or normal conducting carriers exhibit properties which are different from those of solid films. These are so-called *mesoscopic* effects[16,17]. The observation of mesoscopic phenomena in superconductors requires in principle samples with pattern dimensions as small as nanometer. However, due to the rapid decrease of the quasiparticle scattering rate in cuprate superconductors below the T_c the mean free path of unpaired carriers reaches 100-1000 nm in the ab-plane. Therefore, one can expect the mesoscopic effects to appear already in micrometer-patterned films.
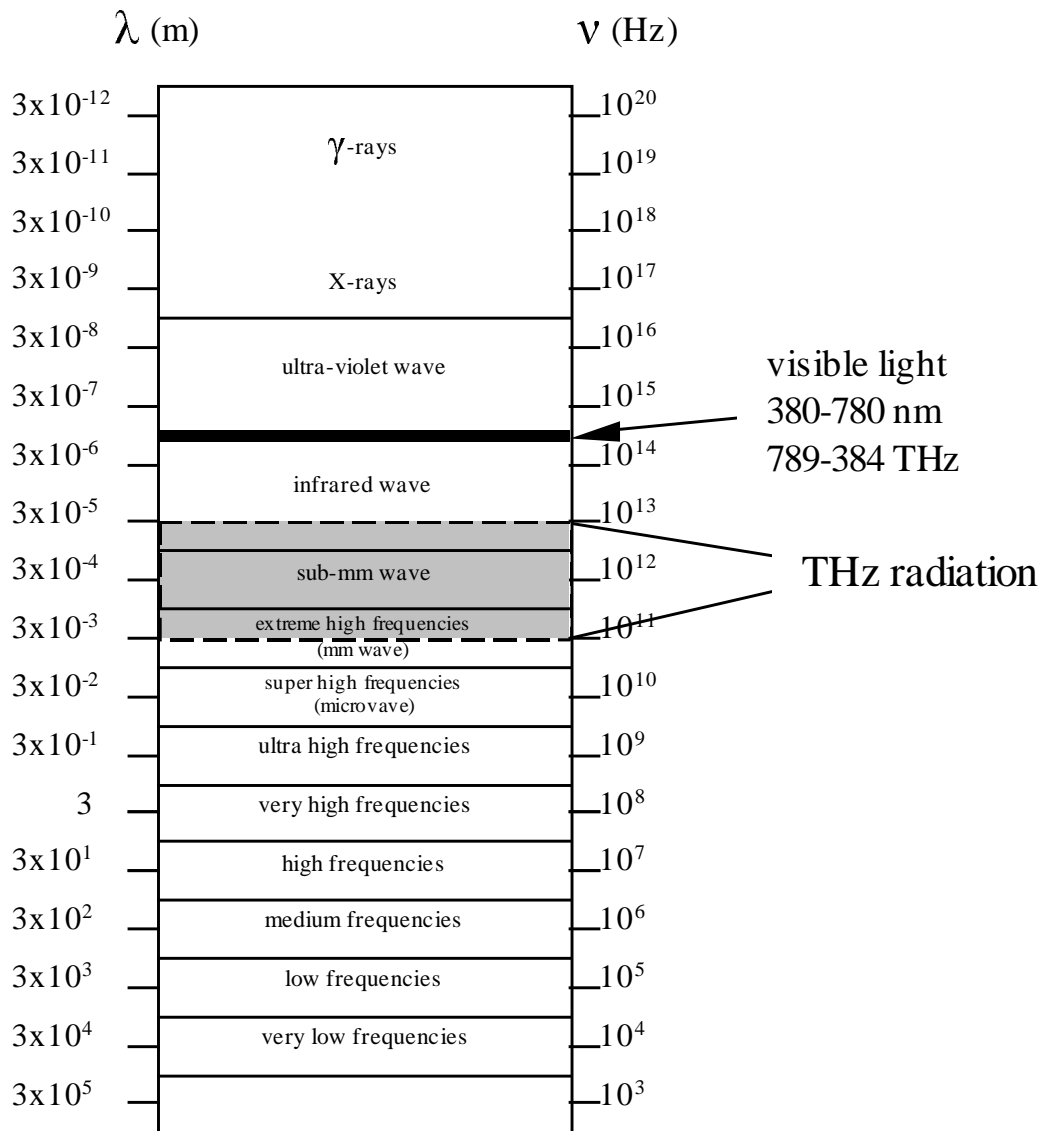
Fig. I.2. *Frequency scale of electro-magnetic radiation. The THz range (100 GHz – 10 THz) is shown gray, the black stripe corresponds to the visible light region.*

On the other hand, patterned high-T_c thin films (mostly YBCO) are already used in passive[18] and active microwave electronic devices. Now, the requirements of fast developing THz electronics[15] stimulate the study of the properties of patterned HTS thin films in the THz region of electromagnetic spectrum.

The accomplishment of the first main task i.e. the development of a reliable time-domain THz instrumentation required a solution of the experimental and theoretical problems which were secondary for this work but are in fact very exciting topics of their own:

- THz beams have distinct spatial distribution of frequencies and therefore the propagation of THz radiation cannot be described in the framework of the plane-wave formalism. Various optical elements like apertures, lenses and mirrors strongly affect temporal shapes and spectra of detected THz pulses and the proper understanding of this influence is of crucial importance for the correct interpretation of the results measured. Our model of spatio-temporal transformations[19] of THz pulses is based on the Gaussian beam formalism and allows us to take into account the contributions of the focusing elements used in the spectrometer.

- To elaborate a stable working procedure for the extraction of the complex refractive index spectra of HTS thin films from measured transmission data was one more task to fulfill. So far, various *a priori* approximations e.g. thin film approximation have been used. However, high values of the refractive index of HTS materials drive us out of the applicability range of the approximations. The purely numerical approach used by us allows to drop the approximations and enables the study of thicker and/or more conductive films.

- Inspired by the needs of THz and far-infrared spectroscopy, which widely use wire grids as polarizers and beam splitters we have investigated the complex transmittance of free-standing tungsten wire grids. The analysis of the results was for us also a first step to the understanding of the transmissive behavior of patterned HTS thin film structures.

Structuring of the text

This dissertation consists of two major parts. The first part (Chapters II – VI) presents the work on the creation of time-domain THz spectrometers and the development of THz spectroscopic methods. The second part (Chapter VII) is devoted to the applications of the means of TDTS to the study of superconductor thin films and patterned metallic and superconducting structures.

In Chapter II, the basic principles of the time-domain THz spectroscopy are highlighted.

Chapter III describes the elaboration of an effective emitter of pulsed THz radiation including testing of various semiconductor materials for unbiased (Section III.2) and biased (Section III.3) emitters.

Detection of THz radiation with photoconducting antennas and electro-optic sampling is the topic of Chapter IV. The electro-optic sampling system built in our laboratory is described in detail in the diploma thesis of H. Selig[20] and therefore I give here only a brief overview of it.

Chapter V is devoted to the elaboration of time-domain terahertz spectroscopic instrumentation. A description of basic elements of a THz spectrometer is given in Section V.1. First, a transmission spectrometer with classical general layout has been built (Section V.2). After that, I have proposed and realized a completely new flexible scheme enabling a swift conversion of a THz spectrometer from transmission to reflection configuration and changing of the incidence angle of THz radiation (Section V.3). The outcome of this work has been published in Ref. 21.

Chapter VI presents the study of spatio-temporal transformations that have been performed in Prague at the Institute of Physics, Academy of Sciences of the Czech

Republic[*] under the guidance of Dr. Petr Kužel and resulted in publication of Ref. 19.

Chapter VII presents materials science applications of TDTS. It begins with the description of the time-domain data treatment procedure including the ways to avoid the misinterpretation of measured data (Section VII.1). In Section VII.2 the TDTS is applied to the study of complex conductivity of thin HTS films. Some of its results have been reported in Ref. 22. The study of the transmissive behavior of free-standing tungsten wire grids and striped YBCO thin films at THz frequencies is presented in Sections VII.3. and VII.4, respectively.

Finally, after the general conclusions of this work (Chapter VIII), possible directions of the future work and some perspective projects including the first time-domain THz ellipsometer are outlined in Chapter IX.

---

[*] Fyzikální ústav Akademie věd České republiky, Na Slovance 2, 182 21 Praha 8, Czech Republic

List of abbreviations

CTRTS	convertible transmission-reflection THz spectrometer
EMA	effective medium approximation
EOS	electro-optic sampling
Eq(s).	equation(s)
HTS	high-transition-temperature superconductor
(F)IR	(far-)infrared
MW	microwave-
PDA	photoconducting dipole antenna
RTDTS	reflection time-domain terahertz spectroscopy
SNR	signal-to-noise ratio
TDTE	time-domain terahertz ellipsometer
TDTS	time-domain terahertz spectroscopy
TTDTS	transmission time-domain terahertz spectroscopy

II. PRINCIPLES OF THE TIME-DOMAIN THZ SPECTROSCOPY

The basic idea of the transmission time-domain THz spectroscopy (TTDTS) can be described in the following way: a sub-picosecond pulse of electromagnetic radiation passes through a sample and gets its time profile changed compared to the one of the reference pulse. The last can be either a freely propagating pulse or a pulse transmitted through a medium with known properties. Through an analysis of changes in the *complex* Fourier spectrum which are introduced by the sample, the spectrum of the refractive index of the sample's material is obtained.

If we denote the Fourier transforms of the measured time profiles of the pulse transmitted through a sample and the reference pulse as $E^*(\omega)$ and $E_{ref}^*(\omega)$, respectively, then we have the complex transmittance of the sample in the form:

$$T^*(\omega, n(\omega)) = \frac{E^*(\omega, n^*(\omega))}{E_{ref}^*(\omega)} \qquad \text{(II.1)}$$

The Eq. (II.1) is then solved in order to obtain the frequency dependence of the complex refractive index $n^*(\omega)$. The procedure will be described in detail in the Section VII.2.1.

Fig. II.1 gives an example of the determination of the complex refractive index by means of TDTS. In the panel (a) the measured THz waveforms are shown. The pulse transmitted through a 0.3 mm thick silicon wafer (dashed) is smaller in amplitude and shifted in time with respect to the freely propagating pulse (solid line). The equidistant satellites which follow the main transmitted pulse originate from the multiple reflections of THz radiation within the silicon wafer. These reflections are also responsible for the Fabry-Perot oscillations in the amplitude spectrum (panel (b)). The ratio of the complex spectra of the pulses gives according to Eq. (II.1) the complex transmittance of the sample which is shown in the panel (c). Then the solution of Eq. (II.1) yields the complex refractive index $n^*(\omega)=n(\omega)+ik(\omega)$ (panel (d)).

For samples, characterized by very low transmittance at THz frequencies, the use of the transmission time-domain terahertz spectroscopy (TTDTS) becomes problematic. In such cases, the reflection time-domain THz spectroscopy (RTDTS) can be employed. The complex *reflectance* of a sample is expressed by the equation:

$$R^*(\omega, n^*(\omega)) = \frac{E^*(\omega, n^*(\omega))}{E_{ref}^*(\omega)} , \qquad\qquad (II.2)$$

where $E^*(\omega)$ and $E_{ref}^*(\omega)$ are this time the Fourier transforms of the pulses reflected from a sample and a reference surface, respectively. The complex refractive index $n^*(\omega)$ is then extracted through solution of Eq. (II.2). The specific problems of RTDTS will be discussed later in Section V.3.
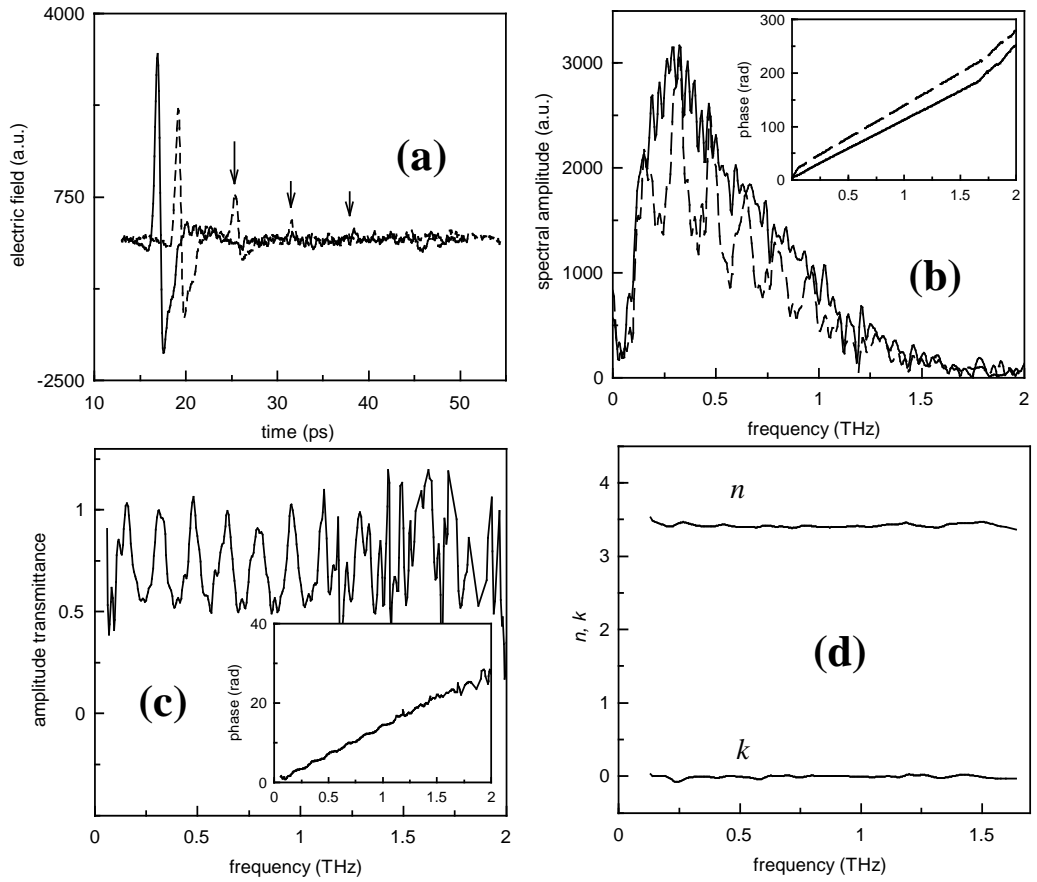
Fig. II.1 *From time profiles to complex refractive index. (a) THz waveforms: a freely propagating pulse (solid line) and a pulse transmitted through a 0.3 mm thick silicon wafer (dashed line). Arrows mark multiple reflections of the THz pulse within the wafer, (b) corresponding complex Fourier spectra, (c) complex transmittance of the sample, (d) calculated real and imaginary parts of the complex refractive index n*=n+ik. Strong oscillations in amplitude spectra and the transmittance are caused by the multiple reflections in the sample.*

17

TDTS operates with pulses of electromagnetic radiation which are too short to be resolved by conventional electronic display instruments like oscilloscopes. Instead, so-called gated-detection technique is employed (see the scheme in Fig. II.2). The THz spectrometer is powered by a laser which emits a train of pulses each of several tens of femtoseconds (1 fs = 10^{-15} s) in duration. The initial laser beam is split by a beam splitter in two parts called pump and probe beams. A pump pulse hits an emitter which in response releases a short (few picoseconds) pulse of electromagnetic radiation. The spectrum of the radiation is centered at several hundreds of GHz (1 GHz = 10^9 Hz) so that one- or even half-cycle pulses are released. This THz radiation then comes to a detector which is gated by a probe pulse. The output signal of the detector is proportional to the magnitude and the sign of the field of the THz pulse in every certain moment of time. Thus, by the variation of the delay between pump and probe optical pulses one can trace the whole time profile of the THz pulse.

In the following (Chapters III-VI), various ways of generation and detection of pulsed THz radiation, the study of the specifics of the THz beam optics, and different THz spectrometer arrangements are presented.

Detector: optical or electrical response measured

Emitter

Pump

THz beam
$100 \ \mu m \leq \lambda \leq 10 \ mm$
$t_p \leq 5 \ ps$

Data aquisition

Probe

delay: τ

Ti:Sapphire Laser

Optical laser beam
$\lambda = 800 \ nm$
$t_p = 50 \ fs$
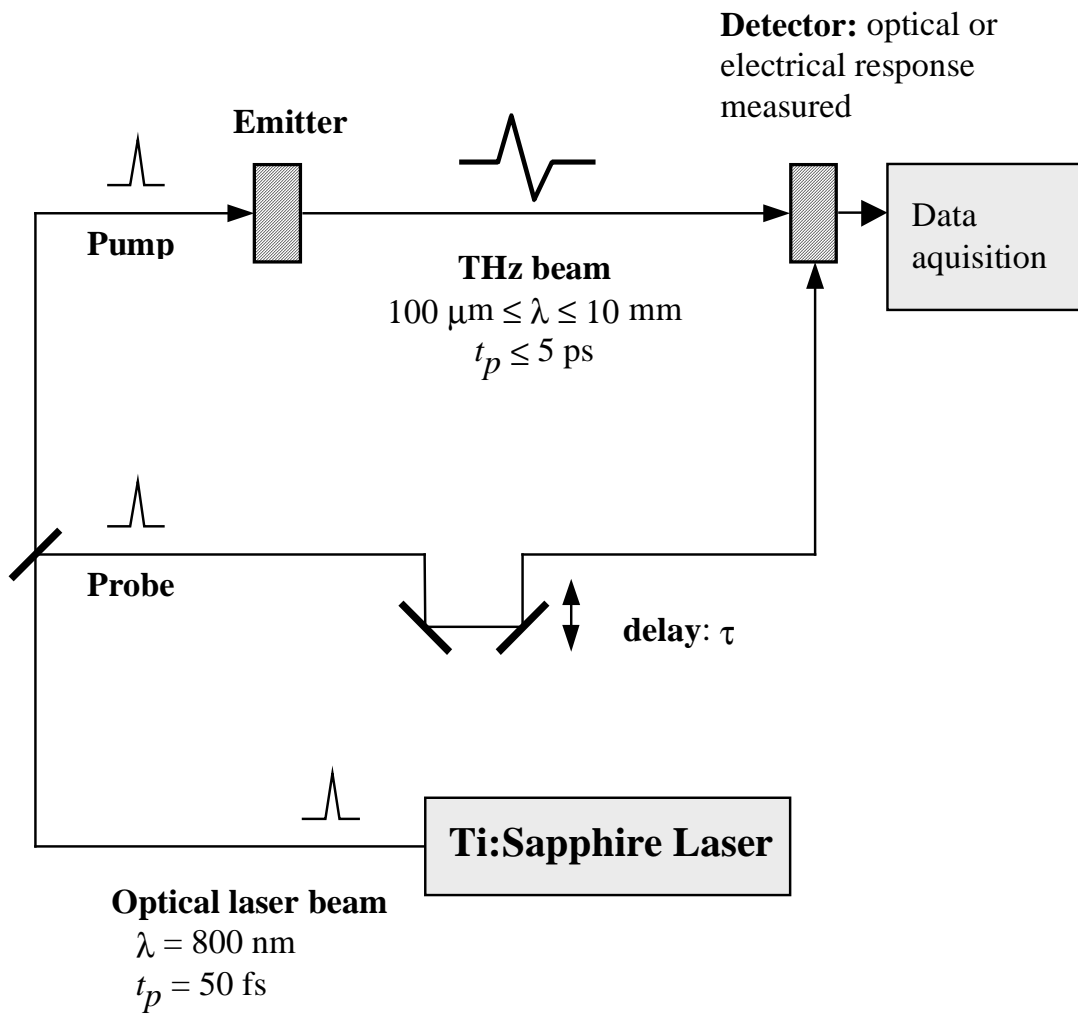
Fig. II.2 *The gated-detection scheme. λ is wavelength and t_p is pulse duration (of either laser or THz pulse).*

III. GENERATION OF SUB-PICOSECOND THZ PULSES

III.1. Introduction

Starting from the mid - 80s, a variety of materials was reported to emit subpicosecond THz pulses. Two rather distinct mechanisms have been used most widely for the generation of such pulses: optical rectification in crystals with large second order nonlinearity, like $LiTaO_3$[23] or DAST[24] and transient photoconductivity. A somewhat less popular generation method is, for example, difference frequency generation in non-linear media[25]. Some other non-linear phenomena like a Cherenkov-like propagation of a short electrical pulse can also result in emission of THz radiation[26]. Various quantum oscillations like Bloch oscillations[27], heavy-hole-light-hole beats[28] or oscillations in double-quantum-well structures[29] can also result in emission of THz radiation. Although some quantum oscillations can provide tunable THz radiation,[30] the production of quantum well structures is complicated and therefore they are barely used in THz spectrometers. THz radiation from superconducting thin films[31] is interesting rather from the point of view of basic research than spectroscopic applications. The reported THz radiation from unbiased helium gas[32] and photoionized electrically biased air[33] can give rise to a new generation of THz emitters.

For our spectrometers, we chose semiconductor emitters whose operation principle is transient conductivity. The transient photoconductivity methods for the generation of pulsed THz radiation are based on high-intensity ultrashort laser pulses exciting the surface of either unbiased[34,35,36] or biased semiconductor[37,38]. In both cases THz radiation arises from the fast change of the photocurrent in the semiconductor. The change is caused by the acceleration and the following recombination of photocarriers generated by a pump optical pulse. The acceleration is driven by the electric field which is either a built-in surface depletion field for unbiased emitters or is externally applied in the case of biased ones.

The photon energy of the laser must be sufficient for the excitation of photocarriers over a bandgap. For example, the typical central wavelength of a Ti:sapphire laser is around 780 nm which corresponds to the photon energy of 1.56 eV that is enough to generate photocarriers through a direct interband transition in GaAs (E_{g300K}(GaAs) = 1.43 eV [Ref. 39]).

The electric field strength of an emitted pulse in far field in the Hertzian dipole model has the form[40]:

$$E \propto \int \frac{1}{R} \sin \varphi \frac{d^2 p}{dt^2} dx dy, \qquad \text{(III.1.1)}$$

where φ is the angle between the dipole moment p and the propagation direction and R is the distance from the dipole and the observation point. The integration is taken over the whole emitting area. Knowing that $p = lq$, where q is the dipole's separated charge (i.e. the charge of a photocarrier) and l is a mean free pass of photocarriers we can write:

$$\frac{d^2 p}{dt^2} = l \frac{d^2 q}{dt^2} = l \frac{dj}{dt}, \qquad \text{(III.1.2)}$$

where j is a photocurrent. Finally, III.1.1 and III.1.2 give:

$$E \propto \int \frac{l}{R} \sin \varphi \frac{dj}{dt} dx dy, \qquad \text{(III.1.3)}$$

Although semiconductor emitters are usually operated at room temperature, their effectiveness increases under cryogenic cooling due to the grow of carriers mobility[41]. There have also been some successful attempts to boost their performance by application of a strong magnetic field[42].

As the intensity of the radiated field is proportional to the time derivative of photocurrent, it is obviously preferable to use materials which react fast on the excitation with ultrashort laser pulse. The rise time of the photocurrent is very short

(tens of femtoseconds) and is limited only by the uncertainty principle, the excitation laser pulse duration, and the probability that the electron-hole pair escapes its mutual coulomb attraction, which is in most high-mobility semiconductors close to 100%. On the other hand, the decay of the photocurrent is significantly slower (from hundreds of ps to milliseconds for pure crystals) being influenced by a number of effects, mainly by electron-hole recombination and carrier trapping on defects. The introduction of defects which play the role of recombination centers and traps can be carried out by doping a semiconductor with heavy impurities e.g. metals, radiation damage or the use of materials characterized by a high density of naturally occurring defects. An excellent example of the last class of THz emitter materials is so-called low-temperature grown GaAs or LT-GaAs. However, the main drawback of materials with extremely high density of defects like for instance amorphous semiconductors[43] is the suppression of carrier mobility (down to few cm^2/Vs) due to intensive elastic scattering on the defects.

III.2. Semiconductor surface emitters

In an unbiased surface emitter, the photocarriers generated by a laser pump pulse are accelerated in the surface depletion field of a semiconductor. The depletion field is caused by the "pinning" of Fermi level at the semiconductor-air interface which results in bending of both the valence band and the conduction band and thus the formation of a depletion layer (Fig.III.2.1). The photoinjected electrons and holes are swept across it so that the photocurrent first rises fast and then vanishes as the photocarriers recombine.

THz radiation is emitted from a semiconductor surface in both reflection and transmission directions (Fig. III.2.2). The photogenerated electrons and holes can be described in the framework of the Hertzian dipole model[44]. Assuming also the plane wave approximation, we obtain the electric fields of radiated waves in the form:
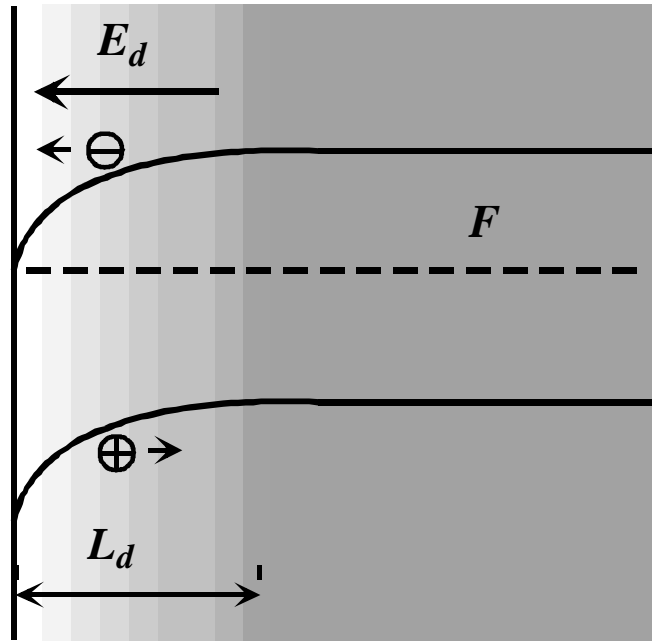
Fig. III.2.1. Semiconductor band diagram near the surface. The "pinning" of the Fermi level near the semiconductor-air interface leads to the formation of a depletion layer with the depth L_d. E_d is the strength of the built-in depletion electric field and F is the Fermi level. Graded gray filling symbolizes the lowered concentration of carriers near the surface.
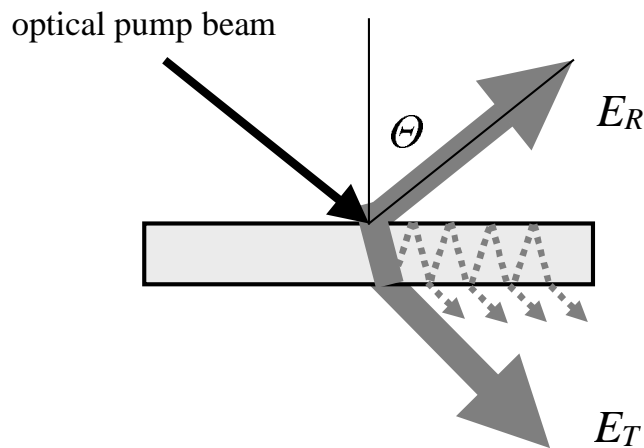
Fig. III.2.2. Semiconductor surface THz emitter. E_T and E_R are electric field of the THz radiation emitted in the transmission and reflection directions, respectively. Dashed lines indicate the paths of the multiple reflections of the THz radiation within the emitter wafer.

$$E_R = ZJ_S \frac{\sin \Theta}{\cos \Theta + (1/n^2)\sqrt{n^2 - \sin^2 \Theta}} \tag{III.2.1}$$

$$E_T = -T(\Theta)(1/n)E_R$$

where E_R and E_T are electric field strength of the THz wave radiated in reflection and transmission directions, Z and n are the impedance and the refractive index of the emitter material, Θ is the incidence angle of the pump beam, J_S is the photocurrent through the depletion layer, and $T(\Theta)$ is the transmissivity of the semiconductor/air interface. The photocurrent J_S is given by the expression:

$$j_S = \frac{\mu e}{h\nu} W_{op} [1 - R(\Theta)] \cos \Theta \int_0^\infty E_d(x)e^{-\alpha x}dx , \tag{III.2.2}$$

where μ is the photocarrier mobility, e is the elementary charge, $h\nu$ is the energy of incident photons, W_{op} is the optical intensity, $R(\Theta)$ is the reflectivity of the surface at the laser frequency, $E_d(x)$ is the surface depletion field, and α is the optical absorption length.

III.2.1. Testing the emitter materials

In order to find a semiconductor material that would manifest the strongest THz emission from its surface, several surface emitters have been tested: In our spectrometers we employed unbiased semiconductor surface emitters: semi-insulating undoped GaAs (SI GaAs) with three different surface orientations and chromium-doped GaAs, iron-doped semi-insulating InP (SI InP), and low-temperature grown GaAs (LT-GaAs). Parameters of the emitter materials studied by us are summarized in Table III.1.1. The time-domain THz spectrometer created for the testing of the emitter materials is depicted in Fig. III.2.1.1.

At it is seen in Table III.2.1.1 and Fig. III.2.1.2, surface orientation of the emitter wafer has significant influence neither on the intensity of emitted THz radiation nor

on the shape and spectrum of pulses. Iron-doped InP with the <100>-oriented surface has manifested itself as the best of the tested emitter materials. Although it is characterized by somewhat lower mobility of carriers, the reduction of their lifetime due to the scattering on Fe impurity atoms results in the stronger THz emission. LT-GaAs is beaten by both SI-GaAs and InP:Fe, in the first case due to lower mobility and probably the weaker surface depletion field $E_d(x)$ in both cases. However, when a strong external bias field is applied, the latter drawback is overridden and LT-GaAs turns one of the best material for biased THz emitters (this will be explained in detail in Sections III.3).

Table III.2.1.1. *Semiconductors as emitters of THz radiation*

wafer material	surface orientation	band gap E_g (eV)	Mobility μ (cm^2/Vs)	decay time τ_c(ps)	peak frequency of THz emission (surface)
SI GaAs	<100>		8500 [Ref.45]	~10^3 [Ref. 45]	0.45
SI GaAs	<110>	1.43			0.47
SI GaAs	<111>				0.507
LT-GaAs	---		2250-3000 [Ref. 46]	0.2-3 [Ref. 46]	0.62
GaAs:Cr	<100>		~2000 [Ref. 47]	300 [Ref. 47]	---
InP:Fe	<100>	1.29	2200 [Ref. 47]	150-1000 [Ref. 47]	0.38
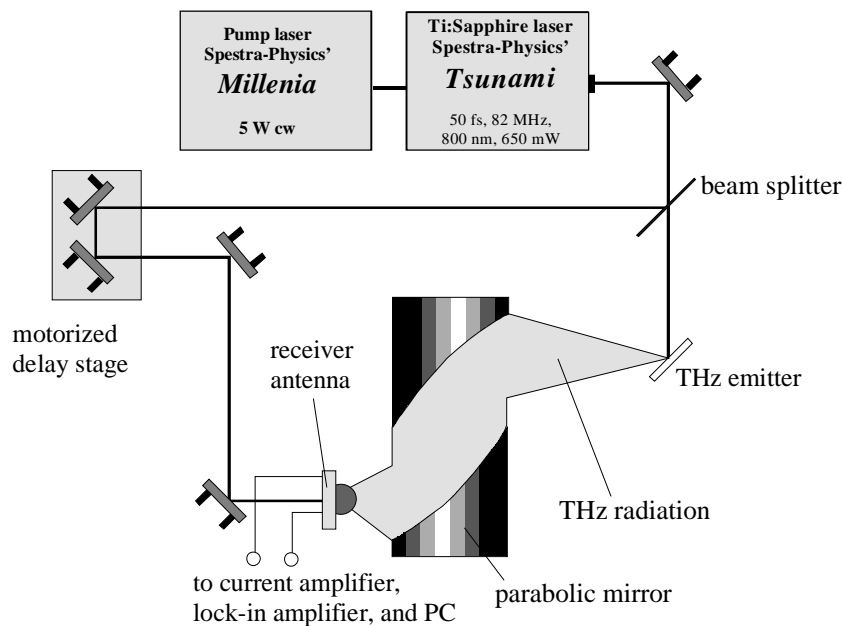
Fig. III.2.1.1. The initial configuration of the time-domain THz spectrometer intended for

Fig.III.2.1.2. *(a) Time profiles (main pulses, multiple reflections within the emitter cut away) and (b) amplitude spectra of THz pulses generated by semiconductor surface emitters at the pump beam incidence angle of 45°.*
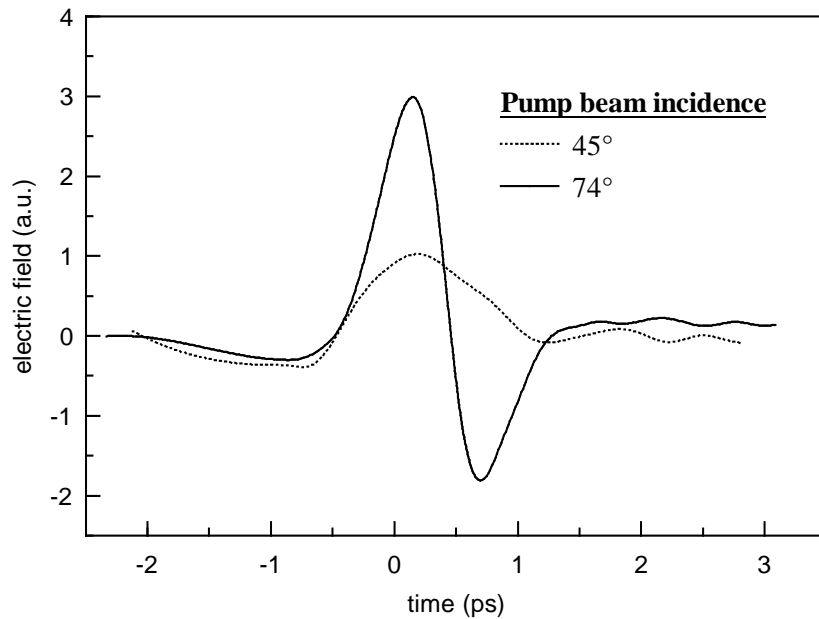
Fig. III.2.1.3. *THz pulses emitted from the GaAs wafer surface at the pump beam incidence angles of 45° and ~74° (Brewster angle).*

A further improvement of the performance of surface emitters can be achieved by the choose of an appropriate incidence angle for the optical pimp beam. In the original configuration of the spectrometer (Fig. III.2.1.1) the angle was set on 45° for the sake of geometrical simplicity. But the analysis of the Eq. III.2.1 shows that the maximum of THz radiation efficiency is reached at the Brewster angle incidence[35,48] which is around $74.8°$ at $\lambda = 800$ nm and $74.5°$ at $\lambda = 300$ μm for GaAs and $73.9°$ at $\lambda = 800$ nm and $74.2°$ at $\lambda = 300$ μm for InP[49]. In Fig. III.2.1.3 the pulses emitted at two different pump incidence angles are presented. It is seen that the pulse emitted from the emitter illuminated at Brewster angle is of the highest intensity.

The emitted radiation spectrum almost does not change with temperature but the peak value of the radiated pulses falls monotonically with increasing emitter temperature[35]. To prevent the decrease of the emitters efficiency due to their overheating by the pump optical beam, they were attached to a brass block so that the temperature was constantly held around 30°C.

III.3. Large-aperture dc-biased semiconductor emitters

Surface emitters described in the previous section are easy to use since they require neither any additional devices like e.g. bias voltage supply nor precise adjustment of the pump optical beam. Their main disadvantage, however, is relatively low intensity of emitted THz radiation which makes necessary the use of highly sensitive detectors. Moreover, one can use only oblique incidence angles since, according to (III.2.1), there is no emission at normal incidence. Thus, satellite pulses originated from internal reflections within the emitter wafer (see Fig. III.2.2) are spatially separated. As a consequence, they travel through the spectrometer the other optical paths than the main pulse which makes the mathematical procedure of multiple reflection subtraction inapplicable. It means that measured time profiles must be cut before the first reflection. As it will be seen in Section VII.1.4, this lowers the frequency resolution of the spectrometer.

Biased emitters are free from this drawback because they are basically set to the normal incidence of the optical pump beam (see Fig.III.3.1). Moreover, the emitted radiation should be stronger than in the case of unbiased surface emitters thank to the possibility to externally apply a bias much higher than the depletion-layer field.
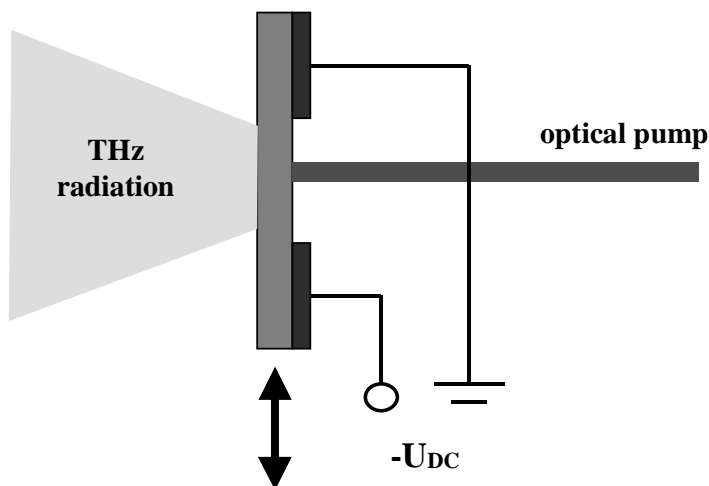
Fig. III.3.1. Schematics of a biased semiconductor emitter. The arrow shows the direction of the lateral scan (see Section III.3.3 for explanation).

28

III.3.1. Ideal biased emitter

For the description of the operation of large-aperture photocoducting switches we rely on the *current surge* model of the dynamics of photoinjected carriers (Ref. 41). The model assumes that the transient surface conductivity grows rapidly when the emitter is excited by a sub-ps optical pulse:

$$\sigma_s(t) = \frac{e(1-R)}{h\nu} \int_{-\infty}^{t} dt' \mu(t-t') I_{opt}(t') e^{-\frac{t-t'}{\tau_c}} ,$$ (III.3.1.1)

where R is the optical reflectivity of the illuminated area, $\mu(t)$ is the carrier mobility, $I_{opt}(t)$ is the optical pump pulse intensity, $h\nu$ is the photon energy, and τ_c is the lifetime of the excited carriers. Or, for the peak surface conductivity:

$$\sigma_s(t) = \frac{e(1-R)}{h\nu} \mu_1 F_{opt} ,$$ (III.3.1.1a)

where μ_1 is the value of the time-dependent mobility at the moment of maximum σ_s and F_{opt} is the incident optical fluence.

In reality, the response of the photoconductor is slower than the rise time of the intensity of the excitation laser pulse because it takes up to several picoseconds for the transient mobility mobility $\mu(t)$ to reach its quasiequlibrium value[50].

Solving the Maxwell equations and taking into account the finite size of the emitter, one obtains for the radiated field:

$$E_{THz} = -E_{bias} \frac{\sigma_s(t)\eta_0}{\sigma_s(t)Z_0 + 1 + n} ,$$ (III.3.1.2)

where E_{bias} is the applied bias electrical field, $Z_0 = 1/\varepsilon_0 c = 376.7\ \Omega$ is the impedance of free space, and n is the refractive index of the semiconductor. By the formula (III.3.1.2), two important points should be noted:

- the radiated THz field E_{THz} should raise linearly with the increase of the applied bias voltage at least in the area of the Ohm's law validity. At very high bias fields, the field dependence of the surface conductivity σ_s have to be taken into account,

- E_{THz} increases and then saturates as the incident optical fluence grows.

III.3.2. Technical realization

A large-aperture high-voltage biased semiconductor emitter consists of a semiconductor wafer and two applied electrodes separated by a few-mm gap. We have constructed an original emitter holder (Fig. III.3.2.1) that provides good electrical and thermal contact between electrodes and the semiconductor wafer's surface which is also ensured by the use of conductive silver paint (Fig. III.3.2.1c). That is important for the stable operation of the emitter since its overheating results in drop of its resistance and consequently makes higher voltage impossible to be applied. Moreover, the decrease of the carriers mobility at higher temperatures also lowers the THz output of an emitter[51].

The electrodes are endowed with copper radiators to ensure the thermally stable operation of the emitter. The temperature of the emitter wafer is checked with a thermocouple sensor and held at 40°C. When necessary, the emitter can be cooled with a Peltier cooler integrated in a thermal radiator.

The high-voltage bias is provided by a Stanford Research Systems PS300 dc power supply.

The stripes of the silver paint are about 1 mm broader than the contact area between the electrodes and the emitter to smoothen the voltage drop between them and so to prevent the erosion of the emitter wafer due to the arc discharge through the air (Fig. III.3.2.1d)
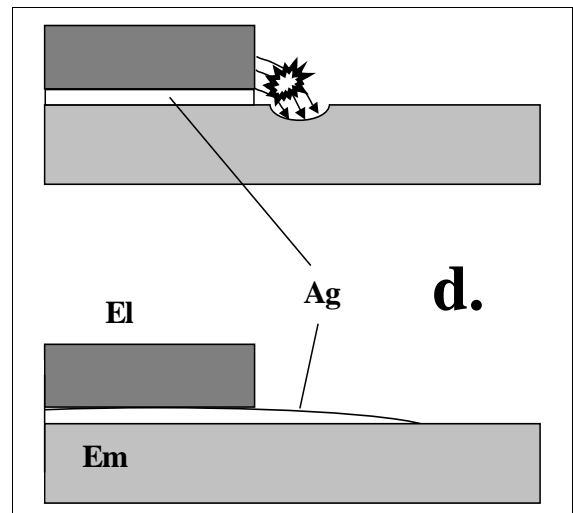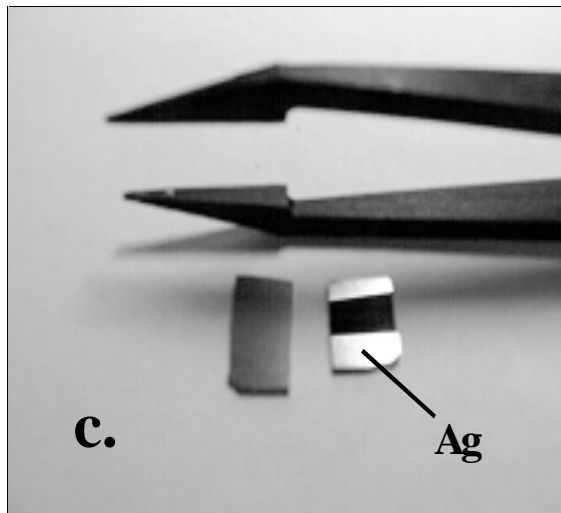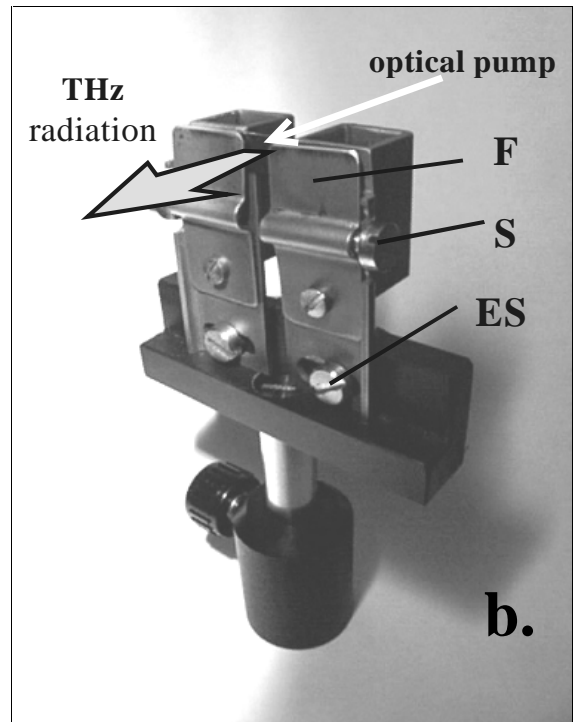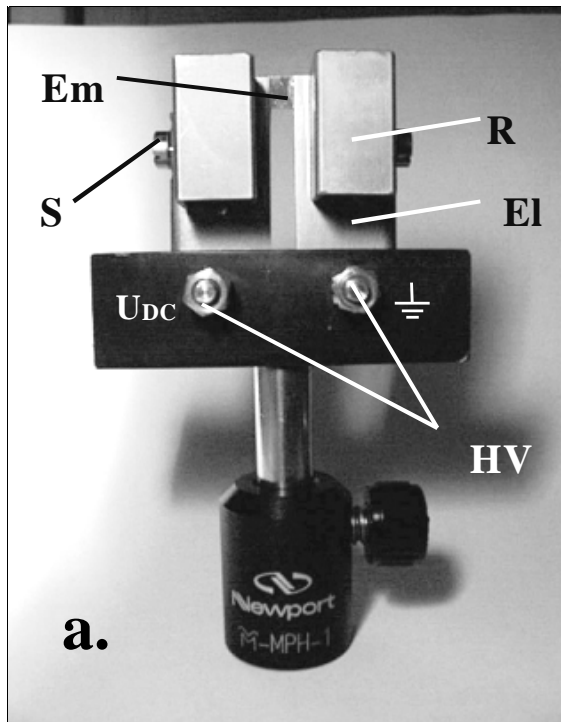
Fig. III.3.2.1. (a)-(b): the emitter of pulsed THz radiation in the holder; (c) the LT-GaAs emitter wafer with two conductive silver paint stripes. (d) erosion of the emitter due to the arc discharge and its prevention with the help of silver paint.

Legend: Em – emitter wafer, El – high-voltage electrode, R – thermal radiator, F – fixing spring, S – spring release screw, HV – high-voltage connectors, ES - electrode adjustment screw, Ag – conductive silver paint.

III.3.3. Testing the emitter materials

We have tested the performance as biased emitters of the materials previously studied as surface emitters (see Table III.2.1.1.). Much higher performance of externally dc-biased emitters compared to the surface emitters is evident from Fig. III.3.3.1. For example, the peak value of the electric field of the THz pulse emitted by a low-temperature grown GaAs (LT-GaAs) biased at 1000 V is 160 times higher than that radiated from the unbiased surface of the same wafer and is 40 times higher than in the case of an unbiased surface <100> InP emitter. On the other hand, biased emitters are set for normal incidence which allows an effective use of the procedure of multiple reflections subtraction (see Section VII.1.4).

LT-GaAs is one of the best materials for THz emitters and detectors. It is characterized by very high concentration of defects which act as traps for photocarriers so that their lifetime is reduced to few hundreds femtoseconds. This leads to a fast change of the photocurrent (rapid fall after the initial growth) which in accordance with Eq. (III.1.3) results in a stronger emission of the THz radiation and naturally in extension of its spectrum to higher frequencies compared to materials with longer living carriers like semi-insulating GaAs (SI-GaAs) and InP.
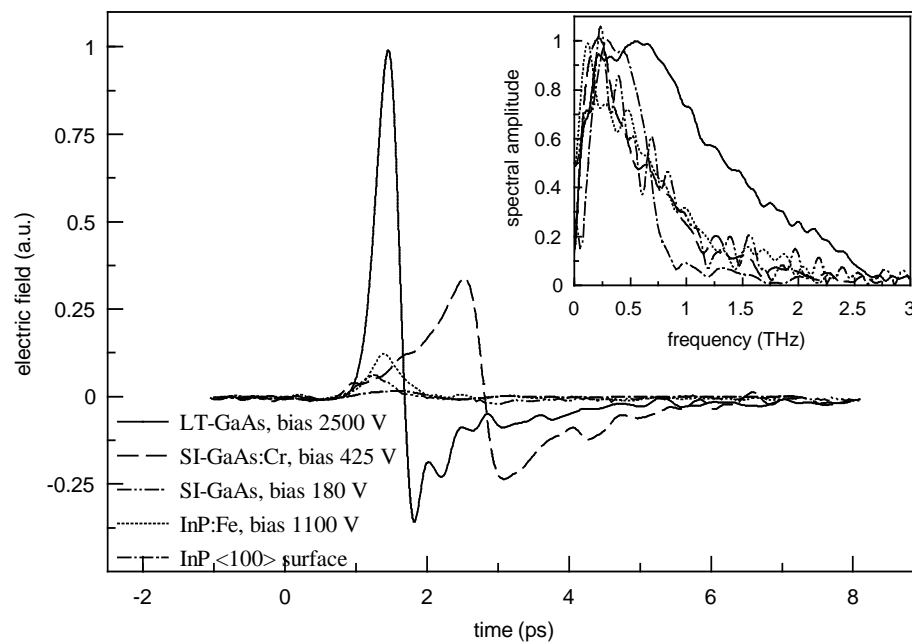
Fig. III.3.3.1. THz pulses generated by dc-biased and unbiased semiconductor emitters. Inset: normalized amplitude spectra of the pulses.

The carrier lifetime in SI-GaAs and LT-GaAs was checked by means of time-resolved optical reflectivity[52]. The free charge carriers generated by an optical pump pulse cause the growth of the sample's reflectivity tested by an optical probe pulse. As the photogenerated electrons and holes first "cool down", then thermalize, and finally recombine, the reflectivity falls back to its equilibrium value. The relaxation of charge carriers in LT-GaAs is finished within few picosecond while in InP the transient carriers persist for hundreds of picosecond, and for the undoped crystalline GaAs it takes nanoseconds or even more for the photocarriers to recombine (Fig. III.3.3.2). As a result, some fraction of the electrons and holes created with the pump pulse is still present in the sample when the next pulse arrives 12.2 ns later, i.e. there is a constant background photocurrent through the emitter wafer. The consequences of it are overheat of the emitter and quite low bias voltage that can be applied to it which all excludes pure GaAs from good candidates for THz emitter materials.

The dependences of the peak value of the electric field of the emitted THz pulses on the incident optical fluence and applied bias is depicted in Fig. III.3.3.3. In reality, a common Ti:Sapphire laser provides relatively low optical fluences (up to few tenths of $\mu J/cm^2$ at the beam diameter of around 1 mm) so that in order to observe the saturation (inset in Fig. III.3.3.3a) one needs an amplified laser with much higher pulse energy[*].

The observed dependence of E_{peak} on the applied bias field deviates strongly from the straight line predicted by Eq III.3.1.2. The $E_{peak}(U_{bias})$ curve follows the non-ohmic dependence of the photocurrent on the bias field. After the initial exponential growth comes the saturation at higher fields (> 3.5 kV/cm). The cause of the saturation is the screening of the applied bias field by the radiated THz field[53] and probably the variation of the transient mobility as a function of bias field[41]. This saturation can be even followed by a decrease at very high (>100 kV/cm) bias fields[54].

---

[*] The measurements with an amplified laser have been kindly performed by Klaas Wynne of the University of Strathclyde, UK
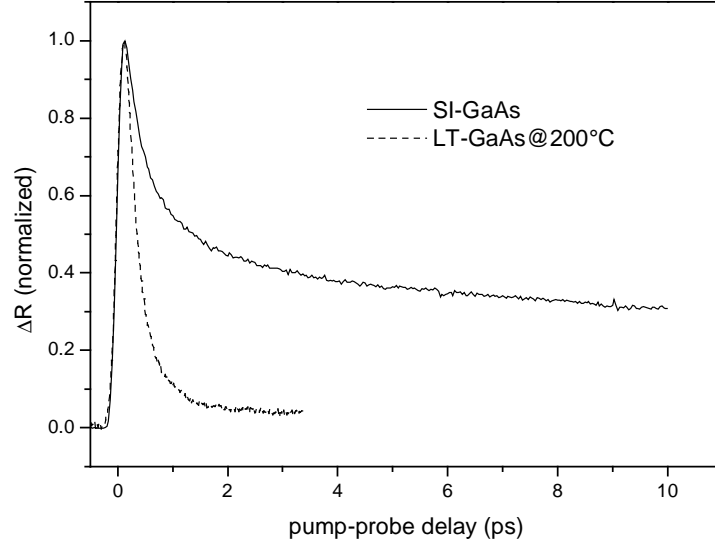
Fig. III.3.3.2. *Time evolution of the transient reflectivity of low-temperature-grown- and semi-insulating GaAs measured with the optical pump-probe technique (measurements by Tobias Korn).*

The exponential rise of E_{peak} at lower fields is due to a Schottky barrier that normally appears between the electrode (or silver paint) and semiconductor. This effect has been first observed with respect to subpicosecond electrical pulse generation on transmission lines[55] then the THz radiation from semiconductor surfaces[56] and from narrow-gap biased semiconductor emitters[57].

The density of the current through a Schottky barrier is given as

$$j = j_S \left[\exp\left(-\frac{e}{kT} U \right) - 1 \right]$$

(III.3.3.1)

with j_s expressed in the framework of the diode model of a metal-semiconductor transition[58]:

$$j_S = \frac{1}{4} e n_0 v_T \exp\left(-\frac{e}{kT} U_c \right),$$

(III.3.3.2)

where U_c is the contact voltage drop (i.e. eU_c the height of the barrier), n_0, v_T, and T are the concentration of photocarriers, their mean velocity, and temperature,

respectively. It should be mentioned that such description of the Schottky barrier in the case of a photoexcited semiconductor is quite rough since the use of the Eq. III.3.3.1 implies that the carriers have Maxwell-like distribution which can be hardly applied to THz emitters where only very hot carriers in few picosecond after generation take part in the radiation process[59].
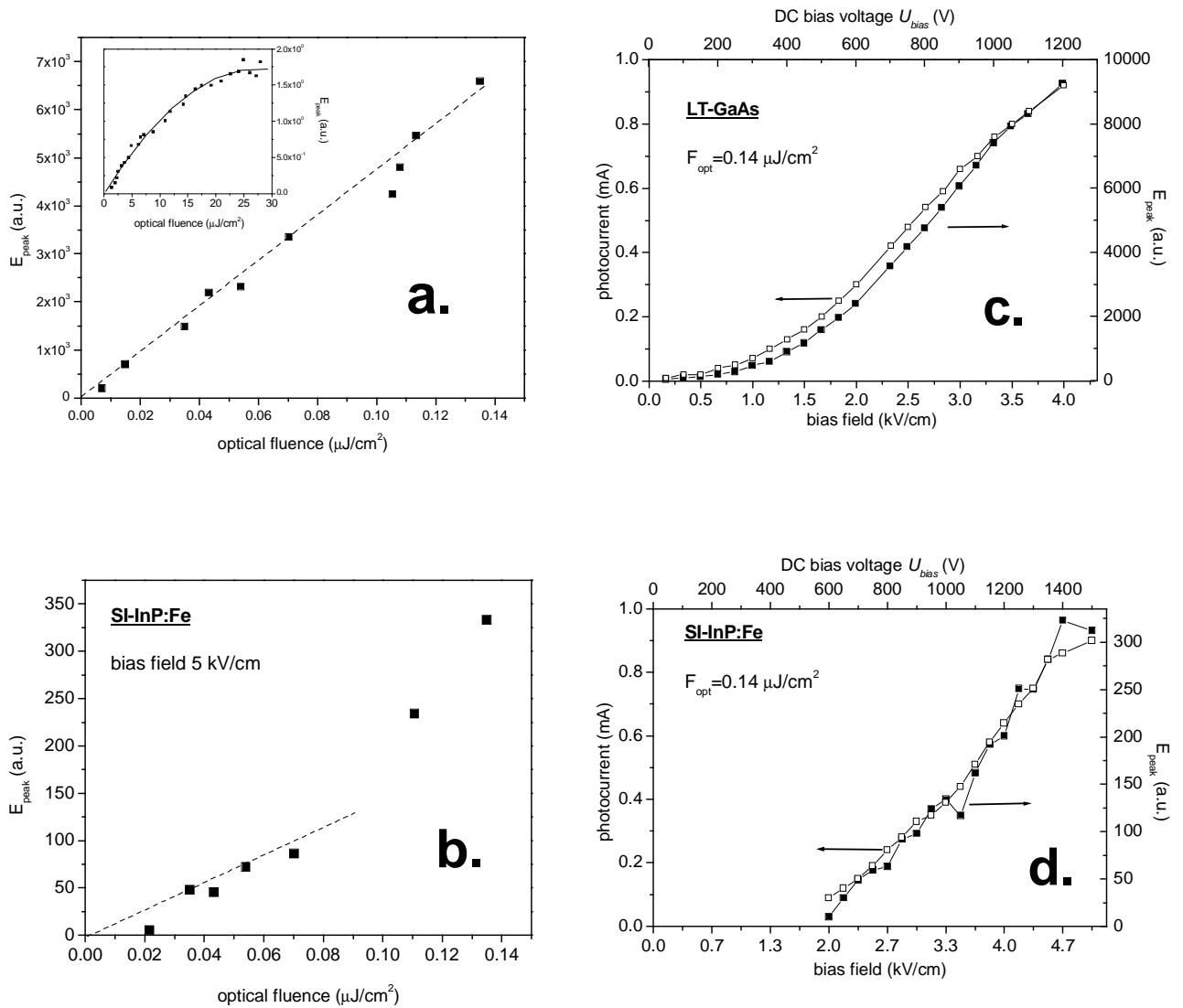
Fig.III.3.3.3. *The peak value of the electric field of a THz pulse E_{peak} as a function of the incident optical fluence (a, b) and the applied dc bias field (c, d) for 3-mm aperture InP:Fe and LT-GaAs emitters. The inset in the panel (a) shows the values of E_{peak} at high optical fluences*
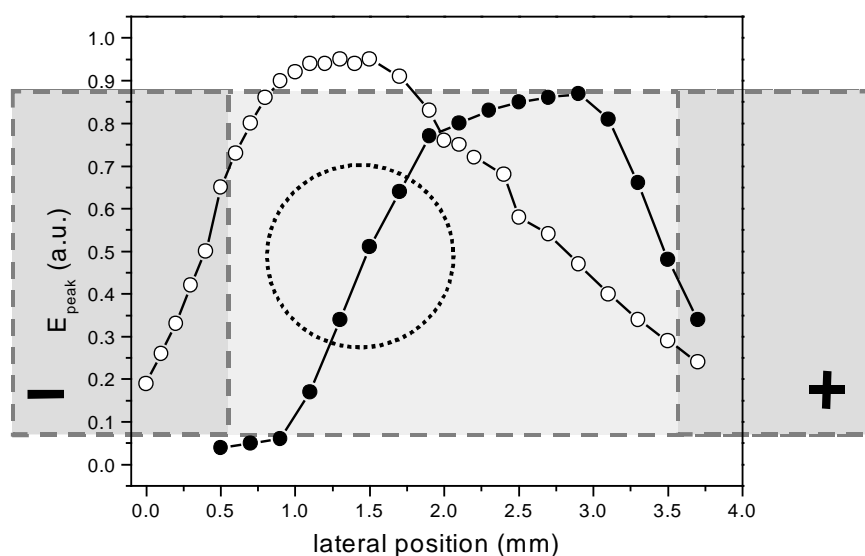
Fig. III.3.3.4. *LT-GaAs biased emitter: dependence of the peak value of the electric field of THz pulses on the lateral position of the laser spot for positive (filled circles) and negative (open circles) bias polarity. The emitter with negative bias applied is schematically shown in the background of the graph. The dotted circle symbolizes the laser spot.*

The emitter can be modeled with two back-to-back Schottky barrier diodes. The presence of such structure manifests itself in a strong dependence of the photocurrent (and, consequently, the strength of the radiated field) on a lateral position of the laser spot on the emitter (see Fig III.3.1; the direction of the lateral scan is shown by the arrow). When the spot is closer to the negative electrode (i.e. to the forward biased barrier), the photocurrent is high and the photogenerated carriers take an active part in the radiation process. However, when the spot is shifted to the positive electrode, the photocurrent is severely suppressed by the reverse biased metal-semiconductor transition (see Fig III.3.3.4).

III.4. Conclusions

Two types of THz emitters have been tested. Unbiased surface semiconductor emitters are very convenient in fabrication and operation. Of all materials studied, <100> InP:Fe has proven to have the strongest THz emission.

Biased emitters require special holder and some additional equipment (high voltage supplies and sometimes coolers) but provide two orders of magnitude stronger radiation than could be obtained from unbiased surface of the same material. Furthermore, biased emitters are set for normal to the direction of the THz radiation propagation which allow the subtraction of internal echoes and thus attaining higher frequency resolution of a spectrometer.

The next chapter is concentrated on two kinds of THz detectors which we employed in our spectrometers: photoconducting antennas and electro-optic sampling and their applicability in different types of THz spectrometers.

IV. DETECTION OF THZ PULSES

The spectral range covered by a time-domain spectrometer is determined by the source of THz radiation, the THz optics, and the receiver. A biased LT-GaAs emitter like the one employed in our spectrometers, releases the THz radiation with the frequencies up to 4 THz, limited by time-varying mobility and the onset of intervalley scattering and carrier trapping[60]. The properly chosen F-numbers of the focusing mirrors (Section V.1.3.) guarantee an efficient collection of the emitted radiation without significant spectral losses. Therefore, the operational bandwidth of the spectrometers is limited mainly by the spectral response of the detector of THz radiation. The following two types of sensors were employed in our spectrometers: photoconducting dipole antennas (PDA) and a electro-optic sampling system (EOS).

IV.1. Photoconducting dipole antennas

Basically, a PDA consists of two metallic leads separated by narrow photoconducting gap. In the pump-probe scheme (see Chapter II), the antenna is gated by a probe optical laser pulse that generates a bunch of photocarriers in the photoconductor. The electric field of a THz pulse is polarized across the antenna and serves as bias. The photocurrent through the gap between the antenna's leads is then proportional to the applied THz field. The current through the antenna is amplified with a current preamplifier and measured with a lock-in amplifier.

In reality, the measured waveform is a convolution of the laser pulse envelope, the response function of the antenna, and the THz pulse itself. Thus, similarly to THz emitters, it is necessary to use photoconductive materials characterized by short carrier lifetimes.

The antennas which we used (Fig. IV.1.1) were designed in Hamburg and fabricated in the Institut für Halbleitertechnik of the Technische Hochschule in Darmstadt.

In order to focus the THz radiation tighter on the photoconducting gap, a hemispherical silicon lens is attached to the antenna. The focal point of the lens must

be set on the photoconducting gap of the antenna with the maximum precision possible since the misalignment of even few microns can lead to the drop of the detector signal of an order of magnitude[61]. In our laboratory, Dr. I. Wilke has developed an antenna layout with special aluminum adjustment marks deposited on the back side of the antenna substrate (Fig. IV.1.1a,d). When glued to the antenna, a lens is carefully centered on the gap according to the marks.

The lens also prevents the appearance of artifacts in the measured waveforms due to multiple reflection of THz radiation within the antenna substrate. Although it would be better in terms of the refractive index matching, we do not use a sapphire lens, since sapphire in the THz range has significantly higher absorption than silicon.

The detection bandwidth of a dipole antenna is determined by its size. A longer dipole is more efficient at the lower frequencies but has narrower bandwidth[62]. On the other hand, there is fundamental limitation to the reduction in the antenna size. Even focused to the diffraction limit, which is hundreds of microns, THz radiation cannot be effectively collected by a small area of the detector antenna and the signal-to-noise ratio (SNR) will suffer.

SiO₂

(b)

poly-silicon

42μm

2μm

photoconducting gap, 4μm

aluminum electrical leads, 5μm

10μm

(c)

10 μm

15 μm

(a)

(d)

optical pulse (probe beam)

Al stripe, 25 nm

poly-Si, 0.5 μm

thermal SiO₂, 0.7 μm

high-ohmic Si, 250 μm

thermal SiO₂, 0.7 μm

alignment mark

Si lens Ø 6 mm

THz beam
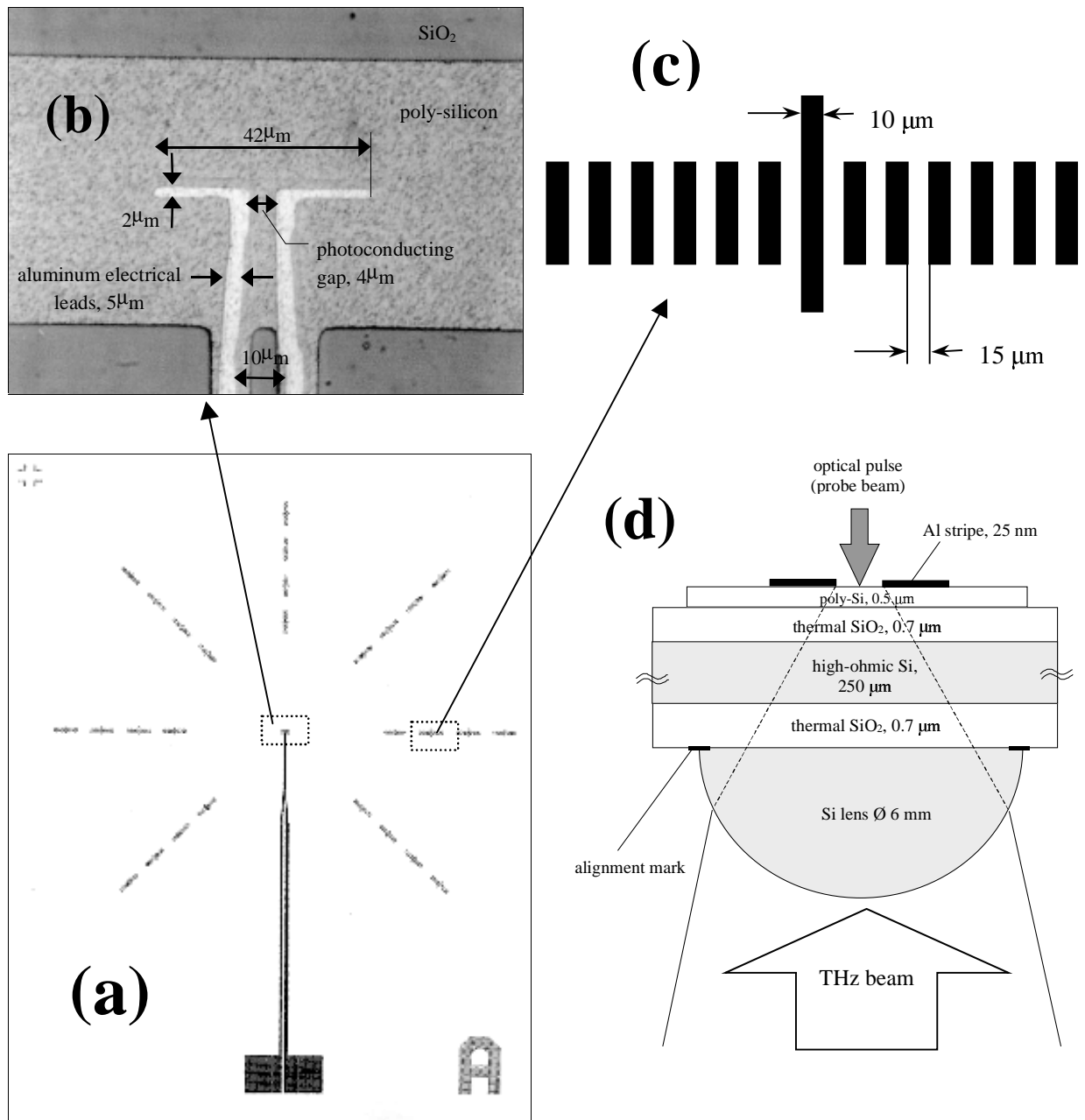
Fig IV.1.1. Photoconducting dipole antenna detector: a - the whole layout (top view), b - photoconducting gap (magnified), c – alignment marks (magnified), d - side view (cross section).

Semiconductor antennas are compact (the whole detection system is just one chip) and are convenient in adjustment and operation. Compared to the EOS described in the next section, they are characterized by a several times higher sensitivity[63]. With antenna detectors, we attained a SNR of 2500:1.
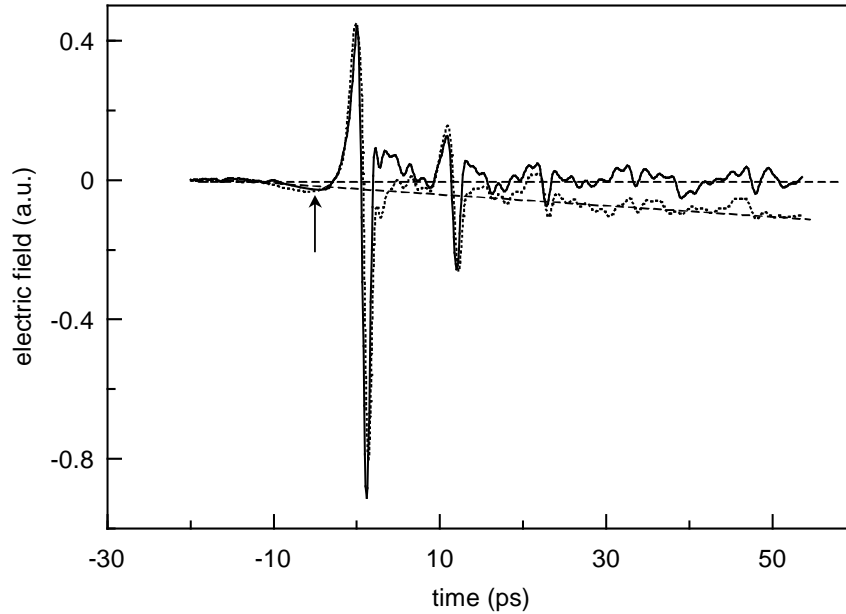
Fig IV.1.2. Drift of the background of THz pulses from a high-bias emitter detected with a photoconducting dipole antenna (dotted line). The background is flat when the THz beam instead of optical pump beam is chopped (solid line). Arrow marks the broad minimum originating from the long relaxation of the photocarriers in the phoconducting gap of the antenna.

The main disadvantage of simple dipole antennas as THz sensors are their relatively narrow bandwidth and some artifacts produced at lower frequencies. One is a broad minimum (Fig. IV.1.2) before the main peak that is a sign of long living photocarrier fraction in the photoconducting gap of the antenna (provided that THz radiation is properly focused and the minimum is not a result of the Gouy shift, see Section VI.1.3). Another problem revealing when an antenna is used together with a high-voltage emitter, is a drifting background of the measured pulses. The reason is the antenna being sensitive enough to detect the *spatial* change of the static (but chopped!) electric bias field of the emitter due to the delay stage movement. To overcome this, the chopper should be placed just after the emitter to chop the THz beam not the optical pump beam.

IV.2. Electro-optic sampling

Developed originally for the characterization of ultrashort *electrical* transients[64], the electro-optic sampling (EOS) has developed into a powerful method of the detection

41

of THz pulses[65,66]. The EOS system built up in our laboratory is described in detail in the diploma thesis of Hanns Selig[20] so that only a brief overview of it will be given here.

The EOS is based on the electric field of a THz pulse inducing a small birefringence in an electro-optic crystal through a non-linearity of the first order (Pockels effect). Passing through such crystal, the initially linearly polarized optical probe beam gains small elliptical polarization. In the first approximation, this ellipticity is proportional to the electric field applied to the crystal i.e. to the THz field in every certain moment of time. Since the THz pulse is much longer than the laser pulse (several ps vs tens of fs), the THz field can be approximately treated as a dc bias field. Thus, by the variation of the delay between THz- and optical probe pulses the whole time profile of the first can be traced.

As EOS active medium, a variety of dielectric materials like $LiTaO_3$ [Ref. 67, 68] and ZnTe [Ref. 67] or polymers polarized by externally applied field[68,69] is employed. If a medium is not absorbing very strongly, its optical properties can be described with the help of the refractive-index ellipsoid[69]

$$\sum_{i,j=1}^{3} \frac{x_i x_j}{n_{ij}^2} = 1 \, , \qquad\qquad\qquad\text{(IV.2.1)}$$

where x_i, x_j are the Cartesian coordinates and $n_{i,j}$ are components of the refractive-index tensor. An applied electric field causes changes in optical properties of the crystal (so-called electro-optic effects). This can be seen as distortions of the the refractive-index ellipsoid:

$$\sum_{i,j=1}^{3} \left(\frac{1}{n_{ij}^2} + \sum_{k=1}^{3} r_{ijk} E_k \right) x_i x_j = 1 \, , \qquad\qquad\text{(IV.2.2)}$$

where E_k are components of the applied electric field and r_{ijk} is the electro-optic tensor describing the non-linearity if the first order (i.e. the Pockels effect).

Nonlinearities of higher orders are usually very small at the field strength typical for THz pulses ($E < 3$ kV/cm, Ref. 70) and can be ignored.

In our setup we used a 10x10x1 mm^3 (110)-cut crystal of ZnTe. With no electric field applied, the material is isotropic so that the refractive-index ellipsoid is simply a sphere i.e. $n_{i,j} = n$ for every i and j. In this case the choice of the coordinate system is arbitrary and it is convenient to set the axes $x_1=x$, $x_2=y$, and $x_3=z$ along the main crystallographic directions of ZnTe.

The orientation of the crystal with respect to the propagation direction and polarization of the THz- and the optical probe beam corresponding to the strongest Pockels effect is shown in Fig IV.2.1.a. The coordinate system x', y', and z' is linked to the propagating beams: the beams travel along the $x' = <$-1-10$>$ direction, the optical probe and the THz beams are polarized along $z' = z = <$001$>$ axis and $<$-110$>$ direction, respectively. Under the influence of the applied THz field, the sphere (IV.2.1) turns to an ellipsoid (IV.2.2) with the main axes oriented along x'', y'', and z'' directions (Fig. IV.2.1b):

$$n_{x''} = n$$
$$n_{y''} = n - \tfrac{1}{2}\, r_{231}\, n^3\, E_{y'} \qquad\qquad\qquad\qquad\text{(IV.2.3)}$$
$$n_{z''} = n + \tfrac{1}{2}\, r_{231}\, n^3\, E_{y'}$$

with $r_{231} = 4.0 \cdot 10^{-12}$ m/V for ZnTe.

<001>

z

ZnTe

$E_{y'} = E_{THz}$

y <010>

x
<100>

optical beam
(vertically
polarized)

(a)

z, z'

z"

y"

y'

y

x

x',x"

(b)

z

n_z

$n_{y'}$

y'

$E_{y'} = 0$

(c)

z

z"

y"

$n_{z"}$

$n_{y"}$

y'

$E_{y'} \neq 0$

(d)
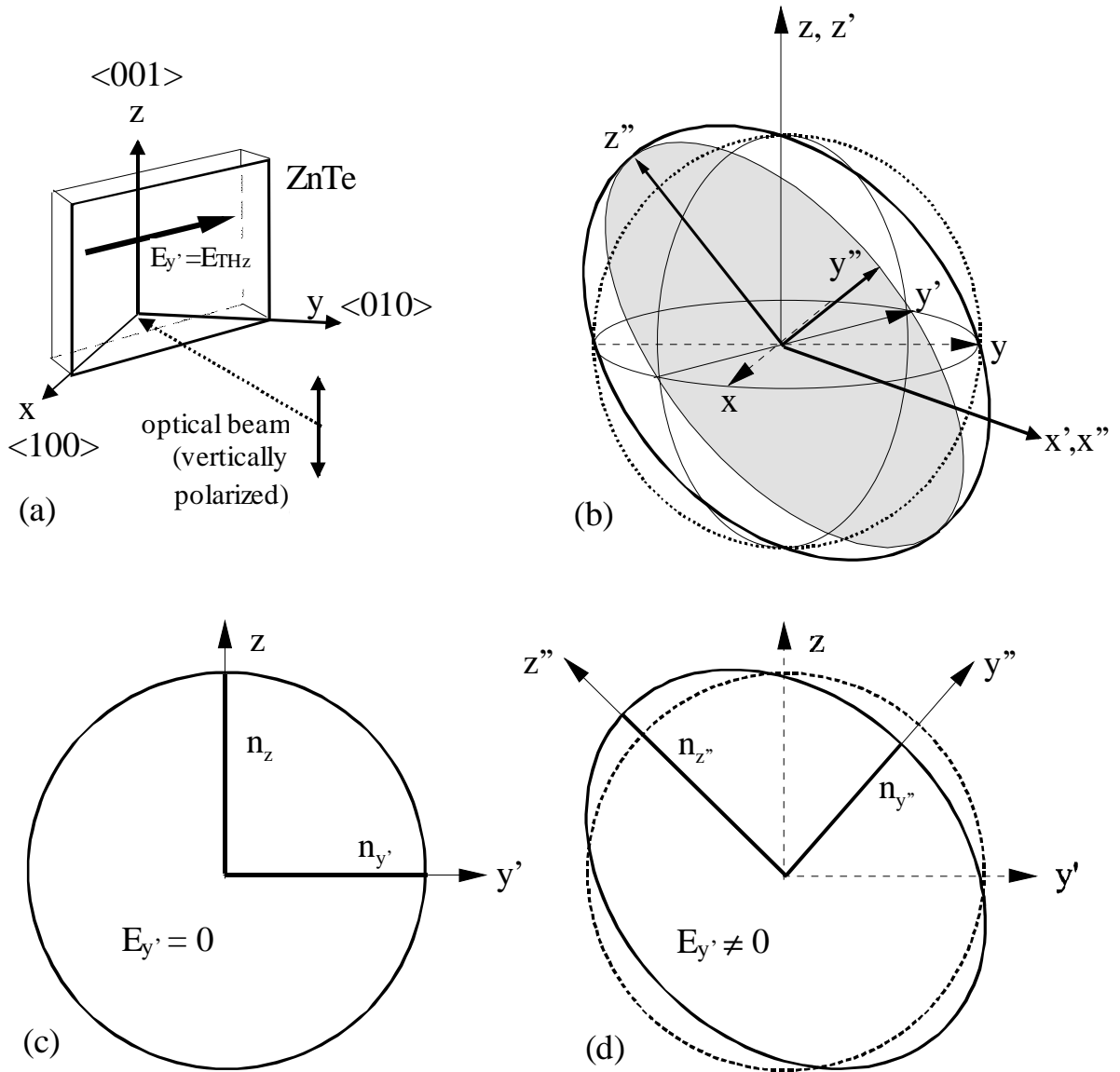
Fig IV.2.1. *(a) Relative orientation of the THz electric field E and the polarization of the laser probe- and the THz beams with respect to the ZnTe crystal. The shown geometry corresponds to the maximum electro-optic (Pocklels) effect. (b) The refractive-index ellipsoid. The x, y, z coordinates are set along the main ZnTe crystallographic directions; the primed axes are defined as the THz- and the optical probe beams propagation (x'), the THz- (y') and the probe beam (z' = z) polarization directions. The double-primed axes correspond to the orientation of the main axes of the refractive-index ellipsoid under the $E_{y'}$ field applied. (c) and (d) depict the projection of the ellipsoid on the surface of the crystal (i.e. as it is "seen" by the incident laser probe beam): without the THz field (c) and with THz field present (d). The figure is taken from Ref. 20.*

Having passed through the EO crystal, the y"- and z"-components of the electric field of the incident optical wave acquire the phase shift

$$\delta\varphi = \varphi_{y"} - \varphi_{z"} = \frac{\omega}{c}\left[n_{y"}\left(E_{y'}\right) - n_{z"}\left(E_{y'}\right)\right]dx' ,$$ (IV.2.4)

or taking Eq. (IV.2.3) into account:

$$\delta\varphi = \frac{\omega}{c}n^3 r_{231}E_{y'}dx'$$ (IV.2.5)

In the absence of the THz field ($E_{THz} = E_{y'} = 0$), the phase shift is zero and the polarization of the probe beam stays linear. When, however, the THz pulse is present the phase shift (IV.2.5) leads to a slightly elliptical polarization.

In practice, a differential scheme of the EOS is usually employed (Fig. IV.2.2). A quarter-wavelength plate is placed behind the electro-optic crystal to make the initially linear polarization of the probe beam (at $E_{THz} = 0$) circular. A Wollaston prism separates its y"- and z"-components components and sends them to photodiode detectors which are connected to the differential input of a lock-in amplifier. With no THz pulse present, the components have equal intensity and the differential signal is zero. When the THz field is applied, a non-zero phase difference (IV.2.4) of the two components appears. Note, that according to Eq. IV.2.5, it is proportional not only to the magnitude of the applied field but also to its sign which makes the whole detection method phase-sensitive.
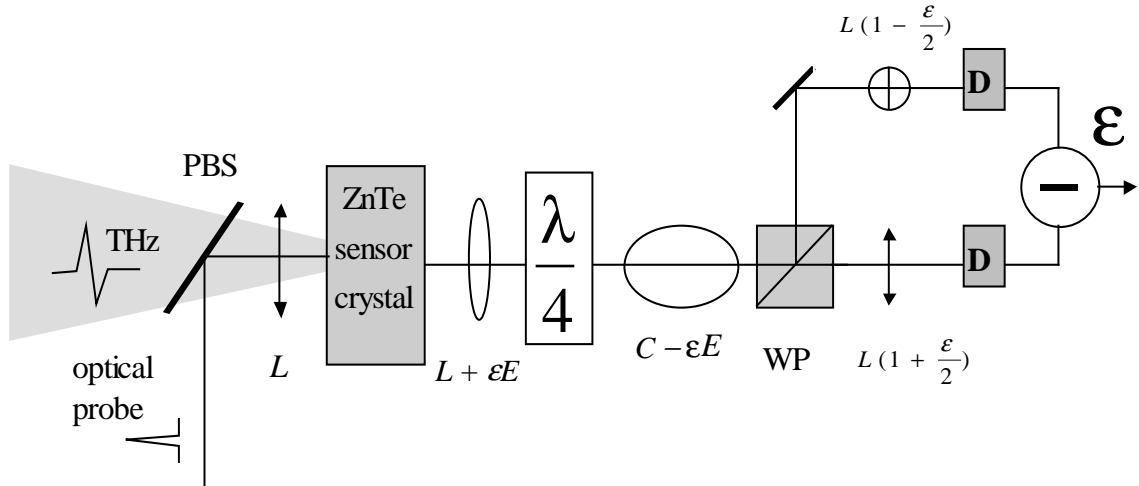
Fig IV.2.2. The schematics of electro-optic sampling. PBS – pellicle beam splitter, $\frac{\lambda}{4}$ - quarter-wavelength plate, WP – Wollaston prism, D – slow photodiodes. Symbolic expressions for the polarization of the optical probe beam: L – initial linear; L + εE – slightly elliptical, close to linear; C - εE - slightly elliptical, close to circular; ε is the fraction of the elliptical polarization.

We use the EOS geometry with the THz – and probe beams propagating collinearly through the sensor crystal. For this purpose we employ a 2" beam splitter made of very thin (0.2 mm) polymer transparent for THz radiation and reflecting around 5% of optical radiation (so-called pellicle beam splitter, or PBS). The major advantage of a PBS is that thank to its thinness, it does not lower the temporal resolution of the system through multiple internal reflections. It is, however, extremely fragile and quite sensitive to even small vibrations of the air in the laboratory.

The highest SNR reached in our spectrometers with EOS is at least 1000:1. Compared to the photoconducting antenna detectors (Section IV.1), the EOS is somewhat less sensitive but, on the other hand, being not limited by the lifetime of photocarriers, covers a broader spectral range (up to 3.5 THz for freely propagating pulse). It is also free from artifacts typical for PDA like a broad minimum before the main peak and the drifting background (Fig. IV.1.2). Moreover, it is mechanically much more stable than PDA and does not require very precise optical adjustment.

V. DEVELOPMENT OF THE TIME-DOMAIN THZ SPECTROMETERS

In this Chapter the time-domain spectrometers, which have been built up in our laboratory, are presented. Our first spectrometer (Fig. III.2.1.1) was intended for testing various THz emitters and detectors. It could be applied to the measurements of complex transmittance only of very large (3 cm x 3 cm or larger) samples since it did not have an intermediate focal point to place a small sample to. Thus, a larger time-domain THz transmission spectrometer suitable for the study of smaller samples have been developed.

Section V.3 is devoted to the first convertible transmission-reflection THz spectrometer that I have designed, build up and tested. The spectrometer has proven to be very flexible and easy to operate and will serve as a base for the future time-domain THz ellipsometer (Section VIII.1).

V.1. Overview of THz spectrometer

This section is devoted to the major parts and components common for all our set-ups which have not been described in preceding chapters: a femtosecond laser, focusing and collimating THz optics, electronic and mechanic devices like lock-in amplifier, chopper, and motorized delay line, and a data acquisition system. Also, a closed-cycle cryostat that is an integrated part of our spectrometers is described here.

V.1.1. Laser

Our THz spectrometers are powered by a Spectra-Physics Tsunami[TM] Titan-Sapphire laser pumped by a Spectra-Physics Millenia[TM]-V Nd-YAG cw laser. The main performance parameters of the laser system are summarized in Table V.1.1.1.

Table V.1.1.1 *The performance parameters of Spectra-Physics Tsunami[TM] laser*

average output power	Ti:Sa (Tsunami)	600-750 mW
	pump (Millenia)	5 W (cw 532 nm)
mode locking	passive through Kerr-lens mode locking[71,72] + active by acousto-optic modulator[73]	
minimum pulse width	< 50 fs	
minimum spectral width	< 15 nm	
tuning range	735-840 nm	
repetition rate	82 MHz	
polarization	> 500:1 vertical	
beam divergence	< 0.6 rad	

V.1.2. Electronics and data acquisition

The photocurrent caused by a THz field in a gated detector (either an antenna or photodiodes in EOS) lay in picoampere range which means that it is in principle weaker that the thermal noise in the detector and the antenna effect in connectors and cables. This obstacle is overcome by the use of a phase sensitive detection technique named *lock-in detection*. Its basic principle is the modulation of the THz beam at some fixed frequency and then select from the whole output only the signal at this reference frequency. Applied to the TDTS, either pump optical beam or directly the THz beam is modulated by a mechanical chopper (Stanford Research Inc., model SR540). The data acquisition scheme is depicted in Fig. V.1.2.1. When a photoconductive antenna is used as a detector (see Section IV.1), the signal is first enhanced by a low-noise current preamplifier (Stanford Research Inc., model SR570) and then is detected at the reference frequency by a lock-in amplifier (EG&G Princeton Applied Research, model 5210). When THz pulses are detected with electro-optic sampling (EOS, see section IV.2), the photodiodes are directly connected to the differential input of the lock-in amplifier (LIA).

The delay stage endowed with a dc-motor actuator (Newport 850F) and driven by a motion controller (Newport Motion Master MM3000) can be moved either continuously or stepwise with adjustable waiting time between steps. The mechanical

precision of the movement is 0.1 μm which corresponds to the time shift of 0.66 fs. However, the actual time resolution of a THz system is defined by a convolution of a laser pulse envelope and a response function of the THz detector and is about few tens of fs.
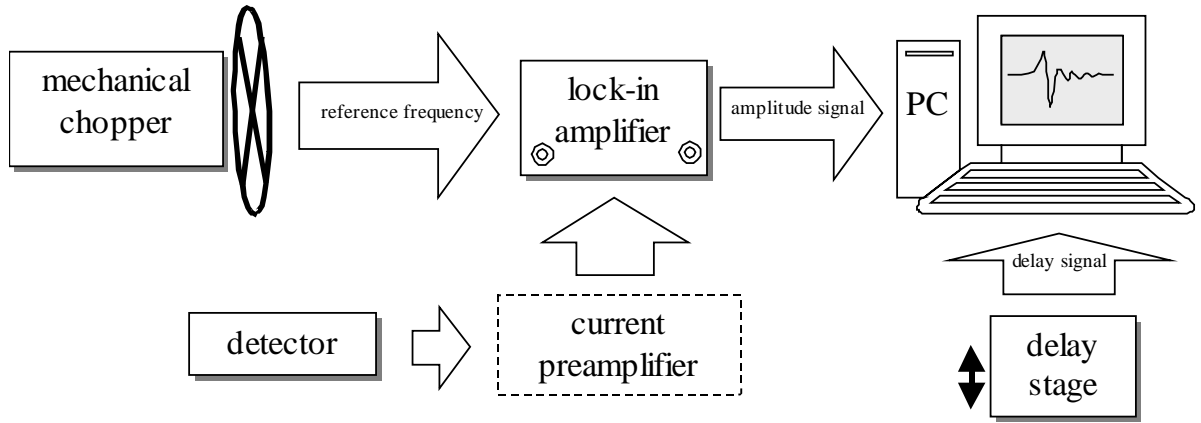
Fig. V.1.2.1 *Data acquisition scheme. The detector is either a dipole antenna or photodiodes (for EOS). The current preamplifier was used only with the antenna, in the case of EOS the photodiodes were connected directly to the differential input of the lock-in amplifier.*
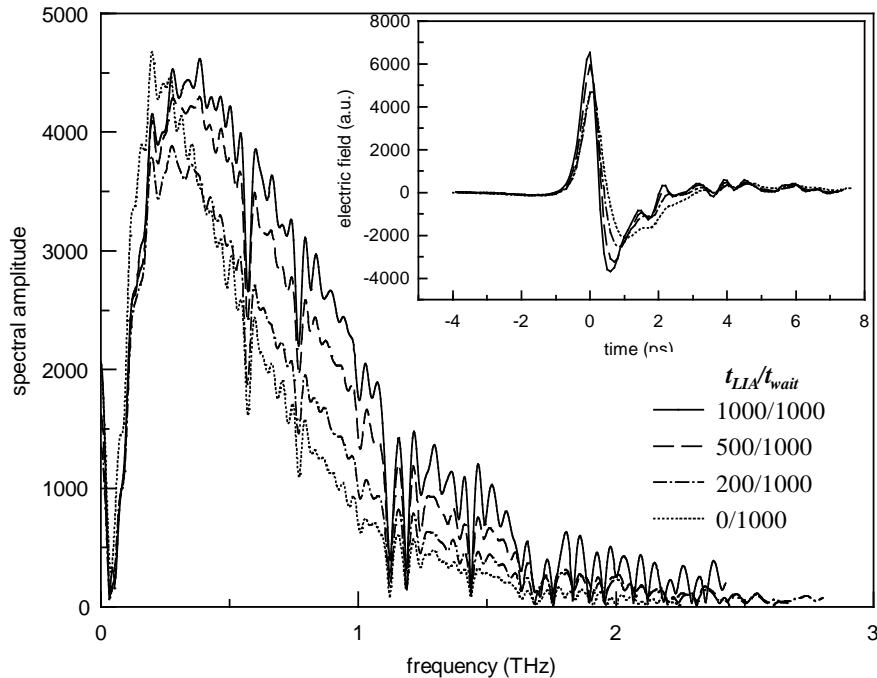
Fig. V.1.2.2 *The influence of the change of the delay stage waiting time on the shape and amplitude spectrum of detected THz pulses (freely propagating pulses shown). See the text for explanations.*

49

There are three basic time periods in a TD-THz spectrometer: t_{wait} delay stage waiting time, t_{LIA} - the time constant (integration time) of the LIA, and f_{chop} - the chopping frequency. The choice of the constants is a trade-off between the time of measurements, the signal-to-noise ratio (SNR), and the sensitivity of the spectrometer at higher frequencies. The longer is t_{LIA}, the narrower the noise bandwidth of the amplifier is and so the better the SNR will be. But this improvement is gained at the expense of increased response time and, consequently, the duration of measurements since $SNR \propto \sqrt{t_{LIA}}$. In principle, t_{wait} should be several times larger than t_{LIA}. Otherwise, the LIA does not manage to integrate the whole signal during the delay waiting time which results in smoothing of narrow details in measured THz waveforms i.e. losing of the higher frequencies in spectrum (see Fig. V.1.2.2).

For THz spectroscopic measurements, we typically set $t_{LIA} = 1$ s. But in this case, for example, a 40 ps scan with 50 fs step takes up to a half an hour. If one is sure not to have any high-frequency peculiarities in spectra, the measurements can be speeded up by setting lower t_{wait}.

V.1.3. THz optics

THz optics serves for collection of the THz radiation from the source, its guidance through air (and, eventually, a sample) and its focusing onto a detector. The optical path of the THz radiation in an arrangement intended for spectroscopic applications on smaller samples should contain at least 3 focal points: for a THz emitter, a sample, and a detector. Basically, polyethylene lenses or metallic mirrors are used for that purpose. The most convenient mirrors shapes are off-axis paraboloidal and elliptical.

Paraboloids

In the spectrometers, which we have built in Hamburg, off-axis parabolic mirrors were employed (Fig V.1.3.1). The focal diameter for every certain wavelength is $4\lambda F/\pi$, where λ is wavelength and F is the nominal focal ratio[74] (or F-number). In our case, F is the ratio of the mirror's focal length f and its aperture d : $F = f/d$. Thus, in order to collect efficiently the THz radiation coming from the emitter as a strongly divergent beam, the first paraboloid must have quite small F. The mirror used by us have $F = 1$ so that only by the radiation with frequencies below 127 GHz it comes to some minor losses. The second parabolic mirror serves to focus the THz radiation onto the detector antenna (in our first spectrometer, see Fig. III.2.1.1) or onto a sample (in all configurations followed). Its parameters were chosen to ensure an efficient focusing of THz radiation and to fit the geometrical dimensions of the spectrometer. We employed mirrors with the diameter $d = 50.8$ mm and the focal lengths $f = 101.6$ mm (i.e. $F = 2$) and 152.4 mm ($F = 3$) so that for our longest wavelengths, which laid around 100 GHz, the focal spot has a diameter 7.6 mm and 11 mm, respectively. This determines the minimum sample size and the size of the apertures in the sample holder in the cryostat.
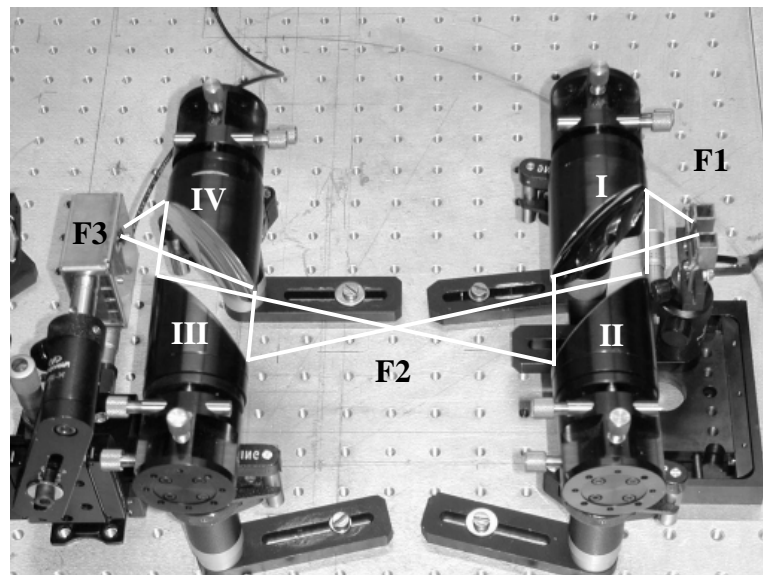
Fig V.1.3.1. The four off-axis parabolic mirror sequence. I - IV - the mirrors, F1 – F3 – focal points: a THz emitter and a detector occupy F1 and F3, respectively, and a sample is set to F2. White lines mark the edges of THz beam.

Alignment of THz optics is usually very tricky. A very smart solution have been described by E. Parks[75]. She used sunlight as a source for parallel light to adjust the mirrors II and III (see Fig V.1.3.1). Unfortunately, the sunshine is quite rare event in Hamburg so we normally aligned the mirrors with the help of optical laser beam. The beam was aligned with a plump along the lines drawn on the surface of the optical table. For the fine adjustment, a piece of Scotch tape have been set to the F1 point. It scatters laser light strongly and thus can serve as a point source of light. Then the position of the light spot in F2 is marked with an iris. After that the piece of Scotch tape is installed in F3 and the mirrors III and IV are adjusted to send the laser beam exactly through the iris.

Elliptical mirrors

A pair of elliptical mirrors is used in the THz spectrometer built in Prague. Unlike a paraboloid, an elliptical mirror has two focal points so that it is possible to arrange a THz spectrometer with only two mirrors. However, compared to paraboloids, such mirrors are harder to produce (and, consequently, are more expensive) and their adjustment is more complicated.

THz Emitter

THz detector
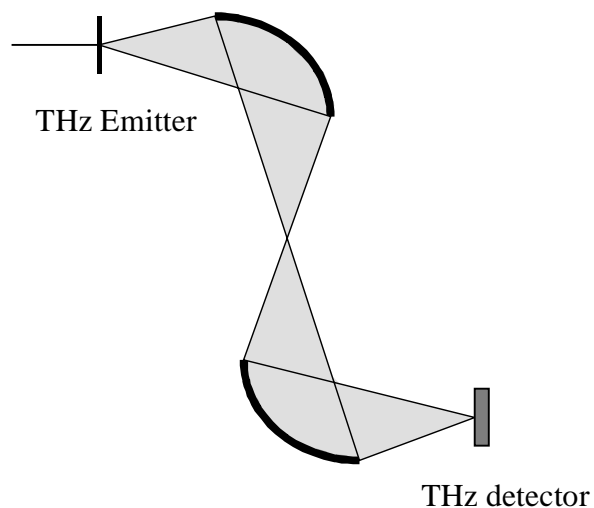
Fig V.1.3.2. Focusing of the THz radiation with a pair of elliptical mirrors.

V.1.4. Cryostat

To enable low-temperature measurements, we have built up a cryogenic system based on a Edwards Coolstar 2/9 closed-cycle cryostat (Fig. V.1.4.1). Unlike helium bath- or continuous-flow cryostats, the closed-cycle systems are compact and do not require liquid helium supply. The vacuum chamber is first evacuated by a turbo pump down to 10^{-5} - 10^{-6} mbar. Then the cooling system is switched on and high-pressure helium gas provided by a Cryodrive compressor is cyclically expanded in the cylinder with a piston in the Coolstar 2/9 unit[76].

We have worked out a design of a sample holder and a vacuum chamber, which meet the specific requirements of THz spectroscopy. The sample holder is attached to the heat station (or "cold finger") of the Coolstar unit. Up to three samples can be measured in one cycle. One of the sample holder's four 8-mm square holes is reserved for a reference sample (e.g. substrate) or should be left free when a freely propagating pulse is taken as a reference. The Coolstar runs constantly at the same cooling power and the temperature of the samples is changed and stabilized by a heater integrated in the basement of the sample holder. There are two temperature sensors from Lake Shore Cryotronics, Inc. installed on the holder: one is a RF-100 Rhodium-Iron resistance chip serving to the temperature stabilization and another is a Cernox resistor (model CX-1070-AA) for the precise measurements of the temperature of the samples. The heater is controlled by a Lake Shore DRS-91C temperature controller.

The vacuum chamber has two Mylar optical windows 3.5 cm in diameter. To avoid the distortion of the measured transmittance at lower frequencies due to the aperturing of the THz beam (see section V.3) the windows should be large enough and as close to the sample holder as possible. However, such large windows have a disadvantage of heat radiation coming from outside through the windows and significantly heating up the samples. Nevertheless, the lowest temperature of 22 K attainable with our vacuum chamber (instead of 9 K with a vacuum enclosure without windows) is sufficient for the study of high-T_c superconductors.

The cryostat holder endowed with a three-dimensional positioner so that by moving the cryostat as a whole one can set a sample exactly in the THz focal point. After the THz pulse transmitted through one sample (resp. reference substrate or empty hole) is measured, the whole cryostat is laterally (either vertically or horizontally) shifted to set another sample in the focal point.
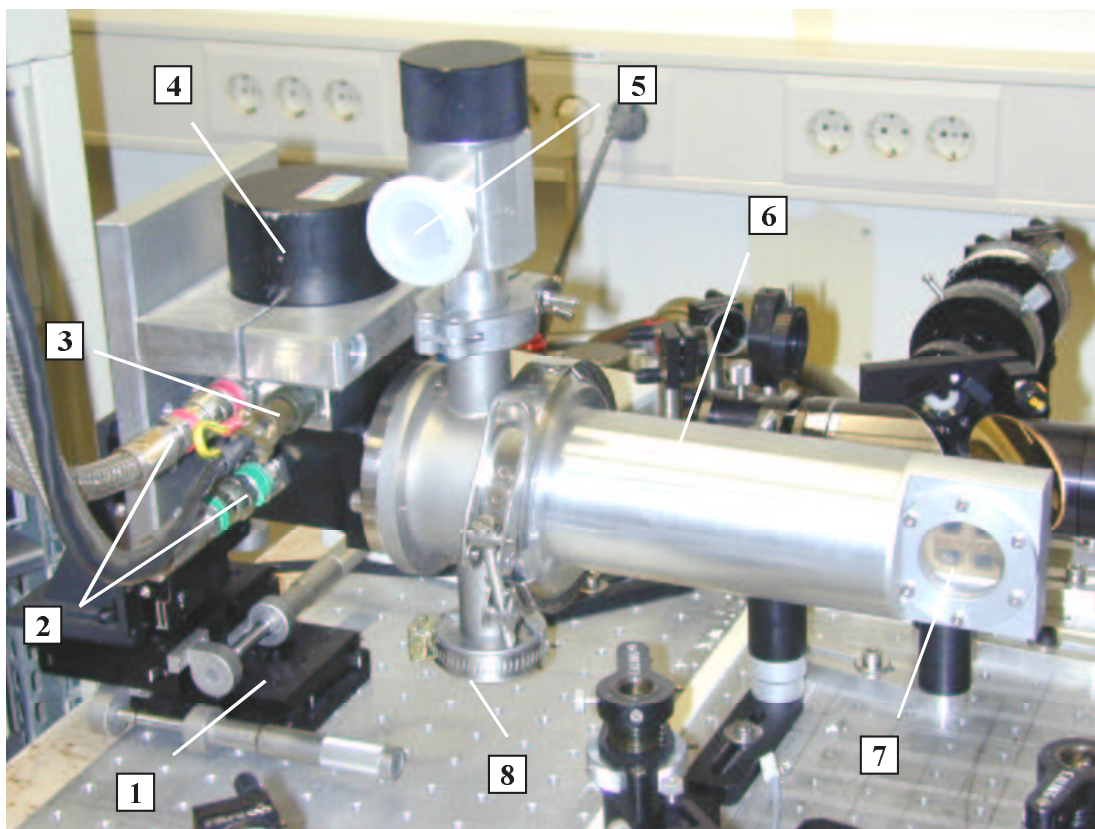
Fig. V.1.4.1 *The cryostat: 1 – cryostat holder with 3D-positioner; 2 – interconnecting helium gas lines; 3 - the Coldhead motor power supply cable; 4 – motor- and piston housing; 5 – vacuum port (the evacuation line not connected); 6 – vacuum chamber; 7 – optical window; 8 – connection to the temperature controller.*
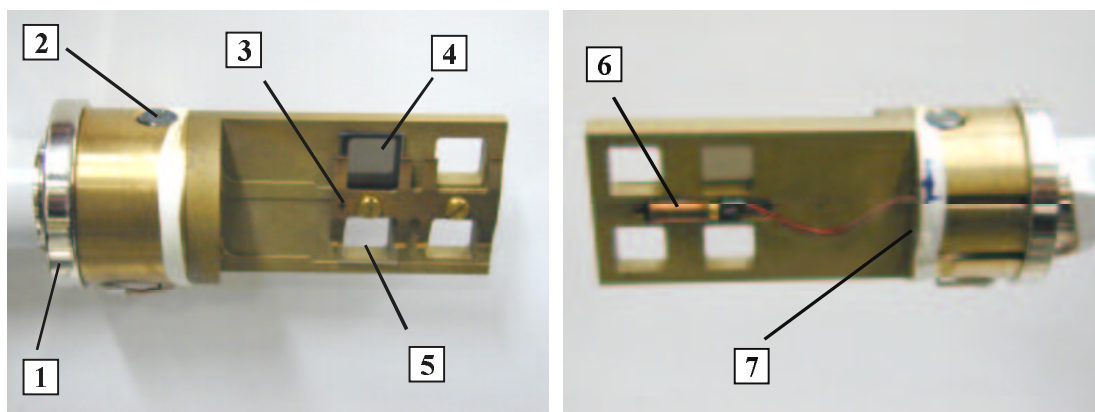
Fig. V.1.4.2. *Sample holder: 1- heat station of the Edwards Coolstar 2/9; 2 – heater; 3 - sample holding spring; 4 – a sample installed (TBCCO film on LAO substrate); 5 – LAO substrate; 6 – Cernox resistive temperature sensor; 7 – RF-100 chip temperature sensor.*

V.2. Transmission time-domain THz spectrometer

Our transmission time-domain THz spectrometer (Fig. V.2.1) is arranged according to traditional scheme widely described in literature[77,78]. The THz radiation is generated with a dc biased LT-GaAs emitter and detected with an electro-optic system described in detail in Sections III.3 and IV.2, respectively.

The emitted THz radiation is collected, lead through a sample, and focused onto the electro-optic crystal by the set of four parabolic mirrors (see Section V.1.3).

The time profile and the complex spectrum of a THz pulse freely propagating in the spectrometer are depicted in Fig. V.2.2.
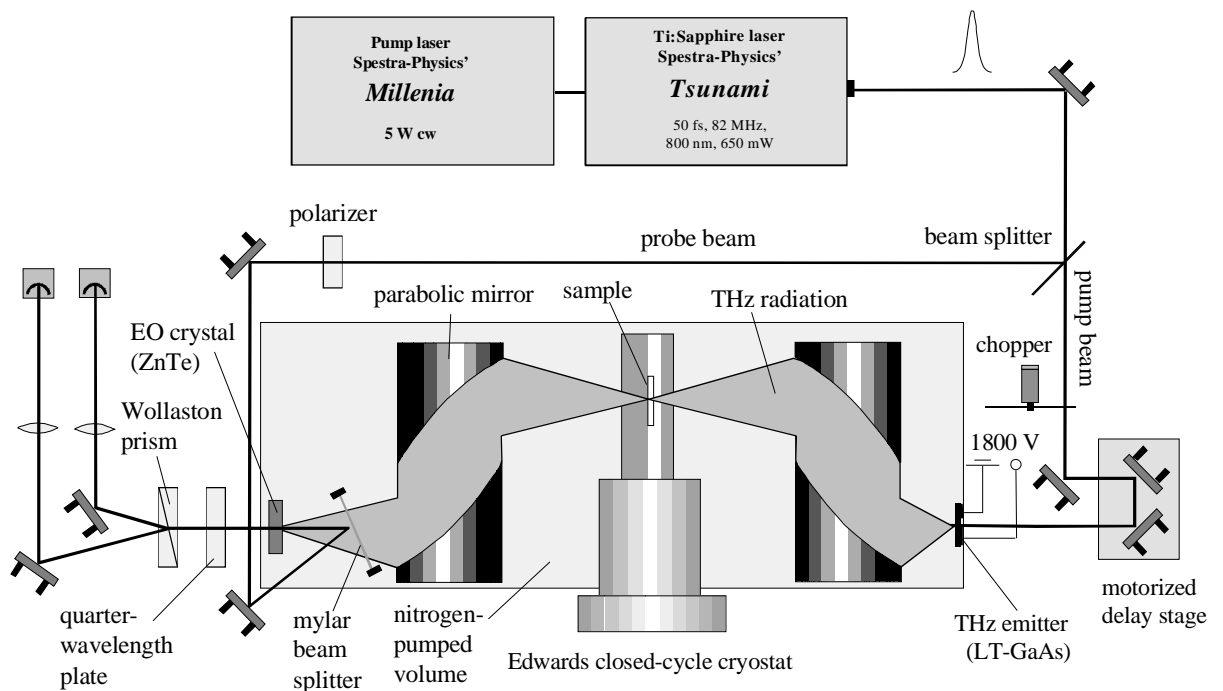
Fig. V.2.1. The transmission time-domain THz spectrometer.

The whole THz part of the spectrometer incl. the emitter, the paraboloids, and the detector is installed in a plastic box purged with nitrogen. It is done in order to eliminate the influence of water vapor that is always present in the air and strongly absorbs the THz radiation (it will be discussed in more detail in Section VI.3). The evaporated nitrogen from a Dewar vessel is warmed as it travels through a pipe immersed in hot water before it enters the box. This system is preferred to a pressured gas bottle since, for example 50 l of liquid nitrogen is sufficient for up to 6 days of measurements while a standard 50 l/ 200 bar bottle runs empty in a day.

As have been shown in Section V.1.3, for the lowest reachable frequencies the diameter of the focal spot is around 1 cm i.e. slightly larger than the size of holes in the sample holder. This leads to some minor losses at those frequencies (Fig. V.2.3).
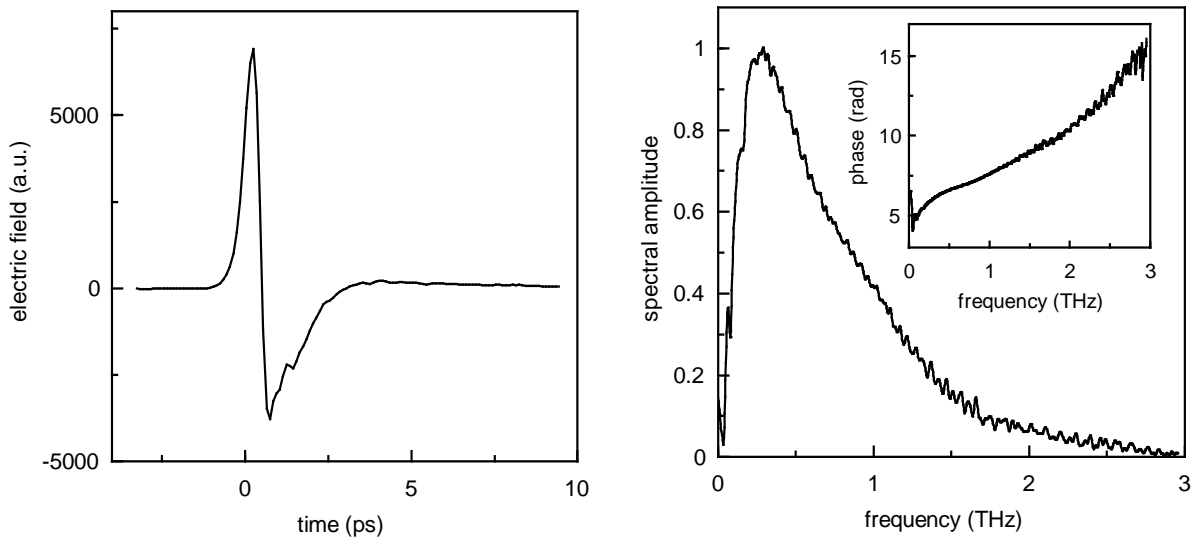
Fig. V.2.2. *A typical freely propagating THz pulse measured with the transmission THz spectrometer and the corresponding complex spectrum.*
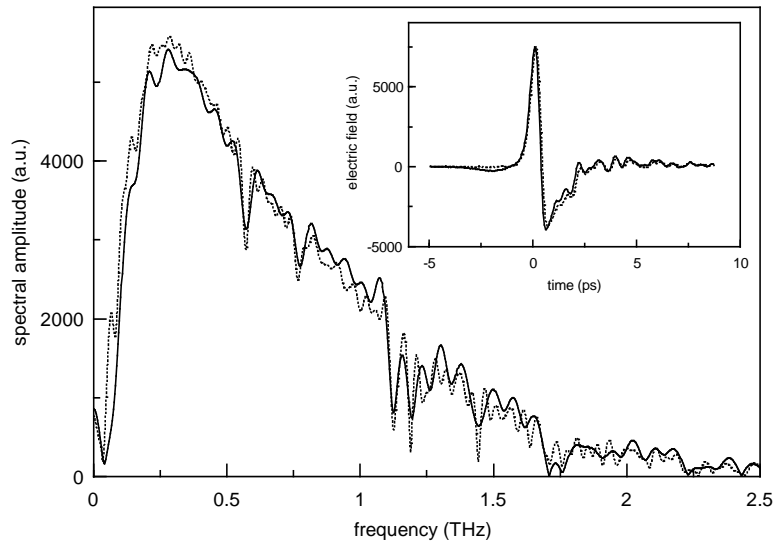
Fig. V.2.3. *Low-frequency cut-off by the sample holder. The size of holes is slightly smaller than the diameter of the THz beam at the lowest frequencies which leads to the spectrum of a THz pulse passed through a holder's hole (solid line) containing less frequencies below 200 GHz than that of the pulse measured without the holder (dashed line).*

V.3. Convertible transmission-reflection time-domain THz spectrometer

The time-domain THz transmission spectroscopy (TDTTS) is a well-developed and reliable means but it is obviously applicable only to transparent samples. Therefore, highly conductive materials can be studied with TDTTS only in the form of thin films, and for measurements on bulk samples the TDTS in reflection geometry (TDTRS) becomes the only choice. Various perspective THz imaging applications[79] especially THz tomography[80] are also based on the measurement of the complex reflectivity. To date, there have been only few works published reporting realization of the RTDTS[9, 81]. Such systems appear to be difficult to adjust since a change of the incidence angle requires a complete realignment of the whole spectrometer. Thus, the creation of a time-domain THz spectrometer that allows easy change of the incidence angle along with measurements in transmission configuration significantly extends the area of the TDTS applications.

V.3.1. Transmission configuration

In the transmission configuration (Fig. V.3.1.1), the convertible time-domain THz spectrometer is identical with the arrangement described in the previous section. The only difference is the detector which was a silicon-on-sapphire dipole antenna endowed with a 6-mm hemispherical silicon lens (see Section IV.1 for details).

The diameter of parabolic mirrors is 50.8 mm and the effective reflected focal lengths are 50.8 mm, 152.4 mm, 152.4 mm, and 50.8 mm for the parabolic mirrors PM I, PM II, PM III, and PM IV, respectively. The THz beam is polarized horizontally, i.e., in the plane of the figure. For polarization sensitive measurements, an additional tungsten-wire grid polarizer (wire diameter 10 μm, period 33 μm) is set between PM I and PM II (not shown). Such an arrangement permits measurements of the complex transmittance in the frequency range from 60 GHz to 1.5 THz with a signal-to-noise ration of at least 1000:1.
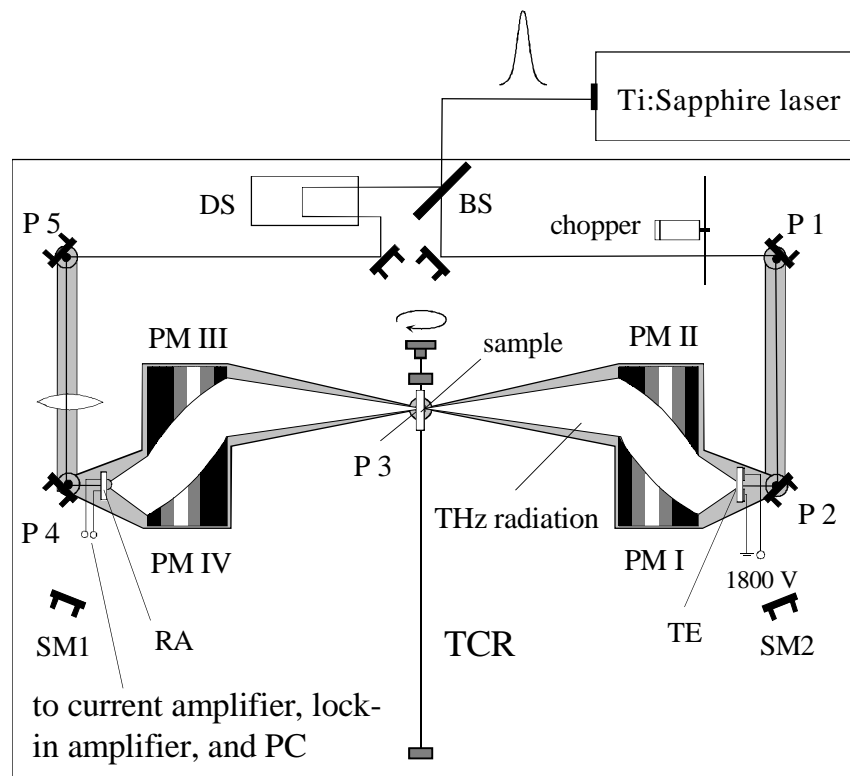
Fig. V.3.1.1 *The convertible time-domain THz spectrometer in transmission configuration: (BS) - beam splitter, (TE) - THz emitter, (RA) - receiver antenna, (P1) - (P5) - pivotal points, (PM I) - (PM IV) - parabolic mirrors, (SM1) and (SM2) - support optical mirrors, (TCR) - threaded control rod, and (DS) - delay stage.*

V.3.2. Reflection configuration

In order to make the spectrometer transmission-reflection convertible and to enable a smooth change of the incidence angle, all optical elements are installed on an aluminum adjustable frame with five pivotal points (Fig. V.3.2.1). The positions of points 1 and 5 are fixed and points 2, 3, and 4 are movable. In order to ensure that the surface of the mirrors in the pivotal points stays always in line with the rotation axis, a standard 0.5'' mirror mount from Newport Corp. has been modified: an aluminum plate has been introduced between the mirror holder and the support post (Fig. V.3.2.2).

The sample holder is placed at the point 3 so that the sample always stays in the common focus of the paraboloids II and III. The threaded control rod allows smooth movement of the point so that the THz radiation incidence angle is continuously changed from 25° to 80°. The angle variation range is limited from below by the focal lengths of the parabolic mirrors II and III and by the dimensions of their holders. By use of paraboloids with longer focal lengths smaller angles of incidence can be achieved. At small incidence angles, when the optical beams strike the mirrors positioned in P2 and P4 under large angles, it is necessary to employ additional support mirrors SM1 and SM2 to guide the beams.

The use of the adjustable frame guarantees that the optical paths of the pump and probe beams remain unchanged. In order to change the angle of incidence, it is sufficient to laterally readjust only the mirrors at the pivotal points. Moreover, once fixed in the transmission configuration, the four-paraboloid sequence requires no further tedious adjustments.

As a sample holder, we use a modified New Focus flipper mirror mount (Fig. V.3.2.3). The modification consists of two (instead of one) adjustable mirror holder frames being mounted on the flipper perpendicular to each other. A sample is attached to one frame and another one holds a reference silver mirror so that the change between the sample and the mirror is done by flipping the mount.

The total time required for the change of the incidence angle, adjustment of pump and probe beams and the measurement itself does not exceed 15 min.

The precise control of   sample position is a challenging experimental task in time-domain reflection spectroscopy[82]. Similarly to the case of measurement of the complex transmissivity, to obtain the frequency dependence of the complex reflectivity, it is necessary to perform two measurements: of the pulse reflected from a sample and the one reflected from a reference surface. Naturally, the sample and the reference mirror have to be consequently placed in the same point with the maximum precision possible otherwise the phase information would be significantly distorted. Before the start of the reflectivity measurements, the sample and the reference mirror positions are adjusted in a sample holder adjuster (Fig. V.3.2.1). The optical laser beam is picked up before the spectrometer and sent to the sample (or the reference mirror). Steering the reflected beam to make it pass through a narrow aperture we ensure that the sample's surface is set in the same position as the reference mirror with 100 µm precision. Then the holder is installed back to the pivotal point P3. However, in reality the mechanical adjustment is often not sufficient for phase-sensitive measurements. The ways to further improve the phase sensitivity will be discussed in Section V.3.4.
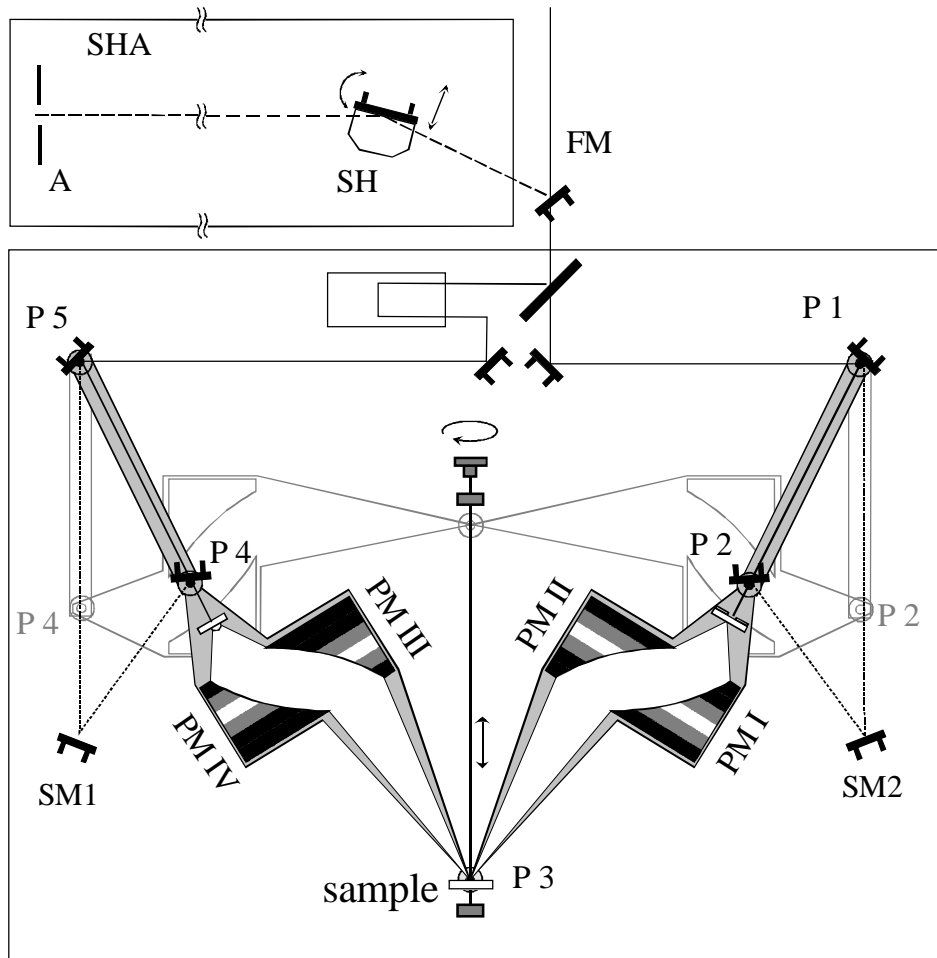
Fig. V.3.2.1. *The reflection configuration: (FM) - flipper mirror, (SHA) - sample holder adjuster, (SH) - sample holder, and (A) - aperture.*
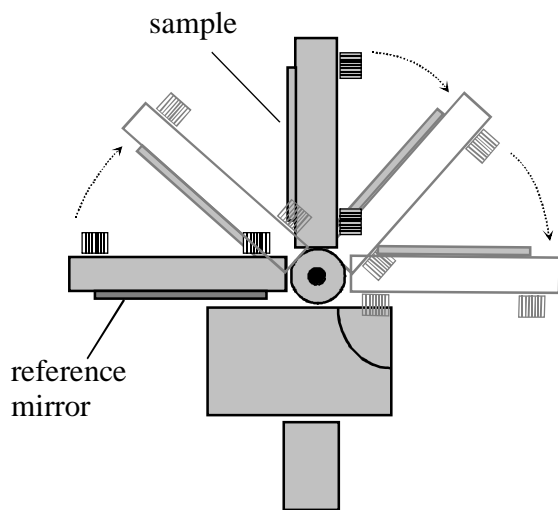
Fig. V.3.2.3. *The sample holder (side view).*

Fig. V.3.2.2. *Modified holder for optical mirrors in the pivotal points.*

V.3.3. Sample measurements and discussion

Measurements of relative complex reflectivity

The effectiveness of the described technique has been tested by measuring the complex transmissivity and reflectivity of a 0.3-mm-thick high-resistivity silicon wafer ($\rho_0 = 10$ kΩ cm). In Fig. V.3.3.1 the time profile of THz pulses for the cases of free-space propagation, transmission through the wafer, and surface reflection are shown.

From transmission data the complex refractive index $n^*(\omega)=n(\omega)+ik(\omega)$ is calculated by numerically solving the Fresnel transmission equation:

$$T^*(\omega) = \frac{4n^* \exp[-i\dfrac{\omega}{c}n^*d]}{(n^*+1)^2\left(1-\left(\dfrac{n^*-1}{n^*+1}\right)^2 \exp[-2i\dfrac{\omega}{c}n^*d]\right)}, \qquad (V.3.3.1)$$
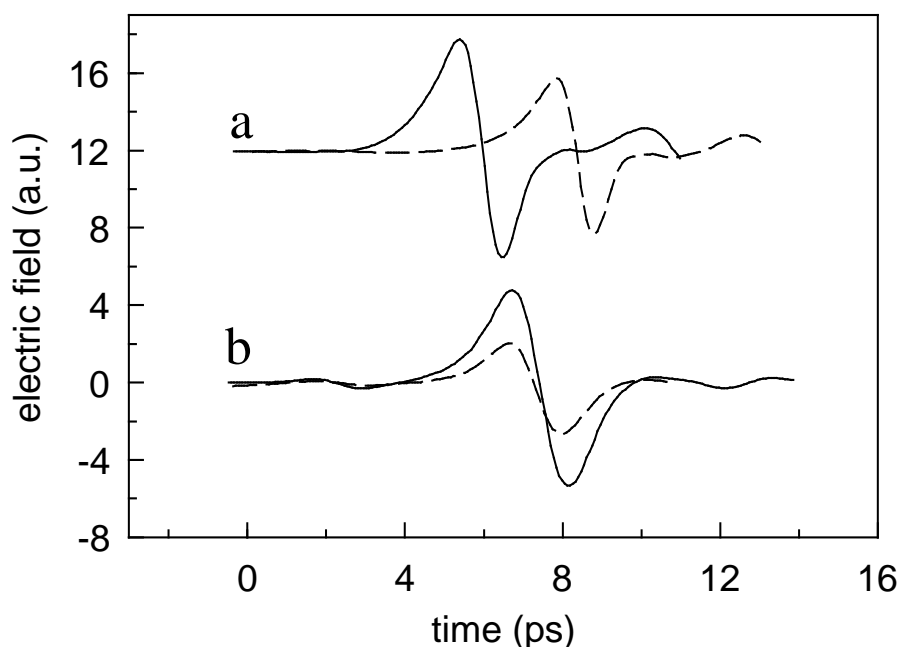
Fig. V.3.3.1. *Time-domain data. (a) Reference, freely propagating pulse (solid line) and pulse transmitted through a silicon wafer (dashed line). (b) Reference, pulse reflected by a silver mirror (solid line) and pulse reflected from silicon wafer surface at 45° incidence (dashed line).*

where d is the thickness of the sample. The complex refractive index spectrum obtained this way is shown in Fig. V.3.3.2. It is seen that the agreement with previously reported data[83] is excellent.
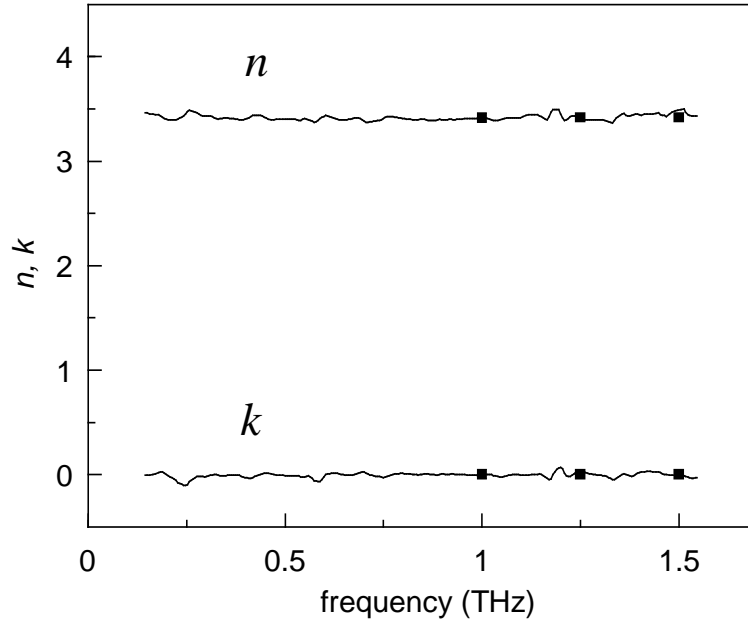
Fig. V.3.3.2*. Frequency dependence of the complex refractive index of high-resistivity silicon calculated from the measured complex transmissivity (solid line) and the data from Ref. 47.*
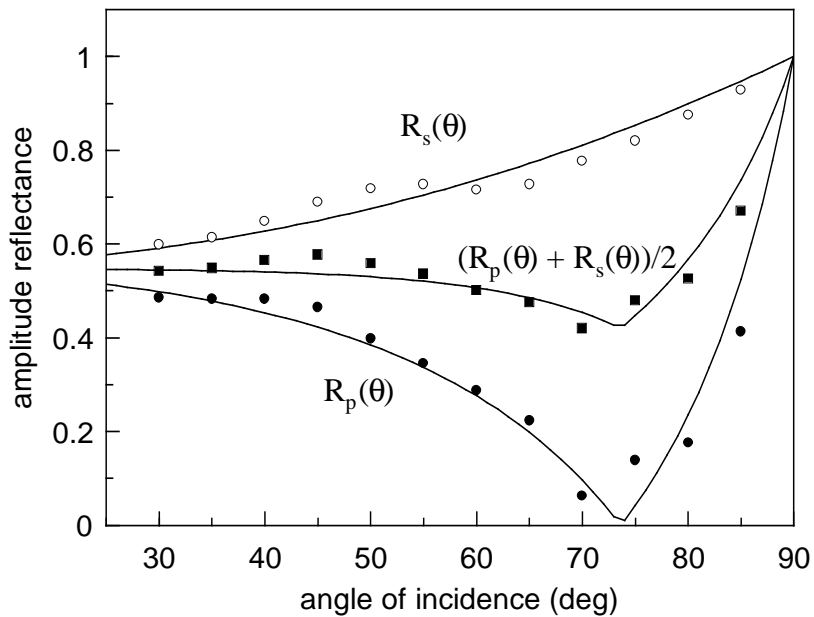
Fig. V.3.3.2*. Amplitude reflectivities of high-resistivity silicon for s- and p-polarizations at 0.4 THz. Solid lines are the ideal Fresnel reflectivities.*

Then these values of n^* have been used for the calculation of the complex reflectivity through the Fresnel formulas[84]:

$$R_P^*(\Theta, n^*(\omega)) = -\frac{n^{*2}(\omega)\cos\Theta - \sqrt{n^{*2}(\omega) - \sin^2\Theta}}{n^{*2}(\omega)\cos\Theta + \sqrt{n^{*2}(\omega) - \sin^2\Theta}}$$

(V.3.3.2)

$$R_S^*(\Theta, n^*(\omega)) = -\frac{\cos\Theta - \sqrt{n^{*2}(\omega) - \sin^2\Theta}}{\cos\Theta + \sqrt{n^{*2}(\omega) - \sin^2\Theta}}$$

(V.3.3.3)

where Θ is incidence angle of the THz radiation, s and p polarizations imply that the THz beam is polarized perpendicular and parallel to the incidence plane.

In order to perform measurements of the reflectivity of s-polarized THz radiation, both the emitter and the detector antenna are turned for 90°.

Fig. V.3.3.3 shows measured amplitude reflectivities compared to the predictions of Eqs. V.3.3.2 and V.3.3.3. The measurements agree very well with the calculations. Some slight deviations of the measured data from the ideal Fresnel reflectivities are attributed to THz radiation being not perfectly p- or s-polarized so that some small fraction of unwanted polarization is always present. This effect manifests itself in a small minimum in $R_S(\Theta)$ and non-zero values of $R_P(\Theta)$ in the vicinity of the Brewster angle ($\Theta_B = 73.7°$).

As has been mentioned in the section V.3.2, the measured phase of the complex reflectivity often needs an additional correction. Uncertainty in the position of a sample with respect to a reference mirror results in the reflected pulse acquiring an additional phase shift φ_0. This leads to errors in the determined refractive index which are particularly large in the case of weakly absorbing materials like silicon (see Fig. V.3.3.4.). The approaches to overcoming the problem are described in the following section.
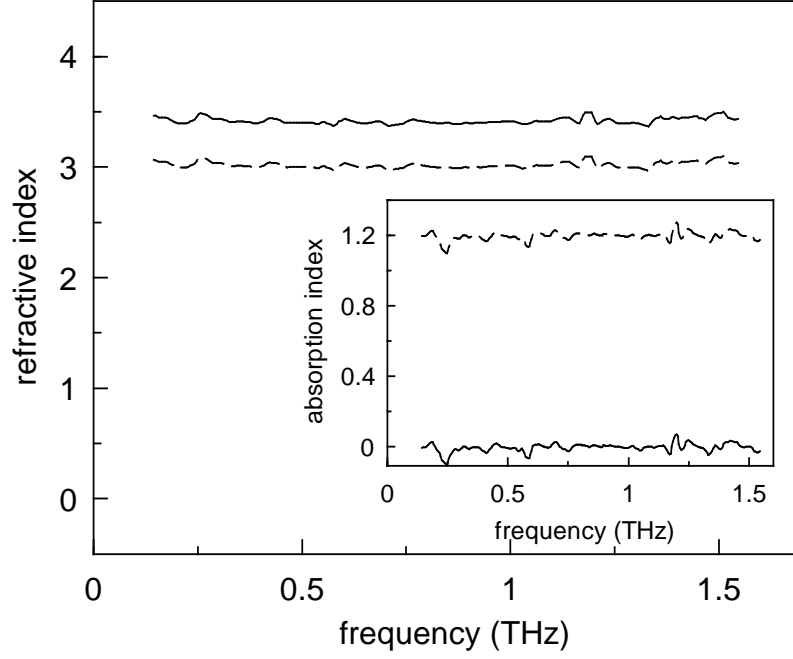
Fig. V.3.3.4. *Refractive index of high-resistivity silicon calculated from the complex reflectivity for s-polarization (45° incidence): as measured (dashed line) and after the correction through (4) (solid line). The corresponding uncertainty in time domain is 48 fs.*

V.3.4. How to deal with phase uncertainty

Numerical correction of phase

Having measured the complex reflectivity for *either* s- or p-polarization, we can get rid of φ_0 with the help of a simple mathematical procedure. We introduce into Eqs. V.3.3.2 and V.3.3.3 a value of $n_0{}^*$ calculated through Eq. V.3.3.1 at some certain frequency ω_1 from measured transmissivity to obtain the corresponding complex reflectivity $R_0{}^*(\omega_1)$. Comparing it to the measured value of $R^*(\omega_1)$, we calculate φ_0 through the expression:

$$e^{i\varphi_0} = \frac{R^*(\omega_1)}{R_0^*(\omega_1)} \qquad\qquad\qquad \text{(V.3.4.1)}$$

and then subtract it from the phase of $R^*(\omega)$ at all frequencies. This method is simple and direct but its drawback is that the usage of Fresnel formulas (Eqs. V.3.3.2 or

66

V.3.3.3) is valid only when the reference surface can be treated as an ideal reflector compared to the sample.

Extraction of the refractive index from amplitude reflectivities

When the reflectivity is measured for *both* s and p polarization, the system of equations V.3.3.2 and V.3.3.3 is then solved in terms of *amplitude* reflectivities $|R_S^*(\omega)|$ and $|R_P^*(\omega)|$ to extract $n^*(\omega)=n(\omega)+ik(\omega)$. Now it is not necessary to calculate φ_0 but the supposition of the ideal reflectance of the reference surface should still be made.

Reference-free measurements

In principle, the polarization sensitivity of the THz emitter and the detector antenna allows the reference-free extraction of the complex refractive index of a sample's material. At some certain incidence angle Θ, instead of measurement of $R_S^*(\omega)$ and $R_P^*(\omega)$ which actually implies the scan of four time profiles (pulses reflected from the sample and the reference surface for either polarization), one obtains a complex function $\rho_{PS}^*(\omega)$ as a ratio of Fourier transforms of time profiles of the pulses reflected from the sample at s and p polarizations:

$$\rho_{PS}^*(\omega) = \frac{E_P^*(\omega)}{E_S^*(\omega)} \qquad (V.3.4.2)$$

or

$$\rho_{PS}^*(\omega) = \frac{R_P^*(\omega)}{R_S^*(\omega)}. \qquad (V.3.4.3)$$

The numerical solution of Eq. V.3.4.3 using Eqs. V.3.3.2 and V.3.3.3 yields the spectrum of the complex refractive index $n^*(\omega)$. This approach is free from the problems of non-ideal reference surface and the φ_0 but requires precise mechanics,

67

which guarantees that the rotation of the emitter and the detector does not change the optical path of THz radiation for more than a few microns.

In fact, $\rho_{PS}^*(\omega)$ is nothing else than the ellipsometric function. Here we come directly to the idea of a time-domain THz spectroscopic ellipsometer, a promising new instrumentation that I propose. It will be presented in Section IX.1.1.

Outlook

A number of further improvements can enhance the performance of the spectrometer and make it even more flexible. The upper frequency limit is given by the detector antenna. State-of-the-art THz antennas are able to detect frequencies as high as 5 THz (Ref. 85). By replacement of free-space optics by a fiber-optic system similar to that offered by Picometrix, Inc. a spectrometer requiring no readjustments at all can be created. To enable low-temperature measurements, a continuous-flow cryostat or bath cryostat rather than a close-cycled one should be chosen since high amplitude vibrations of the latter make the precise positioning of a sample difficult.

VI. PROPAGATION OF THZ PULSES

In order to focus the terahertz radiation on a detector, eventually on a smaller-size sample, FIR optics like mirrors or lenses are to be employed. Consequently, it is worth to know in detail how the temporal waveform and the spectrum of the pulses are altered due to these spatial transformations.

The pulsed THz radiation does not propagate as a plane wave. On the contrary, a THz beam has a pronounced radial distribution of frequency components, which makes THz waveforms and their spectra very sensitive to the influence of focusing optics and apertures and even to free space propagation.

The half-cycle terahertz beam transformations were first theoretically described in the frame of Gaussian beam optics by Ziokowski *et al.* (Ref. 86). Kaplan[87] then extended this approach to pulses with arbitrary time profiles. Jepsen *et al*. (Ref. 88) used the *ABCD* matrix formalism for the simulations of the THz beam propagation. You and Bucksbaum (Ref. 89) used this formalism to calculate numerically the changes of time profile and spectra of the pulses due to the transformations by a lens or a mirror. Feng *et al.* (Ref. 90) elucidated the role of the phase shift (also called *Gouy shift*[*]) near the focal plane in the reshaping of pulses. More recently, Gürtler *et al.* (Ref. 91) have performed detailed numerical simulations of the near- and far field propagation of THz radiation and presented a spectacular dynamic graphics.

We have performed a detailed experimental study of the spatio-temporal transformations of ultrashort THz pulses and we quantitatively compare the results to the theoretical predictions. Our approach is predominantly analytical and it allows us to describe not only the propagation of THz beams in free space but also the influence of focusing optics and to take into account the finite size of optical elements.

---

[*] The effect is named after L.G. Gouy who first observed changes in the light interference pattern under the influence of focusing optics (L.G. Gouy, C. R. Acad. Sci. Paris **110**, 1251 (1890)).

VI.1. Theoretical description: gaussian beams

Our theoretical description holds on the gaussian beam propagation formalism[92]. When possible, analytical expressions were derived and the effects related to the dephasing of the frequency components within the pulse bandwidth were distinguished from the effects related to the spectral filtering owing to the beam diffraction and to its aperturing by the optical elements.

In the following, $E(t)$, $e(\nu)$ are denoted as the Fourier pair of the THz electric field waveform:

$$e(\nu) = \int_{-\infty}^{\infty} E(t) \exp(-2\pi i \nu t)\, dt \tag{VI.1.1}$$

VI.1.1. Dephasing of spectral components: simple insight

Let us consider the case when each frequency component $e(\nu)$ within the THz pulse bandwidth acquires an equal phase shift θ. This can occur, for example, by a reflection on an interface or as a consequence of the propagation of a gaussian beam between its waist and a distant point (in the last case $\theta = \pi/2$). Physically, it means that the spectral components oscillating originally in phase and thus forming an ultrashort pulse will get dephased (they are shifted by the same fractions of λ, which correspond to different temporal or spatial shifts). Although the amplitude spectrum does not change due to this transformation, the temporal waveform of the THz electric field can be significantly modified. The new waveform is given by:

$$E'(t) = \int_{-\infty}^{\infty} e(\nu) \exp(i\theta \operatorname{sign}(\nu)) \exp(2\pi i \nu t)\, d\nu \tag{VI.1.1.1}$$

The term sign(ν) arises from the condition that the corresponding time-domain response function must be real. After having performed the inverse Fourier transform, one obtains:

$$E'(t) = E(t)\cos\theta - \frac{\sin\theta}{\pi}\left[E(t) * \mathrm{vp}\tfrac{1}{t}\right],$$

(VI.1.1.2)

where vp stands for the principal value of the integral. For example, the phase shift of $\theta = \pi/2$ transforms a unipolar half-cycle pulse into a significantly longer (because of $1/t$ tails) bipolar single-cycle pulse with the same amplitude spectrum:

$$E'(t) = -\frac{E(t)}{\pi} * \mathrm{vp}\frac{1}{t}$$

(VI.1.1.3)

This very simple calculation shows that one can really expect spectacular changes in the pulse shape related to the transformations by focusing optics: if the distance between the beam waist and a lenses (or focusing mirror) is much longer than the confocal parameter z_0 for all relevant wavelengths, then the phase change acquired by the pulse during the propagation between the lens (mirror) and the waist is $\pi/2$ (or $3\pi/2$ in the case of a mirror) and the phase change between the waist and the far field is $\pi/2$.

VI.1.2. Free-space propagation

For the sake of simplicity, the analysis will be concentrated only on the on-axis field. Within the gaussian-beam approximation, one can write down:

$$e(\nu; z) = e_0(\nu)\frac{w_0}{w(z)}\exp\left\{-i\left[kz - \arctan(z/z_0)\right]\right\},$$

(VI.1.2.1)

where

$$w^2(z) = w_0^2 \left[1 + (z/z_0)^2 \right] \quad , \quad z_0 = \frac{\pi w_0^2}{c} \nu$$

(VI.1.2.2)

$e_0(\nu)$ determines the near field waveform of the pulse and depends on the optical pump beam profile and the physical properties of the emitter. The waist of the THz beam for all the transmitted frequencies is supposed to be located on the emitter area: this is a reasonable assumption for the usual case when the pump optical beam is not extremely convergent or divergent. Additionally, w_0 is assumed to be equal to one half of the gap between the emitter's electrodes for all wavelengths. Introducing Eq. (VI.1.2.2) to (VI.1.2.1) gives immediately:

$$e(\nu;z) = e_0(\nu)\Phi(\nu;z)\frac{1}{1 - i\frac{\alpha(z)}{\nu}} ,$$

(VI.1.2.3)

where $\Phi(\nu;z) = \exp(-2\pi i\,\nu z/c)$ is a propagator, and

$$\alpha(z) = \frac{c}{\pi w_0^2} z$$

(VI.1.2.4)

The resulting temporal waveform then reads:

$$E(t;z) = E_0\left(t - \tfrac{z}{c}\right) * \left[\delta(t) - 2\pi\alpha Y(t)\exp(-2\pi\alpha t)\right]$$

(VI.1.2.5)

where $Y(t)$ is the Heaviside unit-step function and $\delta(t)$ is the Dirac delta-function. The shape of the function in the square brackets can be easily studied: it is obvious that a half-cycle unipolar pulse in the near field leads to a one-cycle bipolar pulse in the far field, a one-cycle pulse in the near field is transformed to one-and-half-cycle pulse in the far field etc. Note also that

$$\lim_{a\to\infty} aY(t)\exp(-at) = \delta(t),$$

i.e. the on-axis field vanishes for $z \to \infty$ due to the divergence of the beam. It also directly follows from (VI.1.2.3) that when $z \gg z_0$ (i.e. $\alpha \gg \nu$) throughout the whole pulse bandwidth, the Eq. (VI.1.2.5) reads simply as:

$$E(t,z) = \frac{1}{2\pi\alpha} \frac{\partial E_0\left(t - \frac{z}{c}\right)}{\partial t} \qquad \text{(VI.1.2.6)}$$

The amplitude of the far field is indirectly proportional to z (through α), as expected, and the far-field time profile is the first derivative of the near-field waveform. This result is in an analogy with the near and far field radiation characteristics of an oscillating dipole, as it was discussed for the case of the terahertz emission from a Hertzian dipole antenna[93] and for a large-aperture biased emitter[94].

VI.1.3. Influence of focusing optics and apertures

The changes introduced by focusing optics into spatial properties and temporal profiles of terahertz pulses can be well described using the ABCD matrix formalism[92]. In the following, the beam parameters before the transformation by an optical element are denoted w_0 (beam waist size), z_0 (confocal parameter), and L (distance between the waist and a lens or a mirror); the parameters transformed through an optical element without taking into account its aperture will be primed (w'_0, z'_0, L') and the transformed parameters where the optics aperture was included into the calculation will be double-primed (w''_0, z''_0, L''). Let us consider a lens with the focal distance f and a sufficiently large aperture. For the transformed parameters we then obtain:

$$L' = \frac{f\left(L^2 + z_0^2\right)\left(L^2 + z_0^2 - fL\right)}{\left(L^2 + z_0^2 - fL\right)^2 + f^2 z_0^2} \;, \qquad\qquad w'_0 = w_0 \sqrt{\frac{L'f}{\left(L^2 + z_0^2 - fL\right)}} \qquad \text{(VI.1.3.1)}$$

However, for such long-wavelength and broadband radiation, as a pulsed THz beam is, it is necessary to take into account the lens aperture (denoted A). In our simple

model, the aperture is introduced in the following way: (*i*) if the beam size at the lens is smaller then its aperture, i.e. $w(L, \lambda) < A/2$, then the beam is considered unaffected by the finite lens size, (*ii*) if the beam size at the lens is larger then its aperture, i.e. $w(L, \lambda) > A/2$, then the transformed beam size close to the lens is set to $w''(-L'', \lambda) = A/2$. It will be shown that such a cut-off leads to an effective wavelength filtering in the beam waist position.

The beam parameters after the transformation and the cut-off take the form:

$$\nu > \nu_m : \qquad L'' = L', \qquad\qquad w_0'' = w_0' \qquad\qquad\qquad \text{(VI.1.3.2a)}$$

$$\nu < \nu_m: \qquad L'' = \frac{f\left(L^2 + z_0^2\right)\left(L^2 + z_0^2 - fL\right)}{\left(L^2 + z_0^2 - fL\right)^2 + f^2 z_0^2 \left[\left(\frac{2w_0}{A}\right)^2\left(\frac{L^2}{z_0^2} + 1\right)\right]^2}, \qquad \text{(VI.1.3.2b)}$$

$$w_0'' = w_0 \sqrt{\frac{L''f}{\left(L^2 + z_0^2 - fL\right)}\left[\left(\frac{2w_0}{A}\right)^2\left(\frac{L^2}{z_0^2} + 1\right)\right]}$$

where $\nu_m = \alpha(L)\left[(2w_0/A)^2 - 1\right]^{1/2}$. The parameter α was defined by Eq. (VI.1.2.4).

In the area of the beam optics validity (i.e. when $L, |L-f|, f \gg z_0$) and if, moreover,

$$\left|\frac{fL}{L-f}\right| \ll \frac{\pi(A/2)^2}{\lambda} \qquad\qquad\qquad\qquad \text{(VI.1.3.3)}$$

the formulas (VI.1.3.2a, b) are reduced to the simple relations:

$$\nu > \nu_m: \qquad L'' = \frac{fL}{L-f}, \quad w_0'' = w_0 \frac{L''}{L} \qquad\qquad \text{(VI.1.3.4a)}$$

$$\nu < \nu_m: \qquad L'' = \frac{fL}{L-f}, \quad w_0'' = \frac{2cL''}{\pi A \nu} = w_0 \frac{L''}{L}\frac{\nu_m}{\nu} \qquad \text{(VI.1.3.4b)}$$

$$\nu_m = \alpha(L)\frac{2w_0}{A}$$

In the general case, the changes in the spectrum due to the transformation can be expressed as:

$$e(v,z) = e_0(v) \frac{w_0}{w''(z)} \frac{w''(-L'')}{w'(-L')}$$

$$\times \exp\{i[\arctan(L/z_0) - \arctan(-L''/z_0'') + \arctan(z/z_0'')]\}$$

(VI.1.3.5)

where z stands for the distance between the detection sensor and the transformed beam waist position. For simplicity, we have omitted the propagator term Φ; the term $w''(-L'')/w'(-L')$ accounts for the continuity of on-axis amplitude after having passed through the lens aperture. Using the condition $w(L)=w'(-L')$ fulfilled for all wavelengths, we can express the equation (VI.1.3.5) in a compact form (reflection on a mirror is described by the same expression multiplied by -1):

$$e(v;z) = \frac{e_0(v)}{1 - i\frac{\alpha(L)}{v}} \frac{1 + i\frac{\alpha''(L'')}{v}}{1 - i\frac{\alpha''(z)}{v}},$$

(VI.1.3.6)

where $\alpha''(z) = cz/(\pi w_0''^2)$. The first fraction on the right hand side simply describes the free space propagation before the lens [see Eq. (VI.1.2.3)], the second fraction is responsible the transformation by the lens and subsequent propagation in the free space. Additional focusing optical components can be accounted for by multiplication of the right-hand side by similar fractions. Thus, the Eq. (VI.1.3.6) can be rewritten in a recurrent form that is very convenient for computer simulations of complex optical paths:

(VI.1.3.7)

$$e^{(n)}(v,z) = \frac{e^{(n)}(v,0)}{1 - i\frac{\alpha_n(z)}{v}}$$

$$e^{(n+1)}(v,0) = e^{(n)}(v, L_{n+1} = D_n - L_n)\left[1 + i\frac{\alpha_{n+1}(L''_{n+1})}{v}\right]$$

phase shift:	$-\pi/2$	0	$\pi/2$	π	$3\pi/2$	2π
low frequency filter:	$1/\nu$	1	ν	1	ν	1
high frequency filter:	$1/\nu$	1	$1/\nu$	1	$1/\nu$	1
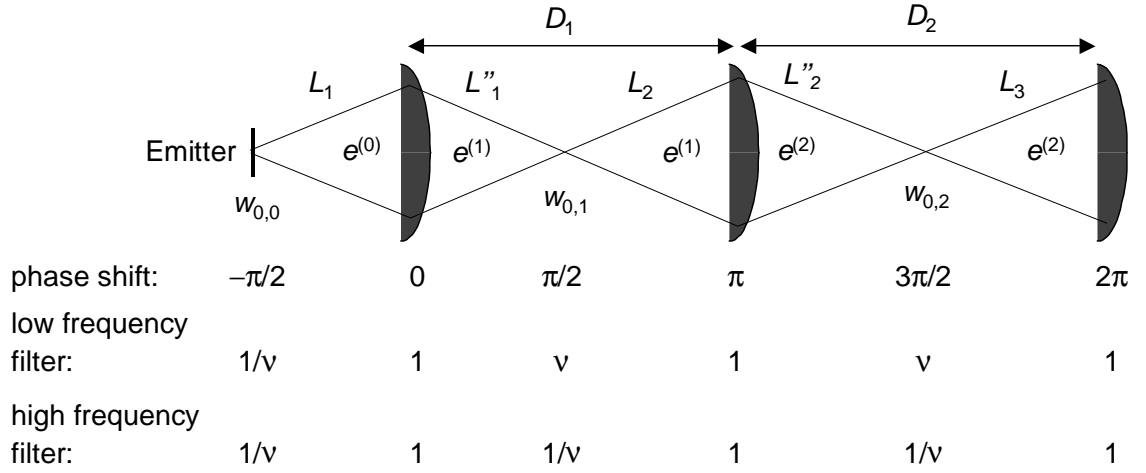
Fig. VI.1.3.1. *Scheme of phase shifts and effective amplitude filters due to propagation of the THz pulse through a set of finite-size lenses (far field).*

where $\alpha_n(z)$ depends on the beam waist $w_{0,n}$ [Eq. (VI.1.2.4)], $e^{(n)}$ is the field between n-th and $(n+1)$-th lenses, D_n is a distance between them, and L_n is a distance between the n-th lens and the preceding beam waist: L_n and L''_n are related by Eq. (VI.1.3.4); the meaning of the symbols and variables is illustrated in Fig. VI.1.3.1.

The only difficulty arises from the fact that, in general, the parameters L_n, α_n $(n>1)$, and L''_n are frequency-dependent as it follows from the Eqs. (VI.1.3.1) and (VI.1.3.2). Consequently, it is impossible to find a general form of the temporal profile of the transformed pulse. On the other hand, one can easily study a particular case, which is often applicable for the main part of the transmitted spectrum: it is the case when the approximate formulas (VI.1.3.4) can be applied for the beam transformations, i.e., the beam optics approximation is valid for all the spectral components. In fact, the condition (VI.1.3.3) is never satisfied for the longest wavelengths but they are always efficiently filtered out due to the diffraction and the aperture effect. Then the waist position does not depend on the wavelength and we obtain for the electric field in the far field (near the lenses) and in the waist:

$$e^{(n)}(\nu, L_{n+1}) \equiv e^{(n+1)}(\nu, -L''_{n+1}) = e^{(n)}(\nu, 0)\frac{i\nu}{\alpha_n(L_{n+1})} \tag{VI.1.3.8a}$$

$$e^{(n+1)}(v,0) = e^{(n+1)}\left(v,-L''_{n+1}\right)\frac{iF_n(v)}{v}\alpha_n\left(L_{n+1}\right)$$

<div style="text-align: right;">(VI.1.3.8b)</div>

$$e^{(n+1)}(v,0) = -e^{(n)}(v,0)F_n(v),$$

<div style="text-align: right;">(VI.1.3.8c)</div>

where $F_n(v)$ is amplitude filter related to the aperture of the n-th lens and is given by the relations:

$$v > v_m: \qquad F_n(v) = \frac{L_n}{L''_n}$$

$$v < v_m: \qquad F_n(v) = \frac{L_n}{L''_n}\left(\frac{v}{v_m}\right)^2$$

The profile of the filter is a direct consequence of our manner of the lens aperture introduction into the calculation. In particular, this filter has a discontinuous derivative at $v = v_m$ and therefore it provides an artificial oscillation in the time domain. The field in the time domain is given by:

$$E^{(n+1)}(t) = -\frac{L_n}{L''_n}E^{(n)}(t) * \left[\delta(t) + 4v_m\left(\frac{\cos(\omega_m t)}{(\omega_m t)^2} - \frac{\sin(\omega_m t)}{(\omega_m t)^3}\right)\right]$$

<div style="text-align: right;">(VI.1.3.9)</div>

where $\omega_m = 2\pi v_m$. The singularity in the filter frequency profile can be removed by choosing a different profile (e.g., a gaussian-like filter), thus the oscillations of $\sin x/x$-like functions can be avoided. However, essential characteristics of the filter — its quadratic behavior in the low-frequency limit and frequency independence in the high-frequency limit — have to be preserved. A more detailed study of the expression (VI.1.3.9) shows that the main features of the pulse shape in the beam waist are similar (as the quadratic low-frequency filtering suggests) to the second derivative of the near field at the emitter; practically, the filter adds one half-cycle to the far field waveform.

If one chooses the far field spectrum as a reference that provides the main characteristics of a particular emitter, then, as the Eq. (VI.1.3.8b) suggests, the spectral bandwidth in the beam waists will be narrower: it is a result of an effective linear low frequency and a 1/ν high frequency filtering. The final picture of the transformations through a set of lenses within the current approximation is depicted in Fig. VI.1.3.1. The pulse characteristics are related here to the far field spectrum. The phase shift is always incremented by π/2 between the waist and the far field and effective low- and high-frequency filters occur in the beam waists.

VI.2. Experimental study of spatio-temporal transformations of pulsed THz radiation

The experimental setup shown schematically in Fig. VI.2.1. was essentially very similar to that in Hamburg (see section V.2). The major difference was the THz optical part, which could be either empty space or a polyethylene lens or a couple of *elliptical* aluminum mirrors. The laser was a Lexel 480 Ti:sapphire oscillator with pulse length of 100 fs, central wavelength of 815 nm, repetition rate of 76 MHz, and average power of about 400 mW.

THz pulses were generated by a large-aperture photoconducting antennas made of pure GaAs, semi-insulating GaAs:Cr or InP:Fe which were believed to have large free carrier lifetimes and, consequently, to provide very short half-cycle THz pulses. We verified, through time-resolved reflectivity experiments, that the lifetimes are at least of the order of several tens or hundreds of picoseconds. The emitters were endowed with golden electrodes with several different spacings (from 3 to 8 mm). The average photocurrent between the emitter electrodes was quite high (typically 1 mA for 800 V and 3 mm electrode spacing in GaAs, slightly larger for InP) due to the large free carrier lifetime of the emitters, therefore the emitters were cooled by the cold air flow.
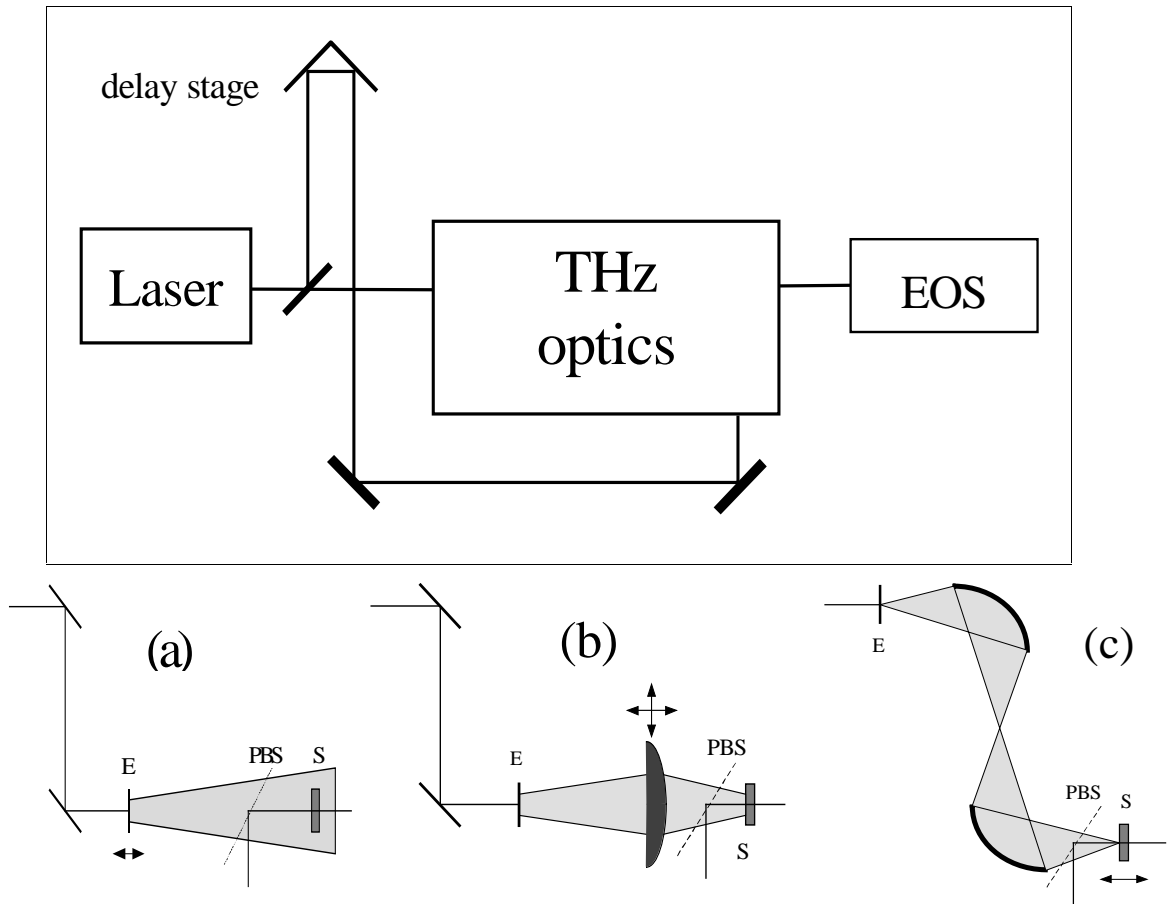
Fig. VI.2.1. *Schematic of the experimental setup. The legend: EOS – electro-optic sampling detection system, E – THz emitter, S – sensor crystal, PBS - pellicle beam splitter. Not shown are a half-wavelength plate and a polarizer in the probe branch. Three versions of the THz optics arrangement: (a) free space propagation (emitter – sensor distance variable); (b) focusing with a soothed polyethylene lens (lens position variable); (c) focusing with a pair of ellipsoidal mirrors with one common focus (second mirror – sensor distance variable).*

The electro-optic sampling technique (Section IV.2) with a <110> ZnTe sensor crystal of an effective thickness of about 0.3 mm (estimated from the real measured thickness and a residual absorption in the THz spectral range) was employed for the time-resolved detection of the pulses. The temporal resolution of the detection system was at least 50 fs.

For the study of the free-space propagation of THz pulses the THz spectrometer was arranged so that there was no optical elements between the emitter and the sensor crystal (Fig. VI.2.1a) and the emitter – sensor distance l_{e-s} were set variable. All the used emitters delivered similar signals: unipolar pulses with duration shorter than

400 fs. In the frequency domain, the non-zero spectral density extended up to 2.5 or 3 THz. The GaAs:Cr emitter was selected for the subsequent measurements mainly because of the lowest average photocurrent and thus smaller heating of the emitter. The waveforms for several emitter – sensor distances $l_{e\text{-}s}$ (from 4.5 cm up to 22.5 cm) have been measured. Those displacements resulted neither in pulse shape changes nor in their spectral profile distortions. Fig. VI.2.2 shows the dependence of the peak value of the waveform and the integrated spectral amplitude of the signal on $l_{e\text{-}s}$ for the emitter with 3 mm electrode spacing. Both curves fit very well to $1/l$ dependence indicating that, following Eq. (VI.1.2.6), the far field radiation is measured. This is in agreement with the theory that predicts the frequency component of 1 THz reaching the far field approximation at the distance of about 3 cm from the emitter. Emitters with significantly larger spacings between electrodes delivered much smaller signal amplitudes and therefore we were not able to follow quantitatively what happens when the $l_{e\text{-}s}$ distance varies.

In the second series of experiments (Fig. VI.2.1b), the emitter with 3 mm electrode spacing was used, $l_{e\text{-}s}$ distance was fixed to 22.5 cm, and a soothed polyethylene plano-convex lens (f=4.3 cm) with one spherical surface was put between the emitter and the sensor. Waveforms were taken for different positions of the lens. During
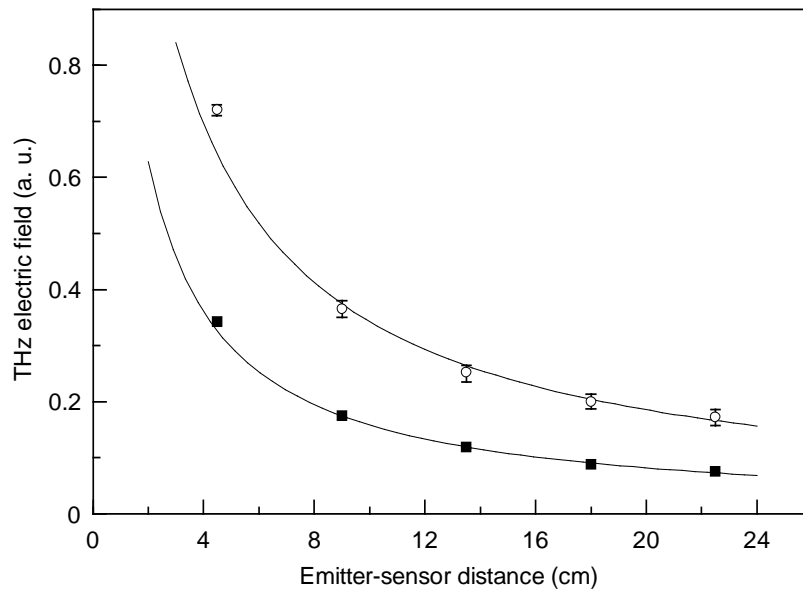

Fig. VI.2.2. *Peak values of the waveforms (■) and integrated amplitude spectrum values (○) as a function of the emitter – sensor distance. Solid lines: fits with ~1/ $l_{e\text{-}s}$ function.*

these experiments the spherical surface of the lens was directed towards the sensor and the distances (emitter – lens l_{e-l} and lens – sensor l_{l-s}) were carefully evaluated: the position of the principal points of the lens was taken into account. One set of measurements is shown in Fig.VI.2.3. The first waveform denoted as reference, was taken without the lens for $l_{e-s}=7$ cm and was used for the numerical simulations. It was introduced through the numerical Fourier transform to the Eq. (VI.1.3.6) and the waveforms expected for various l_{e-l} were then calculated and compared to the profiles measured experimentally. Several points should be emphasized. (*i*) The amplitude and the time delay of the reference pulse were adjusted in order to correspond [after the transformation through Eq. (VI.1.3.6)] to the amplitude and the time delay of the experimental waveform taken for $l_{e-l}=3.9$ cm. (*ii*) No further modifications of the amplitude and delay were made for other studied emitter – lens distances (except for $l_{e-l}=15.9$ and 16.9 cm which will be discussed separately later). (*iii*) The distances $l_{e-l}=5.8$ and 16.3 cm correspond to the situation when the sensor is placed exactly in the waist position of the transformed beam. For l_{e-l} greater than 5.8 cm and smaller than 16.3 cm the pulse passes through the waist before entering the sensor: this is the reason why the polarity of the signal is opposite to that of the reference pulse. (*iv*) Evidently, the measured pulse shape and even its intensity correspond very well to the predictions.
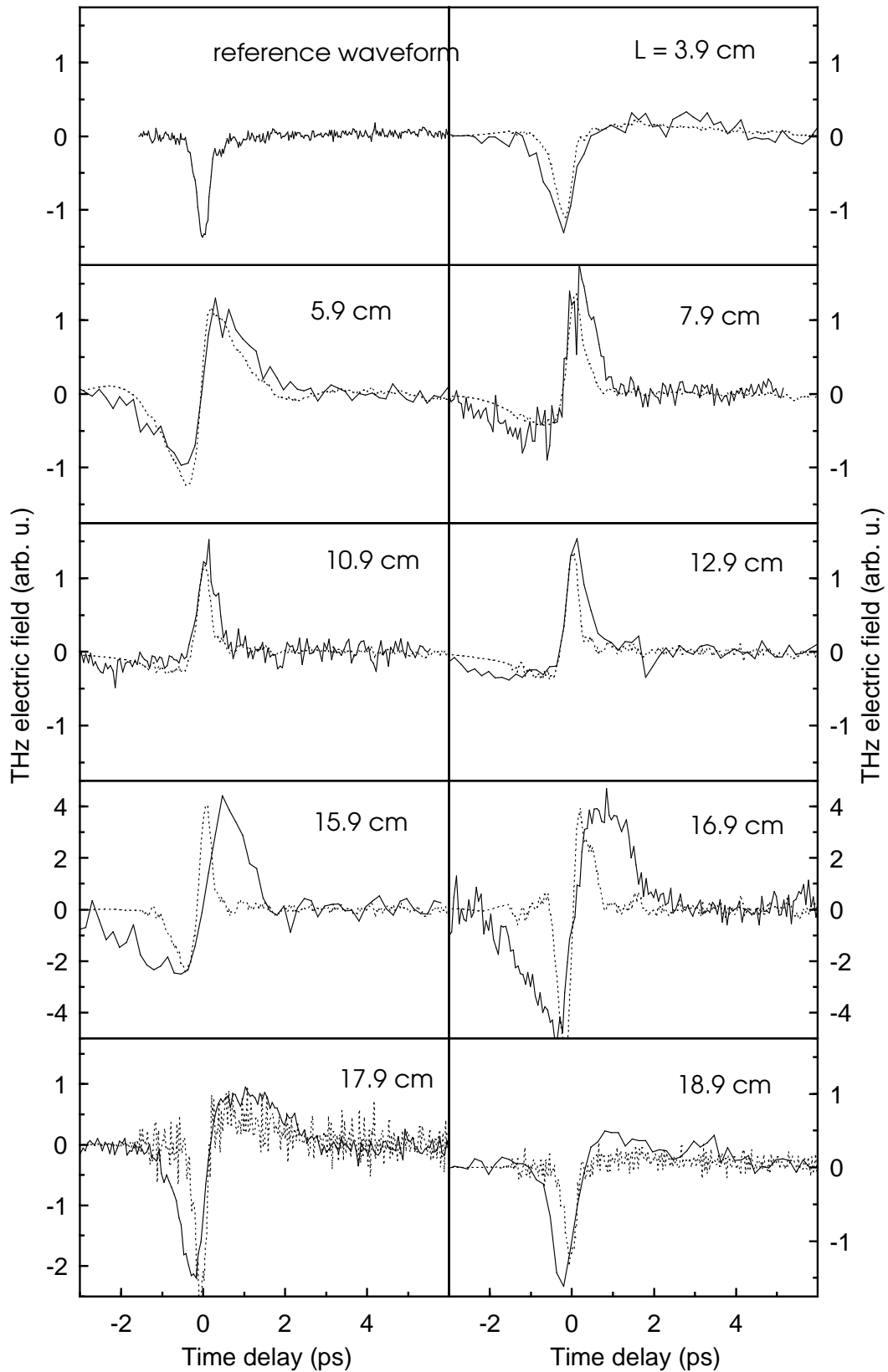
Fig. VI.2.3. *Solid lines: waveforms taken using the setup pictured in f Fig. VI.2.2b (the emitter – lens distance is indicated in the figures). Dotted lines: simulations based on the numerical Fourier transform of the formula (VI.1.3.6); a reference waveform taken in the free-space propagation measurements alignment was used in the calculation to simulate $e_0(v)$.*

One finds 2 major discrepancies for the waveforms taken at $l_{e-l}=$15.9 and 16.9 cm. (*i*) The intensity of the measured signals had to be multiplied by 4.5 and 7, respectively, in order to correspond to the results of the simulations (Fig. VI.2.3 shows the multiplied version of the experimental curves). (*ii*) The pulses obtained experimentally are much longer than the pulses resulting from the calculations. For both distances, the image of the emitter is found to be very close to the sensor and, moreover, it is reduced more than 2.5 times for high frequencies ($v \geq v_m \approx 800$ GHz for the particular experimental parameters) while its size increases for lower frequencies. It means that a very small lateral shift of the focusing lens out of the centered on-axis position should significantly reduce the spectral density at high frequencies that could explain the observed discrepancy. In order to check this hypothesis we set $l_{e-l}=$16.2 and moved the lens laterally. The results are presented in Fig. VI.2.4. It is clearly seen how both discrepancies are removed when the lens is centered more precisely on the beam path. The distance from the correct laterally centered position for the measurements taken at $l_{e-l}=$15.9 and 16.9 cm was about 1 mm.
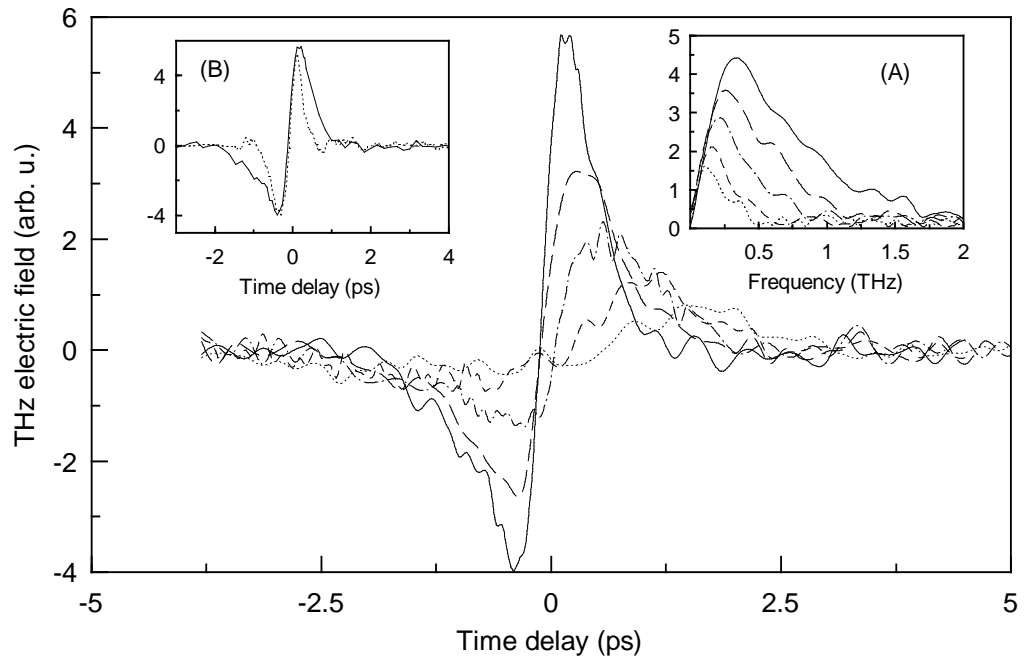
Fig. VI.2.4. *THz waveforms obtained by sliding the polyethylene lens along the lateral (x) direction for l_{e-l}=16.2 cm. (———) pulse corresponding to the best alignment, i.e. x =0; (—— ——) x =0.75 mm; (– · – ·) x =1.25 mm; (– – –) x =1.75 mm; (· · ·) x =2.25 mm. Inset (A): corresponding amplitude spectra. Inset (B): comparison of the best alignment pulse and the model predictions (as described for the Fig. Vi.2.3).*
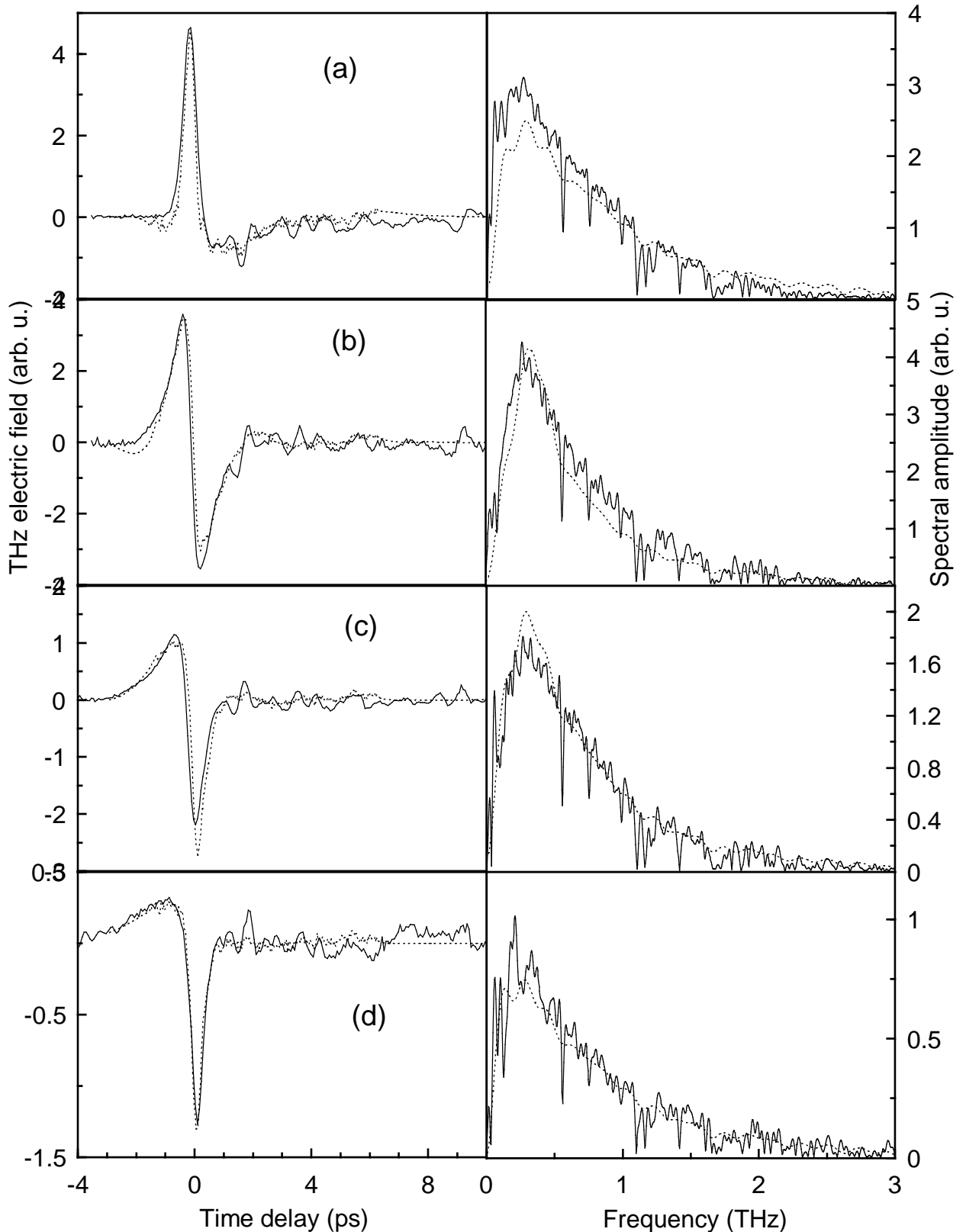
Fig. VI.2.5. *THz waveforms and corresponding spectra obtained with 3 mm emitter in the setup with 2 ellipsoidal mirrors for 4 different l_{m-s}. Dotted lines: simulations obtained from the reference waveform (same as in Fig.VI.2.3) based on the Eqs. (VI.1.3.7) for two mirrors. l_{m-s} in centimeters: (a) experimental 11.5, model 13.5; (b) exp. 15, model 15; (c) exp. 19, model 16.5; (d) exp. 26, model 20.*

Finally, in the third series of experiments (Fig. VI.2.1c), a pair of aluminum ellipsoidal mirrors with equal effective focal lengths ($f=7.5$ cm for 45° incidence) was introduced into the THz beam path so that the emitter was placed in one focus of the first mirror, one focus was common for both mirrors (the place for a small sample in spectroscopic applications) and the sensor was positioned near the other focus of the second mirror. Then the mirror – sensor distance l_{m-s} was scanned. The experimental results and the results of simulations for the emitter with 3 mm electrode spacing are presented in Fig. VI.2.5. The sharp absorption lines in the measured spectra correspond very exactly to the water vapor rotational transitions discussed in more detail in the next section. The theoretical curves were calculated starting from the same reference waveform as for the lens experiments and again the amplitude and time delay of the reference waveform were fixed for all the simulations. The agreement with the experiment is excellent for $l_{m-s}=15$ cm (sensor exactly in the focus of the second mirror; Fig. VI.2.5b). We can also get a very good agreement between the experiment and theory for the other positions of the sensor (see Fig. VI.2.5a, c, and d) but the distance l_{m-s} introduced into the model should differ systematically from the experimental one.

We repeated the set of experiments using a larger emitter (6 mm). The related experimental data and the results of the model are shown in Fig. VI.2.5. First, one can remark that the detected bandwidth is narrower and shifted to lower frequencies than in the case of 3 mm emitter: it is mainly due to the fact that the limit frequency ν_m is decreased approximately by a factor of 2 in the setup with larger emitter. Secondly, we verified that in the case of 3 mm emitter, the approximate expressions (VI.1.3.4) can be used in the calculations and lead to the waveforms which satisfactorily fit the experimental results; however, in the case of the 6 mm emitter the agreement is poorer within the beam optics approximation. Thirdly, it is clear that the agreement between the theory and experiment is achieved if the same distance mismatch as for smaller emitter is supposed. We verified that within our model there is no parameter which, when being varied around its experimental value, could compensate the distance mismatch. On the other hand, we did not find any distance mismatch for the spherical lens case. It thus seems that the problem should be related to the ellipticity of the mirrors.
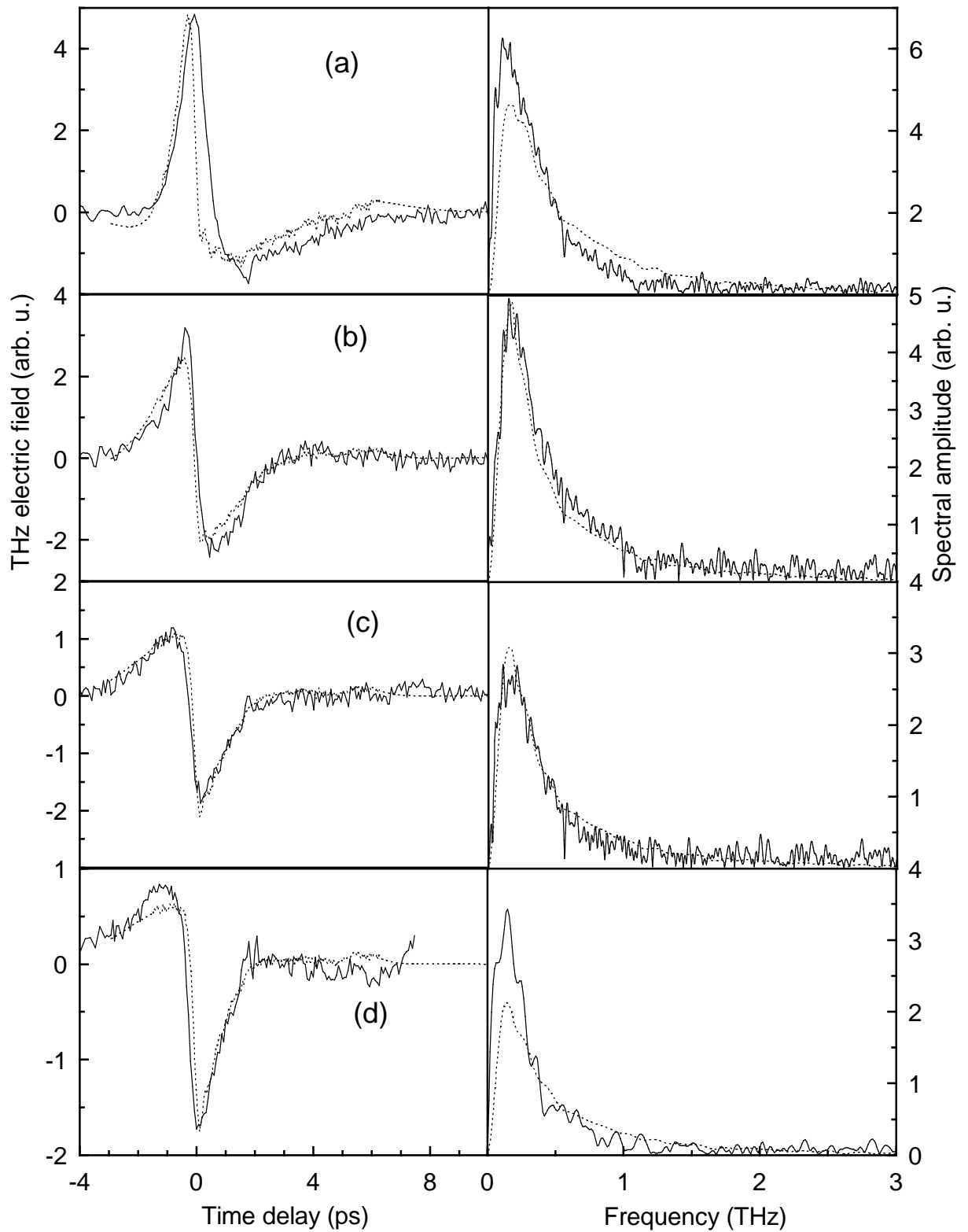
Fig. VI.2.6. *THz waveforms and corresponding spectra obtained with 6 mm emitter. All other parameters are the same as in the legend of Fig. VI.2.5, except $l_{m\text{-}s}$ in the case (d): experimental 26 cm, model 19 cm.*

We chose these mirrors because they are free of the very large astigmatism that would be introduced by the spherical ones for 45° incidence: the effective focal distance *f* is the same for tangential and sagittal plane.

In fact, our experiment suggests that the beam remains in a state close to its waist state on a longer distance than a gaussian beam does and that at even longer distances it diverges faster (in order to fit the mirror aperture). The ellipticity of the mirrors introduces a radial distribution of the radius of curvature — the effective radius of curvature near the edge of the mirrors is smaller than in the center — and a spherical wavefront of a gaussian beam is transformed due to the reflection to a more complicated one:

$$\frac{1}{R_2(r)} = \frac{1}{R_1} - \frac{1}{f(r)}.$$

We tentatively attribute the observed effect to these distortions of the wavefront, however, in order to give more quantitative answer, the scalar diffraction theory should be used and/or experiments using torroidal mirrors instead of ellipsoidal should be performed.

Conclusions

A systematic experimental study of the spatio-temporal transformations of ultrashort terahertz pulses during the propagation by various optical paths including a FIR lens and ellipsoidal mirrors has been performed and a model describing the problem is proposed. The experimental results are in a very good quantitative agreement with the predictions of the model. In particular, the model emphasizes the role of the phase change during the propagation and shows that the aperture of the optical elements acts as an effective spectral filter: linear filtering occurs at low frequencies and $1/\nu$ filtering occurs at high frequencies. These results allow better understanding of the shape of THz pulses detected with different techniques and can have an

important asset for the study of various emitters' characteristics and for the THz time-domain spectroscopic applications.

VI.3. Absorption of THz radiation in the air

As have been already mentioned (see the Introduction), the TDTS can be effectively applied to the sensing of gases characterized by significant absorption in THz frequency region[7,8]. In the spectra of the pulses measured with our spectrometers, one can clearly see the sharp absorption of the THz radiation by the water vapor that is always present in the laboratory air (Fig. VI.3.1). The absorption is caused by H_2O molecule rotation transitions which are defined very precisely[8,95] and can be used for the calibration of THz spectrometers. In Table VI.3.1, measured frequencies and wave numbers of the absorption lines compared to the data from Ref. 95 are presented. It is seen that within the frequency resolution of our spectrometer (20 GHz or 0.67 cm^{-1} for a 50 ps scan) the agreement is fairly good.
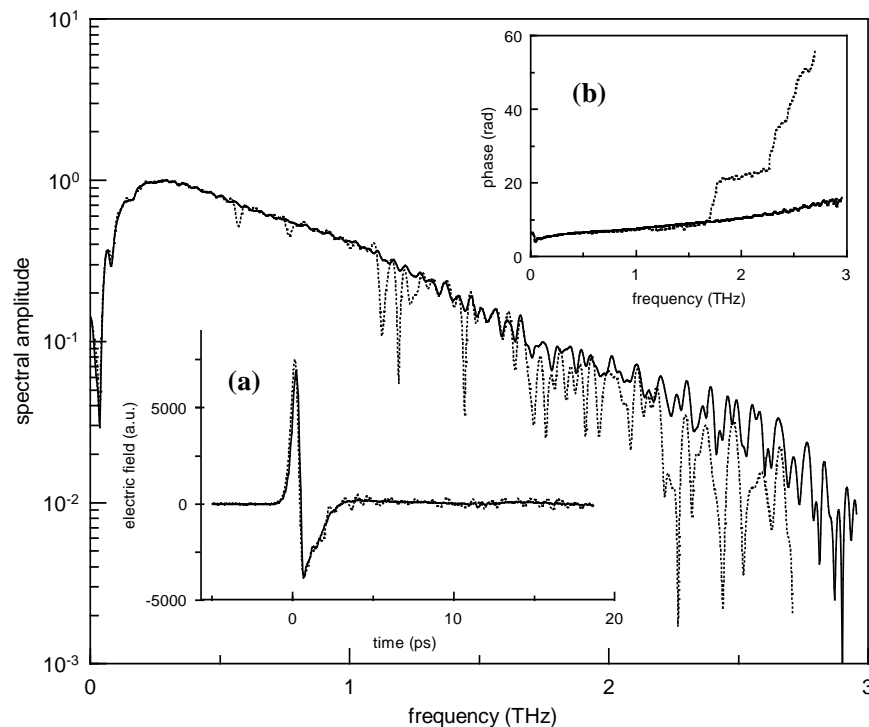
Fig. VI.3.1. The influence of the water vapor absorption on the waveforms and spectra of THz pulses: time profile (a) and its complex spectrum measured with the spectrometer purged with dry nitrogen flow (solid lines) and without purging (dotted lines).

But for THz spectroscopic applications the water vapor absorption is an unwanted effect. The abrupt decrease of the amplitude at the frequencies of the strongest absorption can result in large errors in the determination of a sample's characteristics (Section VII.1). To minimize the influence of water vapor, the spectrometer is put into a plexiglas box purged with dry nitrogen.

Table VI.3.1. Water vapor absorption lines in the THz range

Line #	1	2	3		4	5
f [THz] measured	0.57	0.77	1.13		1.19	1.45
f [cm^{-1}] measured	19.06	25.59	37.57		39.64	48.17
f [cm^{-1}] from Ref. 95	18.58	25.09	36.59	38.73	40.36	48.33

Line #	6		7	8	9		10
f [THz] measured	1.64		1.71	1.76	1.91		2.27
f [cm^{-1}] measured	54.60		57.00	58.67	63.7		75.60
f [cm^{-1}] from Ref. 95	53.46	55.69	57.29	59.68	62.24	64.02	75.52

VII. TIME-DOMAIN TRANSMISSION THZ SPECTROSCOPY

VII.1. Processing of time-domain data

VII.1.1. Bulk samples

The inverse electromagnetic problem, i.e. the obtaining of material characteristics of a sample from its complex transmittance, is solved in terms of complex refractive index. That means that the sample is believed homogeneous in the whole area of the THz beam focal spot that is about several millimeter in diameter for the lowest frequencies. The refractive index $n^* = n + ik$ can be then converted to complex dielectric function $\varepsilon^* = \varepsilon' + i\varepsilon''$ or conductivity $\sigma^* = \sigma' - i\sigma''$ using the relations:

$$n^* = \sqrt{\varepsilon^*} \qquad\qquad\qquad (VII.1.1.1)$$

$$\sigma^* = -i\,\omega\,\varepsilon_0\,\varepsilon^* \qquad\qquad\qquad (VII.1.1.2)$$

The transmittance of a homogeneous plane-parallel wafer has the form:

$$T^*(\omega) = \sum_{p=0}^{m} \frac{4n^*(n^*-1)^{2p}}{(n^*-1)^{2p+2}} \left[\exp\left(-i\omega d n^*/c\right)\right]^{2p+1} \exp(i\omega d/c) \qquad (VII.1.1.3)$$

where m is a number of internal reflections (echoes) taken into account (see Fig. II.1 (a)). The longer is the scan in time domain the better is the frequency resolution of the measurements. Thus, to take into account only the main transmitted pulse ($m = 0$) i.e. to stop the scan before the first reflection comes would be the fastest way of doing measurements but worse spectral resolution would be the cost.

When the wafer is optically thin i.e. adjacent echoes cannot be clearly separated, Eq. (VII.1.1.3) turns into a sum of an infinite row expansion ($p = \infty$):

$$T^*(\omega) = \frac{\dfrac{4n^*}{(n^*+1)^2}\exp\!\left(-i(n^*-1)\omega d/c\right)}{1-\left(\dfrac{n^*-1}{n^*+1}\right)^2\exp\!\left(-2in^*\omega d/c\right)}$$

(VII.1.1.4)

It is the case of so-called *infinite pass*.

Then the Eq. (VII.1.1.3) or (VII.1.1.4) is numerically solved through the Newton-Raphson algorithm[96] to extract the complex refractive index $n(\omega)$.

The determination of the refractive index from the complex transmittance is ambiguous since the phase shift is defined with the uncertainty of 2π. In order to follow the right phase branch one should provide to the program code[97] the initial guess for the refractive index:

$$n = \frac{\Delta t_0 c}{d} + 1$$

(VII.1.1.5)

where Δt_0 is the time delay between the maxima of the of the pulse passed through the sample and the reference waveform. The program then tries inherently to hold the same phase branch but when the transmittance changes drastically (e.g. due to a sharp phonon resonance, see Fig. VII.1.2.1a) or gets very low (Fig. VII.1.2.1b) or when the data are simply too noisy, the right branch can be lost at some point and the program will follow the wrong one. If there is a suspect that some features observed in $n(\omega)$ could originate not from such "hops" of the calculation routine but from phonon resonances of unknown oscillator strength, one should choose the correct phase branch through the Kramers-Kronig check* [Ref. 98] or perform an additional measurement on a sample of the same material but with a different thickness[9].

---

* Various phase branches produce different couples of n and k but only the correct couple will satisfy the Kramers-Kronig relations.

In the case of bulk samples the transmission TDTS allows the determination not only of their complex material functions but also their thickness with the precision of few micrometer[99]. The refractive index calculated from VII.1.2.3 or VII.1.2.4 is very sensitive to the thickness of the sample. If one takes a wrong thickness then artificial oscillations will show up in both index of refraction (Fig. VII.1.2.2) and absorption. Thus, by variation of the slab thickness and seeking for the minimum of the amplitude of the oscillations we find the correct value of the thickness.
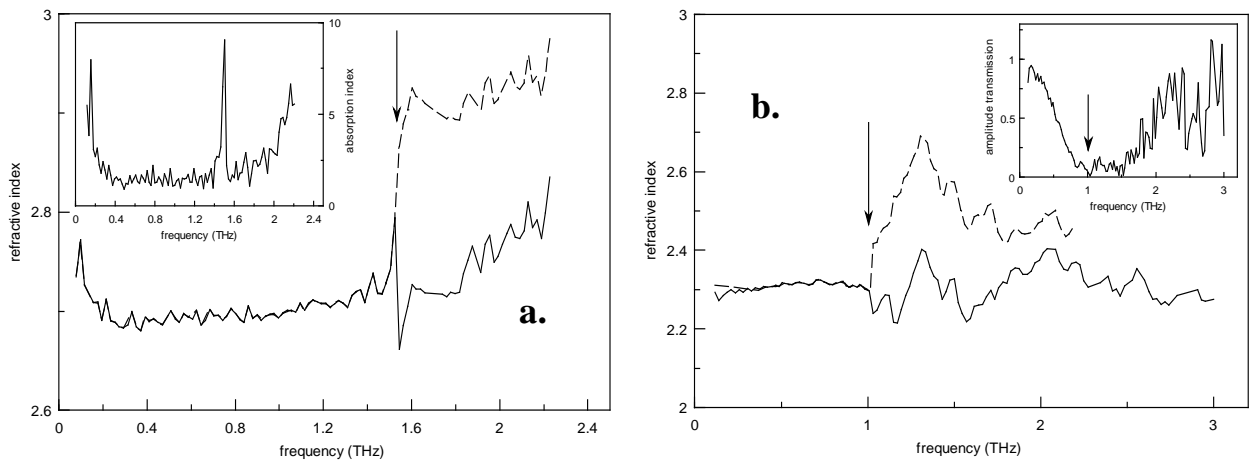
Fig. VII.1.2.1. *Phase ambiguity can result in a "jump" in the refractive index. (a) $Li_2Ge_7O_{15}$: a pronounced phonon resonance at around 1.5 THz (arrowed) leads to the calculation program losing the right phase branch (dashed line); (b) MACOR^{TM} ceramics: high absorption and consequent low transmission (see inset) causes the program to hop to the wrong phase branch (dashed line). Solid lines are the correct spectra of the refractive index.*
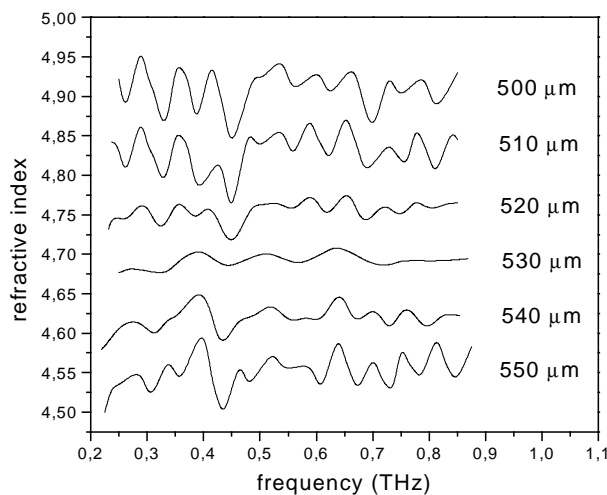
Fig. VII.1.2.2. *Refractive index of a $LaAlO_3$ for different thicknesses of the wafer.*
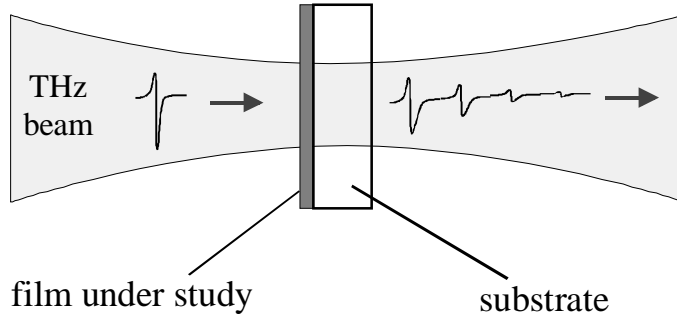
VII.1.2. Thin films

If the sample is a thin film on a substrate (Fig. VII.1.1.4), the refractive index of the substrate has to be measured separately before the measurements of the whole sample transmittance is performed.

If the pulse passed through the substrate is taken as a reference, the full relative complex transmittance of the structure with film is expressed by the following equation

$$
T^*(\omega) = 2n_f(n_s+1)^2 e^{\frac{-i\omega n_f d_f}{c}} \left(1 - \left(\frac{n_s-1}{n_s+1}\right)^2 e^{\frac{-2i\omega n_s d_s}{c}}\right) \bullet [(n_f+n_s)(n_f+1)(n_s+1)
$$

$$
-(n_f+n_s)(n_f-1)(n_f-1)e^{\frac{-2i\omega(n_f d_f+n_s d_s)}{c}} -(n_f-n_s)(n_f-1)(n_s+1)e^{\frac{-2i\omega n_f d_f}{c}} \qquad \text{(VII.1.3.1)}
$$

$$
-(n_s-n_f)(n_s-1)(n_f+1)e^{\frac{-2i\omega n_s d_s}{c}}]^{-1}
$$

where n_f, n_s, d_f, and d_s are the refractive indices and thickness of the thin film and the substrate, respectively. The expression (VII.1.3.1) implies the infinite pass for both the film and the substrate. If the substrate is so thick that THz echoes in it can be cut off through the appropriate time-windowing of the waveform, all the terms containing $e^{-\frac{2i\omega n_s d_s}{c}}$ can be cancelled. Just like in the case of bulk samples, it makes measurements faster and calculation simpler but it lowers the frequency resolution.

In Fig. VII.1.3.1, an example of the application of the described approach to the study of a superconducting thin film is shown.

Fig. VII.1.3.1. Measurement of the transmittance of a thin film sample.

Thin film approximation

If the film is optically thin at THz frequencies so that a THz pulse having passed through it acquires a phase shift much smaller than the typical wavelength i.e.

$$n_f(\omega/c)\, d_f << 1, \qquad \text{(VII.1.3.2)}$$

then the *thin-film approximation*[100] can be used.

Moreover, the material of the film is supposed be optically much denser than that of the substrate:

$$n_f >> n_s > 1 \qquad \text{(VII.1.3.3)}$$

In this case (VII.1.3.1) is reduced to a simple expression:

$$T^*(\omega) = |T(\omega)| e^{i\varphi(\omega)} = \frac{1+n_s}{1+n_s + Z_0 \sigma^*(\omega) d_f} \qquad \text{(VII.1.3.4)}$$

where $Z_0 = 376.7\ \Omega$ is the impedance of free space. The complex conductivity $\sigma^*(\omega)$ is then obtained analytically from (VII.1.3.4):

$$\sigma^*(\omega) = \frac{1+n_s}{Z_0 d}\left(\frac{\cos\varphi(\omega)}{|T(\omega)|} - 1 - i\frac{\sin\varphi(\omega)}{|T(\omega)|}\right) \qquad \text{(VII.1.3.5)}$$

This approach has been widely accepted for the THz study of

superconductor[101, 11] thin films. In this case, however, the use of the thin-film approximation appears to be not particularly correct since so highly conductive materials as HTS can have the refractive index of hundreds so that the condition (VII.1.3.2) fails even for thin (100-200 nm) films at terahertz frequencies. It was the reason for us to discard the thin film approximation in favor of the direct numerical solution of the transmission equation (VII.1.3.1) to obtain the frequency dependent complex refractive index of the film n_f. This approach extends time-domain THz spectroscopy of superconducting thin films to higher frequencies and thicker films (Fig. VII.1.3.3). The refractive index can be then recalculated into the complex dielectric function ε^* or the complex conductivity σ^* through the relations:

$$\varepsilon^* = \varepsilon' + i\,\varepsilon'' = n^{*2} \tag{VII.1.3.6}$$

$$\sigma^* = \sigma' - i\sigma'' = -i\omega\varepsilon_0\varepsilon^*. \tag{VII.1.3.7}$$

Finally, the surface resistance of the film is calculated as:

$$R_S(\omega,T) = \sqrt{\frac{\mu_0\omega}{2}\frac{\left|\sigma^*(\omega,T)\right| - \sigma''(\omega,T)}{\left|\sigma^*(\omega,T)\right|^2}} \tag{VII.1.3.8}$$

Actually, in the case of the films whose thickness does not exceed 150-200 nm, the transmission time-domain THz spectroscopy can be effectively applied only when the material of the film interacts very strongly with THz radiation i.e. is characterized by high indices of refraction and absorption like metals or superconductors. For other materials, the phase shift acquired by a THz pulse during the propagation through the film can be as small as few tens of femtoseconds which is below the temporal resolution of TD-THz spectrometers and the film's material functions simply cannot be extracted from time-domain data (Fig. VII.1.3.4). For such cases the time-domain reflection spectroscopy should be employed (Section V.3, see also Section IX.1.2).
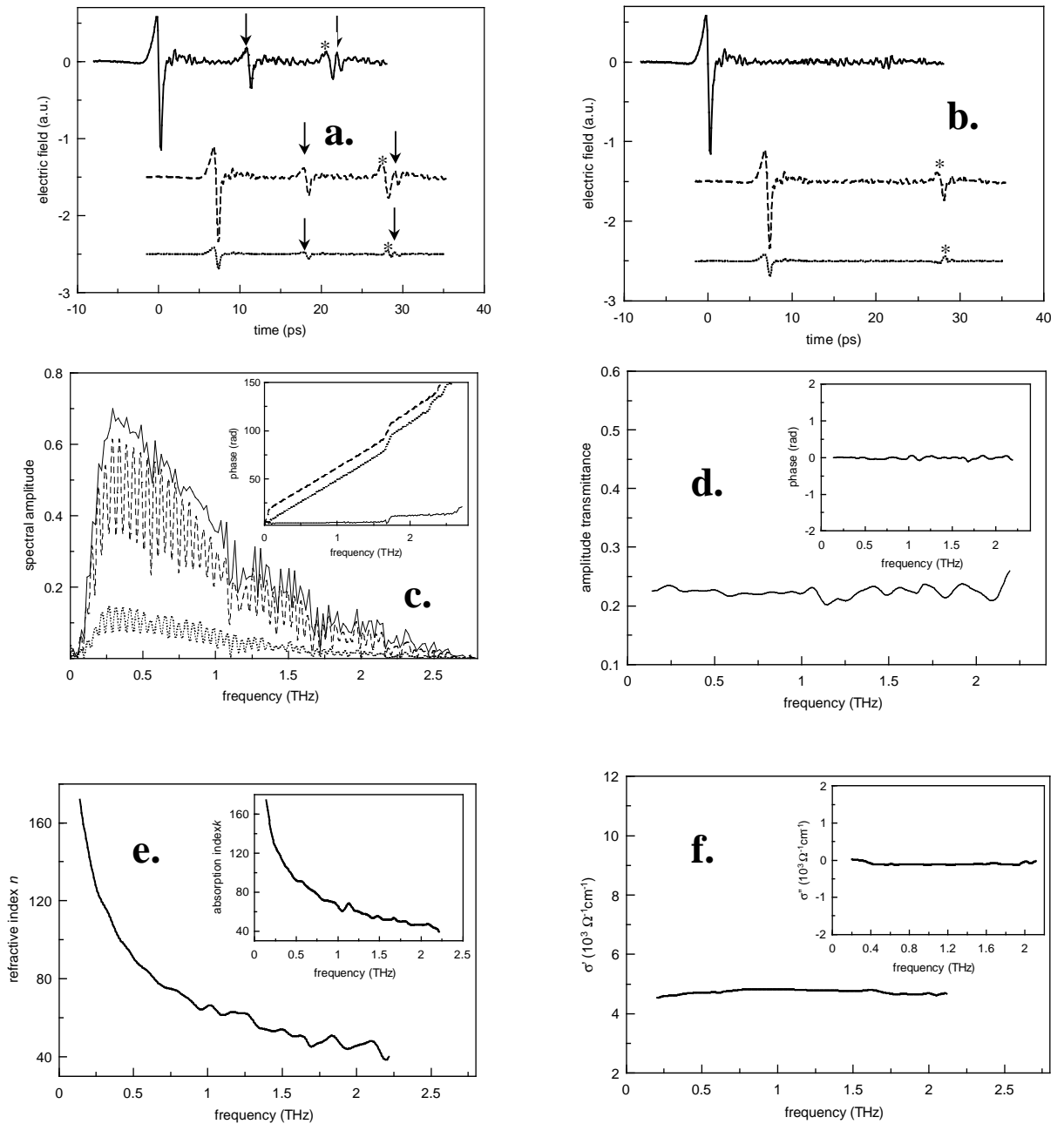
Fig. VII.1.3.2. *An example of the application of the TDTS to the study of thin films (80-nm YBa₂Cu₃O₆.₉₅ film on a 1 mm MgO substrate, T = 300 K): (a) THz waveforms as measured: solid line: freely propagating pulse, dashed line: pulse transmitted through bare substrate, dotted line: pulse transmitted through sample (film on substrate). Multiple reflection within the emitter wafer and within the substrate are marked with arrows and asterisks, respectively; (b) the same waveforms after the subtraction of the multiple reflections in the emitter; (c) corresponding Fourier transforms; (d) complex transmittance of the sample; (e) complex refractive index of the film material calculated through the numerical solution of Eq. (VII.1.3.1) and (f) dynamic conductivity.*
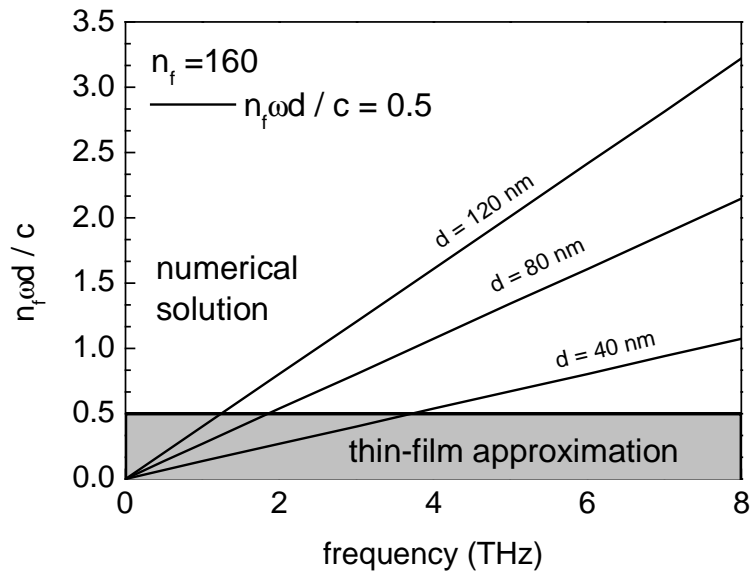
Fig. VII.1.3.3. *Applicability range of the thin-film approximation and the numerical solution of the transmission equation.*
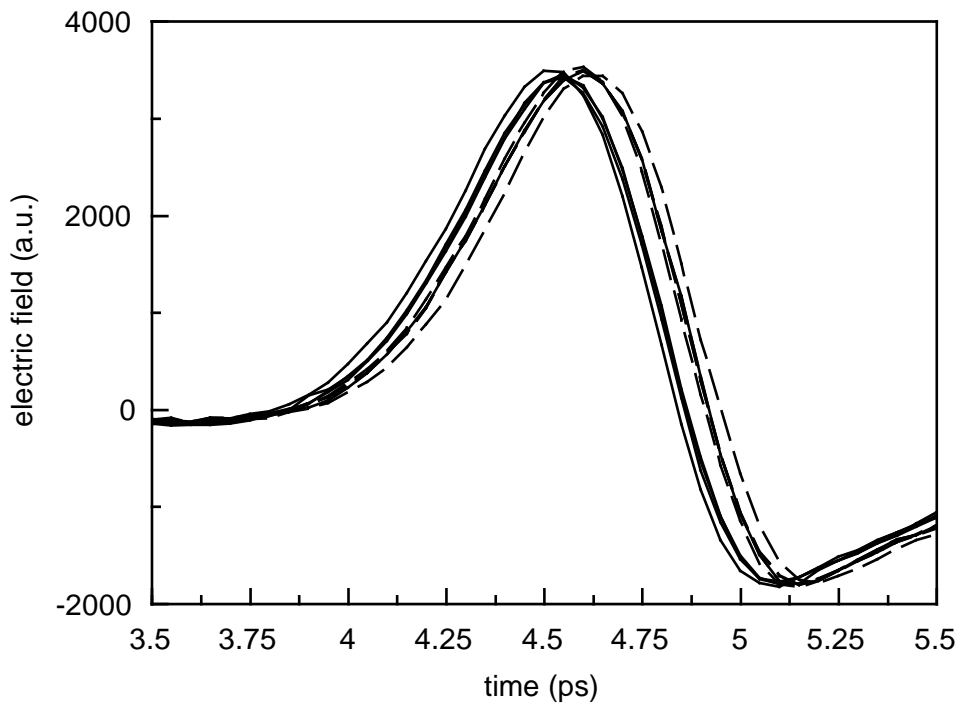
Fig. VII.1.3.4. *THz transmission of thin dielectric film. Solid curves: 5 time profiles of a pulse passed through a 1-mm thick MgO substrate measured in a row; dashed curves: 5 waveforms of a pulse transmitted through a 500 nm thick $YBa_2Cu_3O_6$ film on a 1 mm MgO substrate, T = 29 K. It is clearly seen that the phase shift due to the propagation through the film is comparable with the measurements uncertainty.*

97

VII.1.3. Subtraction of multiple reflections

In every time-domain THz spectrometer, the main THz pulse is always accompanied by echoes (Fig. VII.1.4.1) originating from multiple internal reflections of optical or THz pulses in various elements of the spectrometer like beam splitters, emitter wafer, electro-optic crystal, detector antenna substrate etc. Such "pollution" of the THz waveform can and should be subtracted prior to further treatment of time-domain data.
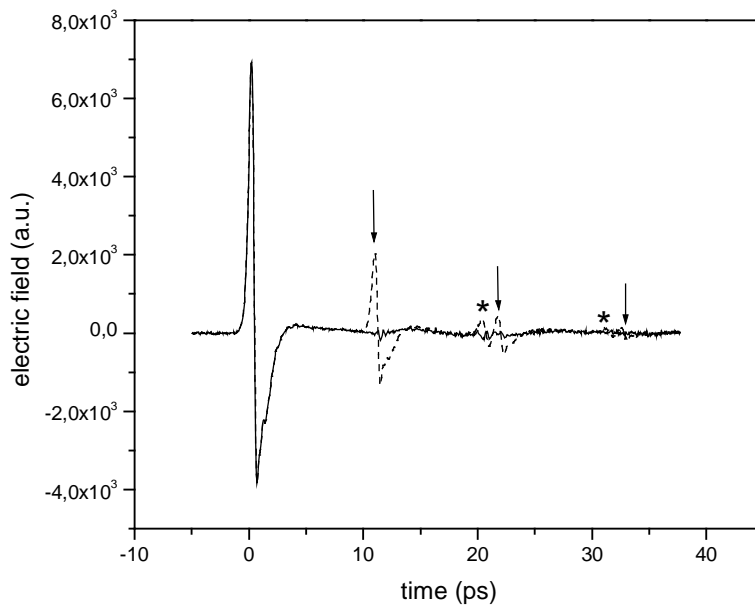
Fig. VII.1.4.1. The main THz pulse (solid line) and its echoes (dashed line). The multiple reflections inside the emitter wafer and the electro-optic crystal are marked with arrows and asterisks, respectively.

The echoes caused by multiple reflections in the pump branch (i.e. the reflections of pump optical pulses or THz pulses themself) of the spectrometer arrive *after* the main pulse. They can be precisely subtracted provided that the reflecting element is a plane-parallel plate with known optical properties and the electromagnetic radiation (THz or optical) have normal incidence on the plate. If all the above conditions are satisfied then the THz waveform appears after the subtraction in the form:

$$E_{sub}(t) = E_i(t) - a\, E_i(t-\Delta t), \qquad\qquad\qquad (VII.1.4.1)$$

where $E_i(t)$ is the measured THz waveform, a is the amplitude ratio of two adjacent reflections and Δt is the time delay between them. If the element's material does not strongly absorb then a and Δt are given by:

98

$$a = \left(\frac{n-1}{n+1} \right)^2 ,$$
$$\Delta t = \frac{d(n-1)}{c}$$

(VII.1.4.2)

where d is the thickness of the plate, n is index of refraction of its material and c is the velocity of light.

There can also be echoes coming from multiple reflections in the *probe* branch of a spectrometer. They come *before* the main THz pulse and to subtract them, rather complicated iterative procedure is required. But they are usually quite weak and therefore one can employ the same linear procedure as in the case of the reflections in the pump branch but, of course, with negative *Δt*.

VII.2. Dynamic conductivity of high-T$_c$ thin films

VII.2.1. Motivation

Symbolically, the appearance of time-domain THz spectroscopic methods has coincided with the discovery of high-temperature superconductivity[102]. Since that, the superconductivity in cuprates has become an unprecedentedly fast growing area of materials research. There have been enormous improvements in preparation and physical characterization of high-temperature superconductors[103] (HTS). These studies are stimulated by needs of electronic industry that sees HTS as extremely perspective materials to be used in low-loss transmission lines, ultra-large-field magnets, powerful electromotors, and even levitating trains[104]. In the most of high-tech applications of HTS like, for example, tunneling-based computer elements or radio-frequency filters (e.g., for cellular phones), the HTS are usually employed in the form of thin (up to few hundred nanometer) films[103,105].

As has been mentioned in the introduction to this thesis, TDTS covers the frequencies, which are hardly accessible for traditional IR and MW methods. On the other hand, the scattering rates in cuprate HTS fall into THz range that makes it especially attractive for the study of their superconductivity mechanism. Moreover, TDTS provides a direct access to the complex material functions while MW techniques measure only a sample's surface resistance from which complex conductivity can be obtained only after making some assumption about the microscopic properties of the sample.

This work presents a study of THz complex conductivity of thin films of two cuprate HTS: $YBa_2Cu_3O_{7-x}$ (YBCO) and $Tl_2Ba_2CaCu_2O_8$ (Tl-2212) by means of the transmission TDTS. The former is the HTS material studied most intensively by all means. Thanks to its technological flexibility, it also finds more industrial applications than any other cuprate superconductor. For us, YBCO has served primarily as a model material for tuning our measurement equipment and data processing procedures to the superconductor research.

Although the growth technology of Tl-Ba-Ca-Cu-O (TBCCO) systems is less advanced than that of YBCO and the production and handling of Tl-compounds requires higher safety precautions, Tl-2212 nevertheless possesses some properties which make it a very promising material for such electronic applications as e.g. channel filters for satellite-based communications systems, low-phase-noise oscillators for radars or active superconducting devices e.g. SQUIDs[106]. TBCCO is namely characterized by higher transition temperature (ranging from 98 K to 110 K), lower $1/f$ noise[107], and smaller concentration of intrinsic weak links[108]. At MW frequencies, Tl films provide at 40-70 K the surface resistance values 50 % lower than YBCO [Ref. 103]. The Tl-2212 system was to date not systematically investigated in the THz range and here we present the first study of its complex material constants by the means of TDTS.

VII.2.2. Experimental data treatment

In order to extract the complex conductivity (or dielectric function) of an HTS thin film's material, the procedure described in Subsection VII.1.3 is employed. Due to very high absorption of HTS materials at THz frequencies, the condition VII.1.3.2 can be hardly satisfied for the films with thickness of several tens of nm and higher. Thus, we rejected the thin-film approximation in favor of a numerical solution of the transmission equation VII.1.3.1.

Two-fluid- and Drude models

Although much has been learned about the properties of cuprate HTS since their discovery 15 years ago, there is still no generally accepted theory that would account for all the phenomena observed in these materials in normal and superconducting state. In most cases, however, THz data can be satisfactorily analyzed in the framework of phenomenological two-fluid model. It considers the charge carriers in a superconductor being of two kinds: normal carriers whose motion is described by the Drude model and superconducting carriers behaving according to the London equation. The total conductivity is then given as a sum of the normal and superconducting components:

$$\sigma(\omega, T) = \sigma_n(\omega, T) + \sigma_s(\omega, T). \qquad \text{(VII.2.2.1)}$$

The normal part σ_n is approximated by the classical Drude expression:

$$\sigma_n(\omega, T) = \frac{n_n e^2 \tau(T) / m^*}{1 - i\omega\tau(T)}, \qquad \text{(VII.2.2.2)}$$

where n_n is the concentration of the normal charge carriers, m^* is their effective mass, and τ is their scattering time. The London expression for the superconducting fraction of conductivity has the form:

$$\sigma_s(\omega, T) = i\frac{n_s e^2}{m^* \omega} = \frac{i}{\mu_0 \omega \lambda_L^2(T)} \qquad \text{(VII.2.2.3)}$$

with n_s being the concentration of superconducting carriers and λ_L the temperature-dependent London penetration depth. Note, that superconducting carriers contribute only to the imaginary part of the whole conductivity. In other words, an ideal superconductor behaves as a pure inductor.

The real and the imaginary part of the whole complex conductivity is then given by the following expressions:

$$\sigma' = \frac{\varepsilon_0 \omega_p^2 \tau}{1 + (\omega \tau)^2} x_n \qquad \text{(VII.2.2.4a)}$$

$$\sigma'' = \frac{\varepsilon_0 (\omega_p \tau)^2 \omega}{1 + (\omega \tau)^2} x_n + \frac{1}{\mu_0 \lambda_L^2(0) \omega} x_s , \qquad \text{(VII.2.2.4b)}$$

where x_n and x_s are the relative normal and superconducting carriers fractions, respectively, so that $x_n + x_s = 1$. ω_p is the plasma frequency: $\omega_p^2 = e^2 N/m^* \varepsilon_0$ (N is the total concentration of carriers, so that $n_n + n_s = N$ and $n_n = x_n N$).

In our analysis, we assume that so-called *clean limit* is valid. It means that the normal conducting fraction vanishes and all carriers turn superconducting at zero temperature. In this case,

$$x_s(T) = \frac{\lambda_L^2(0)}{\lambda_L^2(T)} \text{ and } x_n(T) = 1 - \frac{\lambda_L^2(0)}{\lambda_L^2(T)}, \qquad \text{(VII.2.2.5)}$$

and the expression for the plasma frequency is

$$\omega_p = \frac{c}{\lambda_L(0)} \qquad \text{(VII.2.2.6)}$$

There can be two ways of the fitting of experimentally measured complex conductivity with Eqs. VII.2.2.4a and b. One can either use these full expressions[109,110] or rely on their low frequency approximations. In both cases, $\lambda_L(0)$ (and ω_p) is obtained by the extrapolation of σ" to $T = 0$.

The full Drude fit implies fitting first the real conductivity σ' to obtain τ and then, having the Drude contribution (the first term in Eq. VII.2.2.4b) fixed, the imaginary part σ" to get λ_L. However, it is often quite problematic, especially at lower frequencies, to employ Eq. VII.2.2.4a as a fit function with two parameters τ and x_n. In such cases an assumption about the character of the $x_n(T)$ dependence is made to set limits to the variation x_n. By the analysis of the data on YBCO we have accepted the phenomenological expression

$$x_n(T) = \left(\frac{T}{T_c}\right)^2 \qquad\qquad \text{(VII.2.2.7)}$$

that has proven to provide satisfactory fits at microwave[109] and terahertz[11] frequencies.

An alternative, called *zero-frequency fit* or simply *zero-fit*, uses the low-frequency limit ($\omega\tau \ll 1$) of Eq. VII.2.2.4a and it ignores the contribution of normal carriers to σ" at temperatures below T_c.

$$\sigma' = \varepsilon_0 \omega_p^2 \tau x_n \qquad\qquad \text{(VII.2.2.8a)}$$

$$\sigma'' = \frac{1}{\mu_0 \lambda_L^2 \omega} \qquad\qquad \text{(VII.2.2.8b)}$$

The penetration depth is then extracted directly from the measured imaginary conductivity:

$$\lambda_L(T) = \sqrt{\frac{1}{\mu_0 \omega \sigma''(T)}} \qquad\qquad \text{(VII.2.2.9)}$$

and the quasiparticle scattering rate comes as

$$\frac{1}{\tau(T)} = \frac{\varepsilon_0 \omega_p^2}{\sigma'(T)} \left(1 - \frac{\lambda_L^2(0)}{\lambda_L^2(T)}\right).$$

(VII.2.2.10)

Zero-fit was employed by many researchers (see, for example, Ref. 11). It uses simple and unambiguous fits and is free from any *a priori* assumption about scattering mechanisms in the superconductor (i.e. the temperature dependence of x_n). However, ignoring the Drude contribution to σ'' leads to an underestimation of the London penetration depth. Furthermore, dropping of the $\omega\tau$ term causes errors in the determination of τ. In fact, this approach is not a real fit since it implies only some manipulations with the temperature dependences of conductivity instead of fitting its frequency spectra. In its framework σ' (see Eq. VII.2.2.8) is frequency independent provided that we consider the scattering time τ frequency independent. As a consequence, zero-fit unlike the full Drude fit fails to satisfactorily describe the spectra of the real conductivity in HTS at temperatures well below T_c. Due to all these reasons we performed full Drude fits whenever possible. Zero-frequency fits were used mostly for the processing of very noisy data, e.g., those measured at the lowest temperatures where the transmissivity of HTS films is low.
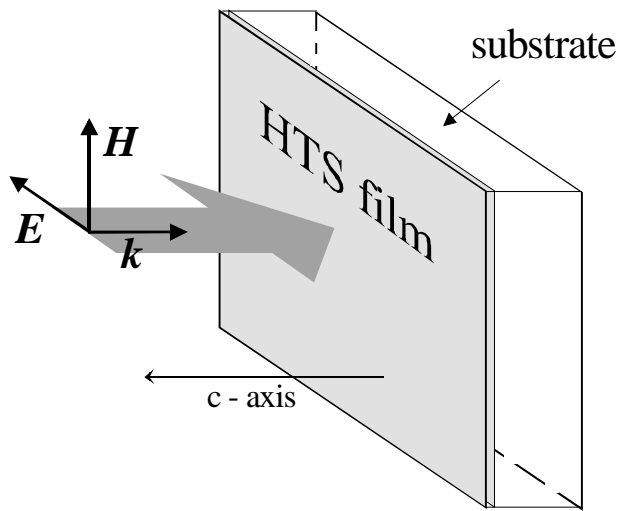
VII.2.3. Thin-film samples

We have investigated several samples of YBCO and TBCCO thin films. Their main parameters are presented in Table VII.2.3.1. All the films were deposited on square 10–mm substrate, as the dimensions of the sample holder required (see Fig. V.1.4.2.).

The YBCO films of thickness from 50 to 100 nm were prepared on 10mm x 10mm x 1mm MgO substrates by the methods of thermal evaporation, dc magnetron sputtering as well as pulsed laser ablation. The Tl-2212 sample was a 80 nm $Tl_2Ba_2CaCu_2O_8$ film on a 10mm x 10mm x 0.5mm $LaAlO_3$ substrate. It has been deposited by sputtering a $BaCa_2Cu_2O_6$ precursor film in argon atmosphere and

subsequently annealed at 877°C for 20 min in a sealed crucible containing optimal Tl-2212 powder.

The superconductor transition temperatures of the films' materials have been determined through the measurements of the temperature-dependent dc-resistivity by four-probe method. The stoichiometry of the YBCO films was checked with the means of Raman spectroscopy[111]. All the HTS films studied are c-axis oriented, i.e. the a-b plane lies parallel to the films surface. THz radiation incidents normally on films so that its polarization oriented in the a-b plane (Fig. VII.2.3.1). As the films are not ordered in the plane, a mixed a-b response have been measured.

*Fig. VII.2.3.1*. *Measurements of THz transmission of HTS thin films.*

Table VII.2.3.1. Parameters of the studied HTS thin-film samples.

sample index	film composition	substrate	film deposition method	film thickness (nm)	T_c (K)	$\lambda_L(T=0)$ (nm)
YBCO1	$YBa_2Cu_3O_{6.95}$	MgO	dc magnetron sputtering	50	86.6	160
YBCO2			laser ablation	80	85.2	179
YBCO3			thermal evaporation	80	81.97	168
YBCO4				100	85.94	186
TBCCO	$Tl_2Ba_2CaCu_2O_8$	$LaAlO_3$	sputtering of $BaCa_2Cu_2O_6$ precursor film + annealing with $Tl_2Ba_2CaCu_2O_8$ powder	80	99.0	245

VII.2.4. YBa$_2$Cu$_3$O$_{6.95}$: experimental results and discussion

THz transmission spectra

Fig. VII.2.4.1. shows the relative (with respect to the transmission of the MgO substrate) amplitude transmittance spectra of a YBa$_2$Cu$_3$O$_{6.95}$ thin film[*] for several different temperatures. At temperatures well above T_c the transmittance is almost frequency independent which is typical for the metallic character of the HTS in the normal state. The superconducting transition causes drastic changes in the transmission spectra. First, there is an abrupt drop in the magnitude of the transmittance at $T < T_c$ where the growth of the Cooper-pair density results in the fast increase of reflectivity. Second, as the temperature further decreases, the transmission develops strong frequency dependence. Namely, the inductive character of a superconductor's conductivity (see Eq. VII.2.2.3) makes it acting as a high-pass filter so that the transmittance increases with frequency.
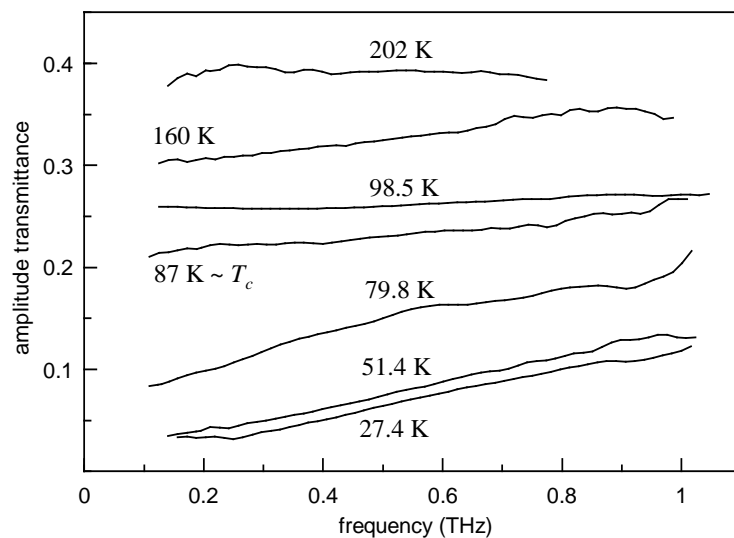
Fig. VII.2.4.1. *Transmission spectra of a YBa$_2$Cu$_3$O$_{6.95}$ thin film at various temperatures.*

---

[*] When another is not specified, the presented data relate to the YBCO1 sample

Complex conductivity spectra and their temperature variation

The frequency spectra of the real and the imaginary part of dynamic conductivity are depicted in Fig. VII.2.4.2. In the normal state, σ' depends weakly on frequency, exhibiting slow Drude-like fall. However, when the sample turns superconducting, the dependence becomes much more pronounced due to the rapid growth of the carrier relaxation time τ (see Eq. VII.2.2.4a). As the temperature falls from 300 K down to T_c, the absolute value of σ' monotonically increases roughly according to a 1/T-law (Fig. VII.2.4.3a). Below T_c, the $\sigma'(T)$ dependence exhibits a distinctive peak at some frequency-dependent temperature ranging from 43.5 K at 200 GHz to 75.3 K at 1 THz.

In the framework of the two-fluid scenario, only normal carriers contribute to the real conductivity σ' which means that it is supposed to go to zero at $T << T_c$ (provided that the clean limit is valid). In our case, the temperature dependence of σ' (Fig. VII.2.4.3a) can be well extrapolated to zero at $T = 0 K$ which is one more indication of a good quality of the sample[*].
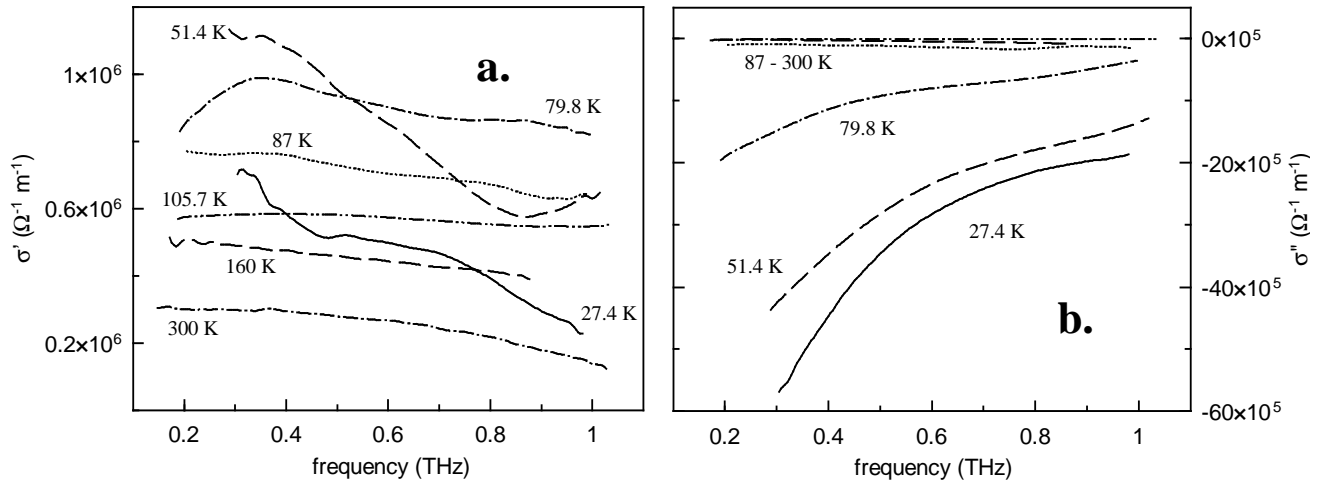
The imaginary conductivity (Fig. VII.2.4.2b) above T_c is almost frequency independent and has absolute values at least 3 orders of magnitude smaller than σ'. Below T_c the σ'' spectra follow an ~1/ω dependence consistent with Eq. VII.2.2.3. Its absolute value rises sharply with falling temperature (see Fig. VII.2.4.3b) and starting from several degrees under T_c the whole conductivity is dominated by σ''. Its sharp rise with the onset of superconductivity can serve as an independent method of the determination of the superconducting transition temperature[**]. At $T \sim 30$ K the

---

[*] Strictly speaking, σ' never goes to zero at $T{\to}0$ in HTS but temperatures below 20 K cannot be reached with our cryostat and the detailed analysis of residual normal conductivity is out of the scope of this work.

[**] However, due to differences in calibration procedures of the setups, T_c obtained by this means at THz frequencies may slightly deviate from the one determined with four-probe measurements of dc resistivity[10]. Thus, from the curves in Fig. VII.2.4.3b comes $T_c^{THz} = 88.7$ K while $T_c^{dc} = 86.6$ K for this sample.

$\sigma''(T)$ begins to saturate at a level of approximately 4 orders of magnitude higher than its room-temperature value.

Fig. VII.2.4.2. *The real (a) and the imaginary part (b) of complex conductivity vs. frequency for a 50-nm thick YBa$_2$Cu$_3$O$_{6.95}$ film.*
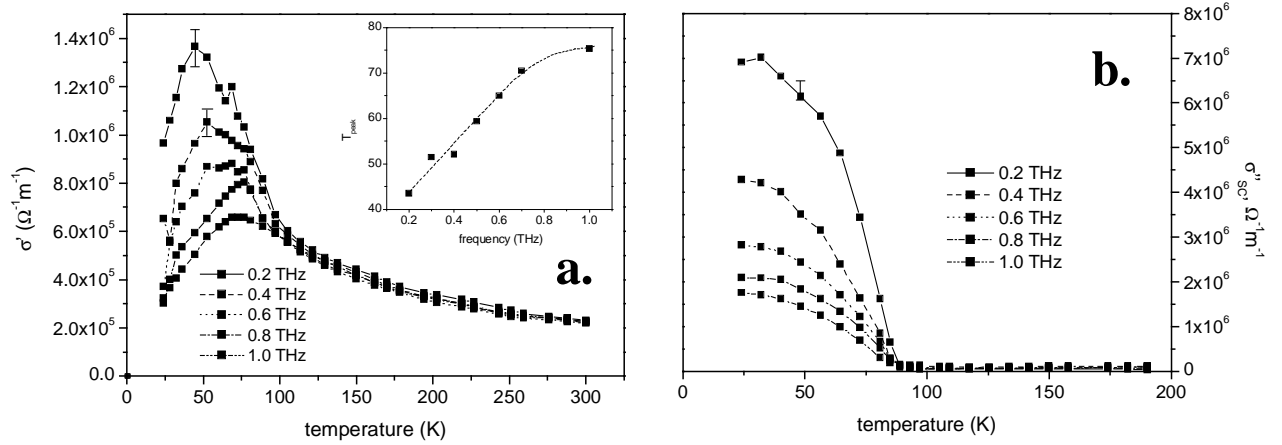
Fig. VII.2.4.3. *Temperature dependences of σ^*. (a): the real part, (b): the superconducting contribution to the imaginary part. The inset in panel (a) shows the temperature of the $\sigma'(T)$ maximum vs. frequency.*

Conductivity peak

The large broad peak in $\sigma'(T)$ is present already in MW range[109,112,113]. There, the main trend for the peak is to become smaller and to be shifted to higher temperatures for increasing frequency. At THz frequencies we observe the same behavior of the peak which is consistent with other results reported recently[114,115,116,117,118]. Some researchers, however, claimed the temperature of the peak to be frequency independent[11, 110].

The detailed nature of the peak is still a topic of intense discussions. It is now generally accepted that it is not a result of BCS-type coherence effects since no coherence features are seen in NMR measurements on YBCO[119]. The conductivity peak's existence is attributed to a competition between two temperature dependences: the sharp increase in the quasiparticle scattering time τ and the vanishing of the superconducting fraction x_n with the temperature decrease. As σ' is proportional to $x_n \tau$, the interplay of those effects leads to the formation of a peak below T_c. There have been also some attempts to take into consideration this effect simultaneously with BCS coherence phenomena[116].

Recently, it has been shown that in crystals of higher quality the peak becomes more pronounced, rises higher, and is located at lower temperature. It is consistent with the above interpretation since the high-purity crystals are naturally characterized by lower concentration of scattering centers i.e. by larger τ. It may be also the explanation why the peak temperature appears to be frequency independent in some THz experiments (Ref. 11, 110). Unlike MW measurements, they are performed on HTS thin films whose quality is much lower than that of single crystals. As a consequence, τ is smaller and the peak is broader. Moreover, the peak arises at temperatures well below T_c where σ'' dominates over σ' and thus the last is determined with much higher uncertainty. These two factors make the exact position of the peak (and its change with frequency) harder to determine.

Penetration depth and scattering rate

Fig. VII.2.4.4 shows the London penetration depth for the YBCO samples as a function of temperature at 0.5 THz. The presented in Table VII.2.3.1. values of $\lambda_L(T=0)$ are obtained from the corresponding temperature dependences by extrapolating them to zero temperature. For our best sample, $\lambda_L(0) = 160$ nm, which is close to 145 nm reported for very high quality $YBa_2Cu_3O_{6.95}$ crystals[109]. In fact, penetration depth can serve as a characteristic of the film quality. Thus, laser ablation is one of the fastest growth techniques but gives films with the concentration of defects much higher than dc magnetron sputtering or thermal evaporation. Our measurements confirm this: $\lambda_L(0)$ for the laser ablated YBCO2 sample is 11 nm larger than that of thermally deposited YBCO3. On the other hand, the epitaxial quality of films is usually lower for larger thickness. This is again consistent with our results: of the two samples which have been grown by thermal evaporation, the penetration depth of 80-nm thick YBCO3 is 18 nm lower than in the case of 100-nm YBCO4. It should be noted, however, that the conductivity and, consequently, λ_L for 100 nm film is defined with higher uncertainty because of the lower transmittance of the film.

Another motivation to study the temperature dependence of the penetration depth is that it reflects the underlying microscopic nature of a sample's superconductivity. In Fig. VII.2.4.4b normalized penetration depth $(\lambda_L(0)/\lambda_L(T))^2$ (which equals to x_s in the clean limit) as a function of normalized temperature T/T_c is presented as compared to the predictions of various superconductivity theories. BCS theory implies an exponential activation of normal carrier fraction x_n (Ref. 120):

$$1 - x_n = \left(\frac{\lambda_L(0)}{\lambda_L(T)} \right)^2 = \frac{1}{\left[3.3 \sqrt{\frac{T}{T_c}} \exp\left(-1.76 \frac{T_c}{T} \right) + 1 \right]^2} \qquad \text{(VII.2.4.1)}$$

Theories of "unconventional superconductivity" give a complicated picture of the energy gap having nodes in k space and predict power-law dependence for normalized penetration depth:

$$\left(\frac{\lambda_L(0)}{\lambda_L(T)}\right)^2 = 1 - \left(\frac{T_c}{T}\right)^\alpha$$

As it is seen in Fig. VII.2.4.4a, our data cannot be satisfactorily described neither by the classical Gorter-Casimir two-fluid model[121] that gives $\alpha=4$ nor by the pure d-wave pairing[122] with its $\alpha=1$. Instead, they lay between the BCS and $\alpha=2$ curves. The last describes the d-wave superconductivity with strong impurity scattering[123]. The $\alpha=2$ behavior of the normalized penetration depth has also been observed both at MW[109] and THz (ref. 115) frequencies.
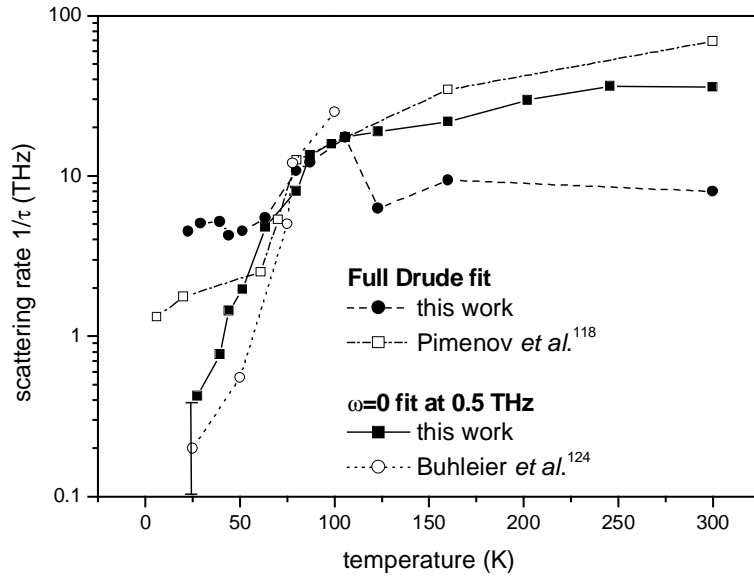
The quasiparticle scattering rate $1/\tau$ (Fig. VII.2.4.5) slowly decreases from the room temperature down to T_c approximately proportional to the temperature. Such behavior has been previously reported for IR and FIR frequencies[117]. Below the transition temperature, the character of the decrease abruptly changes to a rapid exponential fall down to a value around an order of magnitude lower than that at 300 K. Starting from $T \sim 50$ K, the scattering rate remains almost constant as temperature decreases. Similar behavior was registered in YBCO both at MW[109] and THz (Ref. 118) frequencies. It is probably caused by impurity scattering as the plateau in $1/\tau(T)$ in high-quality crystals is significantly lower and is reached at lower temperature than in thin films[109, 112].

The collapse of the scattering rate below T_c appears to be a unique property of cuprate HTS and is responsible for the formation of the peak in the temperature dependence of the real part of conductivity.
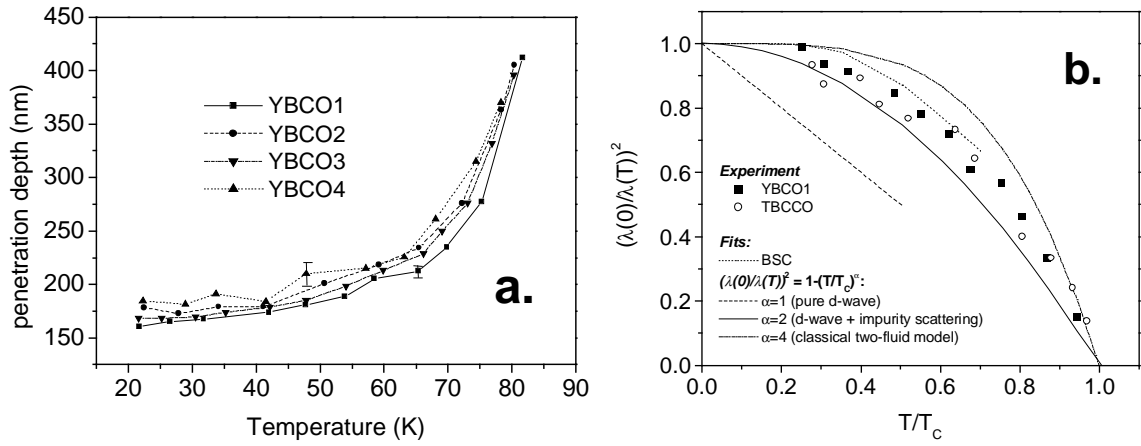
Fig. VII.2.4.4. *Temperature dependence of the London penetration depth at 0.5 THz. (a):*
$\lambda_L(T)$ *in linear scale for four YBCO samples, (b):normalized penetration depth vs.*
normalized temperature, measured data for YBCO1 and TBCCO samples and curves
predicted by some theories.

Temperature dependence of the scattering rate is very sensitive to the procedure applied for its extraction from conductivity spectra. It is clearly seen in Fig. VII.2.4.5 that, compared to zero fit, the full Drude fit provides much higher uncertainty in $1/\tau$ at $T > T_c$. The reason for that is very weak dependence of σ' on frequency at higher temperature. On the other hand, zero fit completely ignores the frequency dependence of real conductivity (see Subsection VII.2.2) which at lower temperature leads to very large errors in $1/\tau$ and to overlooking of the plateau. The results obtained by other groups confirm this idea. Thus, Buhleier *et al.*[124] (see Fig. VII.2.4.5) who used zero fit, did not observe $\sigma'(T)$ to remain almost constant at lower temperatures in contrast to Pimenov *et al.*[118] who performed full Drude fits and clearly observed the plateau.

Fig. VII.2.4.5. *Quasiparticle scattering rate for 80-nm YBa$_2$Cu$_3$O$_{6.95}$ film as a function of temperature obtained from zero- and the full Drude fits to the conductivity spectra.*

VII.2.5. Tl$_2$Ba$_2$CaCu$_2$O$_8$
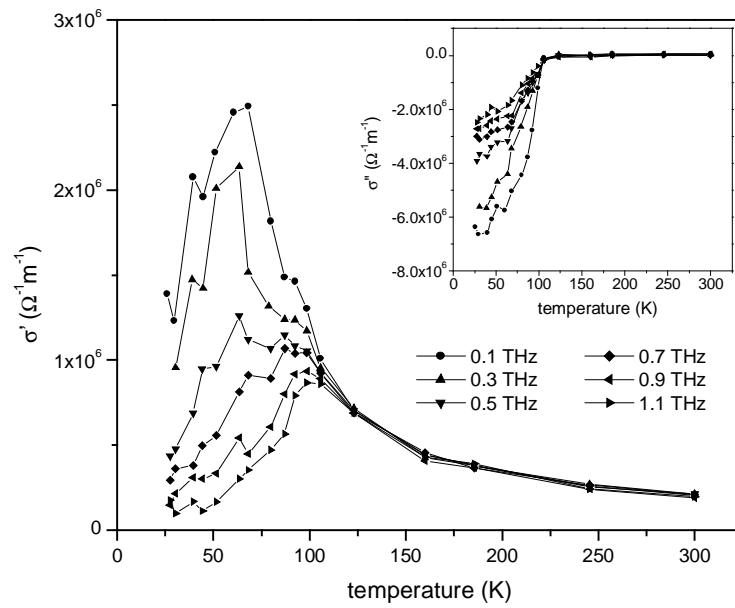
Complex conductivity

The study of the in-plane conductivity in a Tl$_2$Ba$_2$CaCu$_2$O$_8$ (Tl-2212) thin film has revealed that its temperature dependence is markedly different from $\sigma'(T)$ of YBCO. The most important, it has different shape at different frequencies. From the lowest detectable frequency (~100 GHz) and up to ~500 GHz, $\sigma'(T)$ of the Tl-2212 thin film forms a peak at around 60 K. In stark contrast to YBCO, the peak does not shift to higher temperature with increasing frequency and, moreover, it is preceded by a smaller peak at around T_c. The latter is barely seen below 300 GHz but as frequency increases further, the main peak disappears while the smaller one remains.

A similar behavior of the $\sigma'(T)$ dependence has been recently reported for thin film of Bi$_2$Sr$_2$CaCu$_2$O$_8$ (Bi-2212, Ref. 125) that has the crystal layering arrangement identical to Tl-2212 (Ref. 126). The major difference is that our results show that the

113

real conductivity tends to zero at the lowest temperatures for all frequencies in the THz range while in Bi-2212 it was observed only above 200 GHz.

To date, there is no satisfying explanation of the unusual temperature evolution of σ'. It is clear that, unlike the YBCO case, it cannot be described by the competition of the vanishing of normal carrier fraction x_n and the rapid growth of one frequency independent scattering time τ. In order to account for the complicated character of the σ'(T) in Tl-2212, this simple model must be modified by either an introduction of more relaxation times describing different scattering mechanisms or/and making τ frequency dependent: the rapid drop at T_c at frequencies below ~ 500 GHz should change to rather weak temperature dependence at higher frequencies. The idea of two types of carriers has been already raised in connection with non-Drude behavior of the conductivity in some cuprates incl. Tl-2212 (see Ref. 127 and the references 22-24 there).

Fig. VII.2.5.1. *Temperature dependences of real and imaginary (inset) part of complex conductivity of Tl-2212 thin film for six different frequencies. Above ~300 GHz, σ'(T) reveals no low-temperature peak that is typical for YBCO but forms a smaller peak around T_c.*

Penetration depth

Since we could not attribute one frequency independent quasiparticle relaxation time to Tl-2212 we used a zero-fit (Eq. VII.2.2.9) to extract the London penetration depth from the temperature dependence of imaginary conductivity σ''. We observe that λ is proportional to temperature for $T < 55$ K (Fig. VII.2.5.2) which indicates a good crystalline quality of the Tl-2212 film. By extrapolation of the $\lambda_L(T)$ dependence to zero temperature we obtain $\lambda_L(0) = 245$ nm which is in an excellent agreement with the results of the penetration depth measurements by other methods from SQUID magnetometry ($\lambda_L(0) = 221$ nm, Ref. 128) to microwave spectroscopy ($\lambda_L(0) = 260$ nm, Ref. 129). As it is seen in Fig. VII.2.4.4b, the normalized penetration depth vs. normalized temperature in Tl-2212 is close the corresponding dependence in YBCO which indicates the similarity of the superfluid condensation mechanisms in both materials.
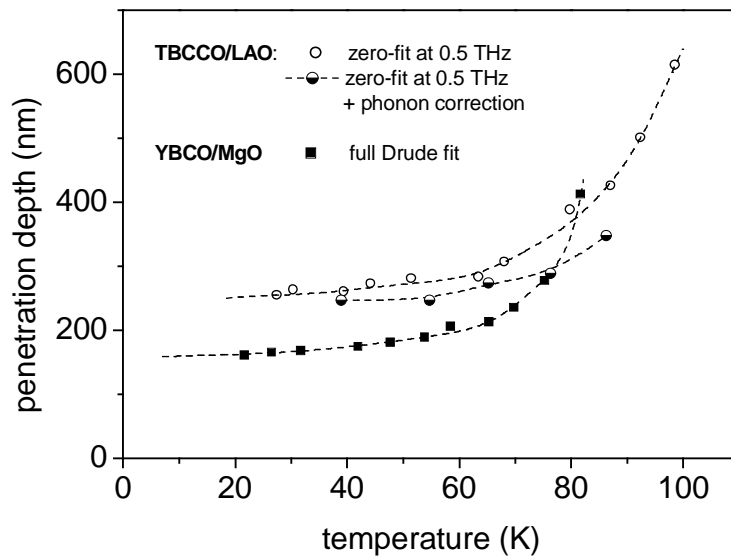

Fig. VII.2.5.2. London penetration depth vs. temperature in TBCCO and YBCO1 samples obtained through zero-fit at 0.5 THz and a full Drude fit to the $\sigma''(T)$ dependence.

Surface resistance

In the area of high-frequency applications of HTS, the surface resistance $R_s(f,T)$ is one of the key material parameters since it determines the dissipation of ac currents. In this subsection, an analysis of the frequency- and temperature dependences of R_s in Tl-2212 thin film is presented.

The surface resistance from 0.2 to 1.0 THz of the Tl-2212 thin film is displayed in Fig. VII.2.5.3 for temperatures above and below T_c and compared to the results of the MW measurements[129, 130,131,132,133].
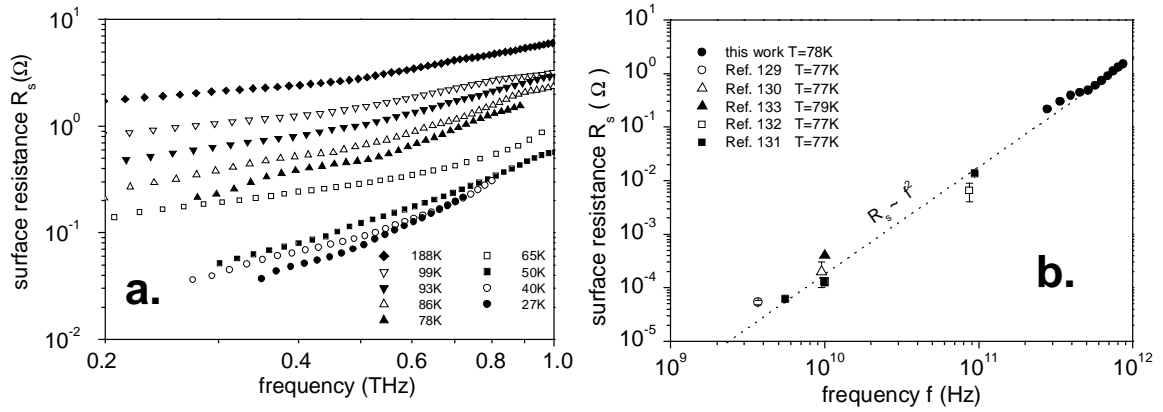
Fig. VII.2.5.3. *Spectra of the surface resistance of a Tl₂Ba₂CaCu₂O₈ thin film at various temperatures (a) and compared previously reported microwave results (b).*

At temperatures above T_c the surface resistance is approximately proportional to the square root of frequency as expected for the normal skin effect. As the Tl-2212 film enters the superconducting state the nonlinear frequency dependence of the surface resistance is strongly enhanced, particularly at higher THz-frequencies.

In microwave studies of Tl-2212 thin films[131, 132] the frequency dependence of R_s at $T < T_c$ has been described as increasing with the square of frequency $\omega = 2\pi f$:

$$R_s \approx \frac{1}{2}\omega^2\mu_0^2\sigma'\lambda_L^2 \tag{VII.2.5.1}$$

116

This expression is valid when σ''>> σ' and σ'= σ'(T), i.e. frequency independent which implies that $2\pi f\tau \ll 1$.

We now compare the THz-measurement of the surface resistance at the temperatures around the boiling point of liquid nitrogen (~ 77 K) to previously reported measurements performed at frequencies between 3.7 and 94.1 GHz (Fig.VII.2.5.3b). In the works cited the measurements have been performed on Tl-2212 thin films deposited by different methods like laser ablation[130] or magnetron sputtering[131-133] on different substrates like $LaAlO_3$ (Ref. 128-131) or MgO (Ref. 127). Nevertheless, the various samples are rather uniform in their properties as characterized by transition temperatures in the range of T_c = 98 to 110 K and London penetration depths between $\lambda_L(0)$ = 200 and 260 nm.

It is evident from Fig.VII.2.5.3b that our TDTS measurements of R_s are in a very good agreement with previous MW data with regard to the overall magnitude of R_s as well as the frequency dependence $R_s \propto f^2$.

Our broadband measurements confirm that the surface resistance increases with the square of the frequency at $T \geq 77K$. We have found, however, that at temperatures below ~77 K the surface resistance spectra cannot be satisfactorily fitted with a f^2 dependence. Thus, we fitted our data with a third-order polynomial:

$$R_S(f,T) = A(T) + B_1(T)f + B_2(T)f^2 + B_3(T)f^3 \qquad \text{(VII.2.5.2)}$$

The temperature dependencies of the polynomial coefficients $A(T)$, $B_1(T)$, $B_2(T)$ and $B_3(T)$ as determined by cubic fits to the experimental data are displayed in Fig. VII.2.5.4. The frequency dependence of R_s is dominated by the linear term B_1 and the cubic term B_3 below T = 60 K. The coefficients B_1 and B_3 are highest for the lowest temperature measured and decrease with rising temperature whereas B_2 grows. From T = 77 K to T_c the frequency dependence of R_s is dominated by the quadratic term B_2.
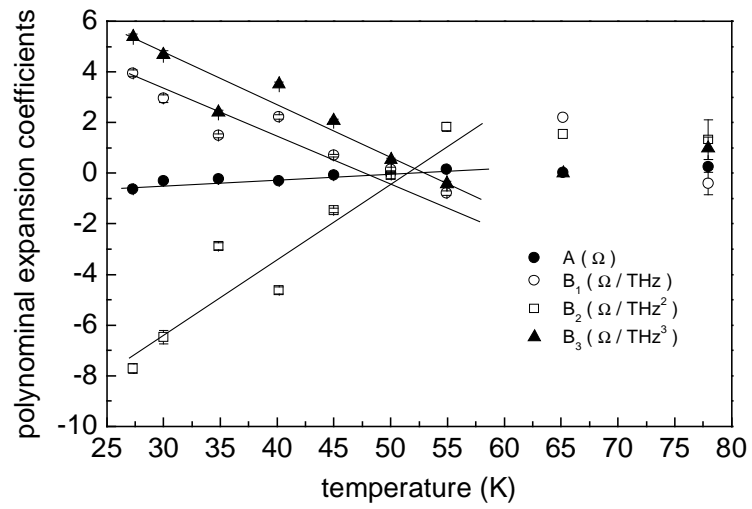
Fig. VII.2.5.4. *Polynomial expansion coefficients A, B_1, B_2 and B_3 as a function of temperature. Solid lines are guides to the eye.*
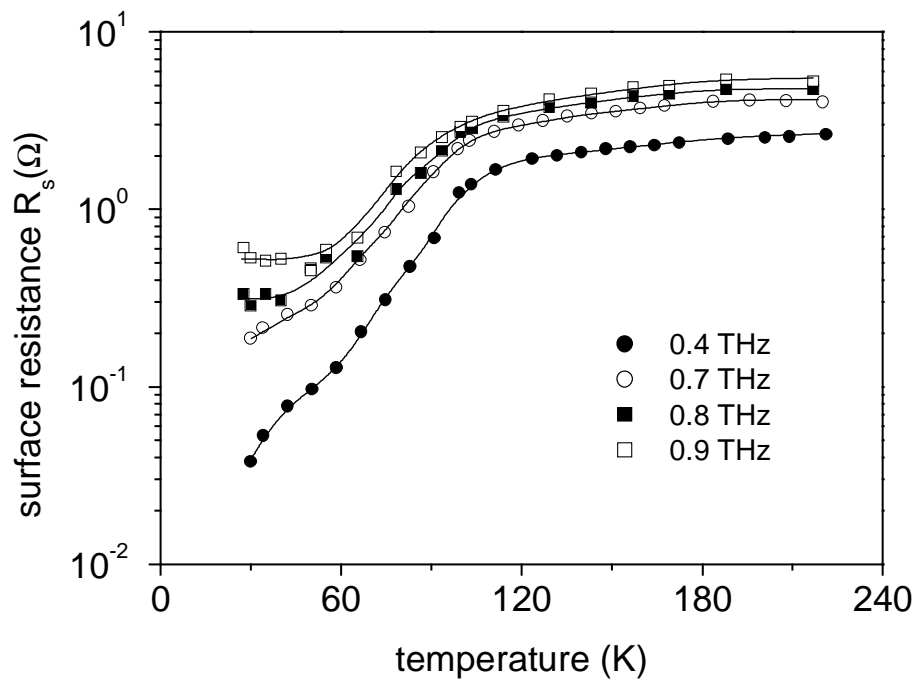
Fig. VII.2.5.5. *Temperature dependence of the surface resistance of a $Tl_2Ba_2CaCu_2O_8$ thin film.*
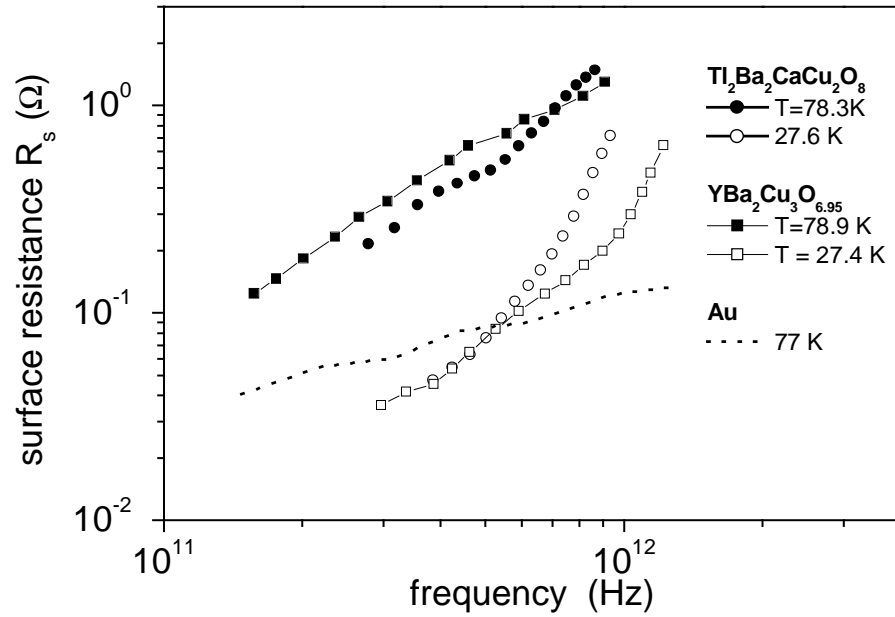
Fig. VII.2.5.6. Performance of Tl₂Ba₂CaCu₂O₈ compared to YBa₂Cu₃O₆.₉₅ and gold. For Tl₂Ba₂CaCu₂O₈ Rₛ at 78.3 K is proportional to the square of the frequency up to 1 THz.

The f^3-dependence of R_s cannot be explained by σ' getting frequency dependent through the $\omega\tau$ term in Eq. VII.2.2.4a because at higher frequencies it would make σ' decrease and subsequently the rise of R_s slow down (as illustrated for YBCO in Fig.VII.2.5.6) or even to turn the surface resistance frequency independent. BSC analysis predicts a similar behavior of R_s or even its decrease at higher frequencies[134] i.e. the trend opposite to that observed. At the moment, there is no satisfactory theoretical description of the appearance of the f^3-term. It is possibly caused by some additional losses, for example, dielectric loss. The analysis of the dielectric function of Tl-2212 in the following Subsection also indicates this possibility.

 The temperature dependence of the surface resistance of the Tl-2212 thin film is shown in Fig.VII.2.5.5. Above the superconducting transition temperature the surface resistance linearly depends on temperature for all frequencies. Below T_c, it monotonically drops two orders of magnitude between 99 K and 27 K first as T^4 for T from 99 K down to 70 K and then directly proportional to temperature for $T < 70$ K at $f = 0.4$ THz. As frequency increases the surface resistance reaches a plateau at low

119

temperatures ($f > 0.8$ THz). This is again the manifestation of the onset of $R_s \propto f^3$. The resulting residual surface resistance is $0.5\ \Omega$ at $f = 0.9$ THz and $T = 30$ K.

From the point of view of MW- or THz electronic applications, it is interesting to compare the investigated Tl-2212 to "HTS #1" YBCO and to such widely used metal as gold. Fig. VII.2.5.6. shows the surface resistance of the Tl-2212 film compared to YBCO1 sample and gold (the data on Au are taken from Ref. 135). At 77 K gold always exhibits a lower surface resistance than Tl-2212 in the THz range. Compared to YBCO, Tl-2212 has lower R_s below ~ 0.6 THz at this temperature and has larger R_s at higher frequencies. At the lowest temperature measured in our experiments ($T \sim$ 27 K) Tl-2212 has approximately the same surface resistance than YBCO but lower than gold for $f < 0.5$ THz and larger R_s than YBCO and gold above 0.5 THz.

Dielectric spectra

TDTS gives a unique possibility to the direct study of a material's complex dielectric function $\varepsilon^* = \varepsilon' + i\,\varepsilon''$. Unlike MW or IR spectroscopy, ε^* comes immediately from the measured THz transmissivity or reflectivity and there is no need to have any *a priori* knowledge about the properties of the material (e.g., ε_∞).

The above-described unusual properties of Tl-2212 at higher THz frequencies clearly manifest themselves in the dielectric function spectra as well. Normally, the real part of the dielectric function (also called dielectric dispersion) in metals and superconductors is negative which corresponds to the strongly inductive behavior of a material. In Tl-2212, however, even at the lowest temperature reachable with our cryostat (~ 27 K) we observe the $\varepsilon'(f)$ curve to cross the zero level (Fig. VII.2.5.7). As the temperature increases and the absolute value of ε' falls, the frequency where ε' turns zero decreases and above T_c the dielectric dispersion is positive in the whole frequency range of our spectrometer (see inset (b) in Fig. VII.2.5.7 and the temperature dependences in Fig. VII.2.5.8). It is quite surprising since the sample is metallic. $\varepsilon' > 0$ is certainly not an artifact of the experimental setup since it is well reproducible while in YBCO we observe only negative dielectric permittivity. Measurements of IR reflectivity (inset (c) in Fig. VII.2.5.7) at room temperature have

produced ε' of the same order of magnitude and the sign as our THz results[*]. Previously, ε' turning positive in Tl-2212 at higher temperature in mid-IR range have been also reported[136].

As a rule, the response of a metal or a superconductor at THz frequencies is dominated by free-carriers contribution, which screens out all other components like lattice oscillations. Tl-2212, however, strikingly differs from other cuprate HTS by the pronounced phonon structure that is clearly seen in its reflectance and conductivity at FIR frequencies[137]. Slightly above our frequency range, at least two infrared active phonon modes at 2.12 THz (TO) and 2.14 THz (LO) are expected[138] and this phonon contribution can be responsible for the real dielectric function to become positive at $T > T_c$. The authors of Ref. 135 argued that the phonon structure that they observed in their FIR reflectivity measurements might arise from the c-axis response due to the non-normal incidence. In our TTDTS experiments, however, samples were always set to the normal incidence. Thus, the "visibility" of the phonon background has to be explained by some intrinsic mechanism that would cause lowering of the carrier concentration and thus of the screening of phonons.
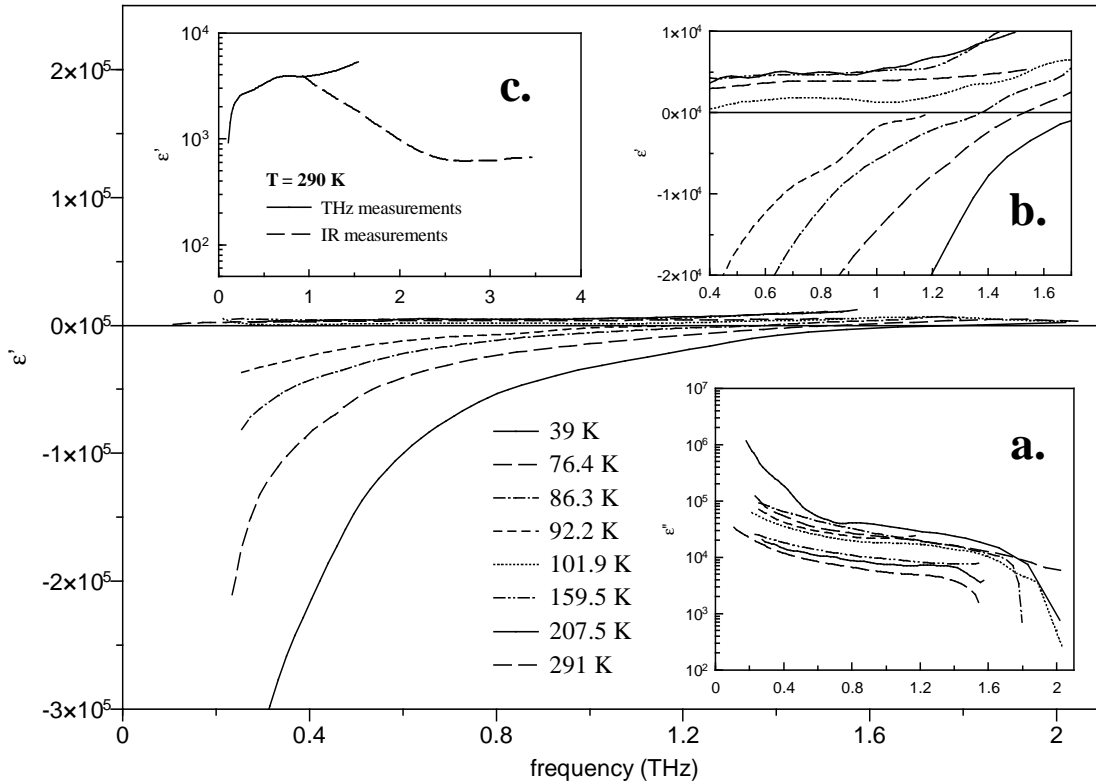
Fig. VII.2.5.7. *Frequency dependence of the real and imaginary (inset (a)) part of the dielectric function of Tl-2212 thin film. Inset (b): a magnified view of the part of the spectrum where ε' changes its sign; inset (c) the ε'(f) dependence and room temperature measured by TDTS and conventional IR reflection spectroscopy. In all insets the horizontal axis is frequency in THz.*
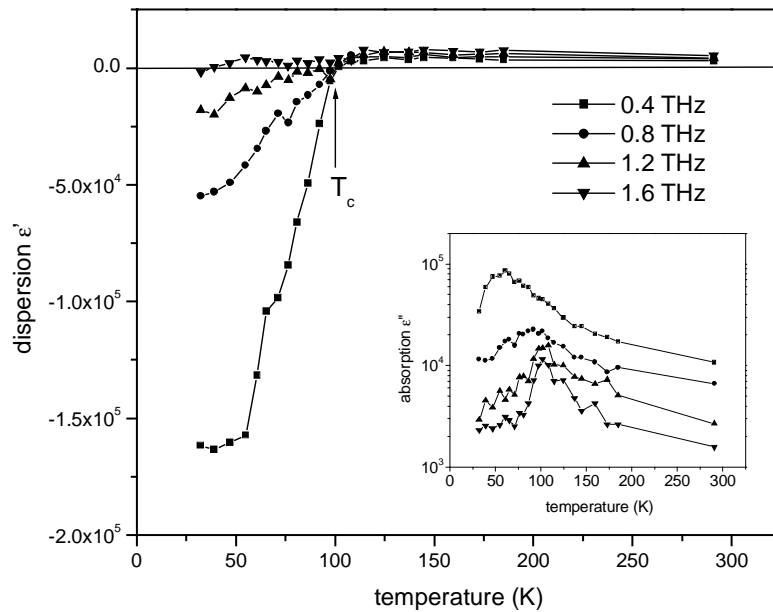
Fig. VII.2.5.8. *Temperature dependence of the real and imaginary (inset) part of the dielectric function of Tl-2212 thin film. Below ~1.6 THz ε'(f) curves cross the zero level around T_c=99 K, at higher frequencies ε' remains positive in the whole temperature range.*

The contribution of a phonon to the complex dielectric permittivity can be described by a damped Lorentz oscillator:

$$\varepsilon_{Lorentz} = \frac{S\omega_0^2}{\omega^2 - \omega_0^2 - i\omega\gamma},$$

(VII.2.5.3)

where S is the oscillator strength, ω_0 is the central frequency, and γ is damping of the oscillator, respectively.

Then the full dielectric function in the two-fluid scenario takes the following form:

$$\begin{cases} \varepsilon' = -\dfrac{\omega_p^2\tau^2}{1+(\omega\tau)^2}x_n - \dfrac{c^2}{\lambda_L^2\omega^2}x_s + \dfrac{S\omega_0^2(\omega^2-\omega_0^2)}{(\omega^2-\omega_0^2)^2+(\omega\gamma)^2} \\ \varepsilon'' = \dfrac{\omega_p^2\tau}{[1+(\omega\tau)^2]\omega}x_n + \dfrac{S\omega_0^2\omega\gamma}{(\omega^2-\omega_0^2)^2+(\omega\gamma)^2} \end{cases}$$

(VII.2.5.4)

At the moment it is hardly possible to fit the measured $\varepsilon^*(\omega) = \varepsilon'(\omega) + i\varepsilon''(\omega)$ with these full expressions because of (i) unknown frequency behavior of quasiparticle scattering time τ (or more then one τ, see above) and (ii) lack of reliable FIR data on Tl-2212 which could provide phonon(s) parameters S, ω_0, and γ. So, in order to take the phonon contribution into account we simply introduced a frequency-linear term into the zero-fit expression for ε' to obtain a corrected value of the London penetration depth at each temperature:

$$\varepsilon' = -\frac{c^2}{\lambda_L^2\omega^2} + const \bullet f$$

(VII.2.5.5)

Such phonon-corrected fit to the dielectric function (or conductivity) produces indeed smaller values of λ_L (Fig. VII.2.5.2), especially at higher temperatures, which to our mind are closer to the right ones.

VII.2.6. Conclusions

The investigation of the complex material functions of high-T_c superconductors YBa$_2$Cu$_3$O$_{6.95}$ (YBCO) and Tl$_2$Ba$_2$CaCu$_2$O$_8$ (Tl-2212) by the means of TTDTS has been carried out. The data on YBCO were analyzed in the framework of the two-fluid model that allowed the extraction of such intrinsic material parameters as quasiparticle scattering rate and the London penetration depth.

Our experiments revealed that in Tl-2212 the temperature dependence of complex conductivity looks significantly different from that in YBCO and thus cannot be described with one frequency independent scattering rate. Another deviation from the classical two-fluid behavior was observed at frequencies above ~ 0.9 THz and may be probably caused by unusually strong influence of phonon modes. Thus, the surface resistance deviates strongly from the microwave f^2-dependence and the real part of the dielectric function at $T > T_c$ turns positive at higher THz frequencies.

From the practical point of view, our results show that that thin films of Tl-2212 can be used in THz electronics with at least the same effectiveness as YBCO and thank to its higher T$_c$ and lower $1/f$ noise it is a very promising material for future applications.

VII.3. Complex transmittance of tungsten wire grids

VII.3.1. Introduction

Free-standing wire grids are widely in use in FIR and THz spectroscopic techniques as polarizers and beam dividers. Thus, at DESY they are employed in a Martin-Puplett interferometer that detects THz pulses produced by relativistic electron bunches in the TESLA test facility. The interferometer is used for electron bunch length measurements and is operated between 0.05-1.6 THz (Ref. 139). In the framework of our collaboration with DESY, we have investigated the complex

transmittance of the grids by the means of TDTS to make possible the calculation of the performance of the entire setup. Our motivation was also the applicability of the existing theories of wire grid transmission to the THz frequency range.

The experimental studies of the transmission of wire grids by Mok *et al.*[140], Beunen *et al.*[141] and Volkov *et al.*[142] appear to be the most comprehensive. The frequency range covered by those measurements extents from 0.6 THz to 13 THz (Ref. 141) and from 1.2 to 9 THz (Ref. 140) for grids with filling factors from 0.15 to 0.33 THz (Ref. 141) and from 50 GHz to 0.2 THz (Ref. 140). The amplitude and the phase of the transmitted THz-radiation in those experiments have been measured by dispersive Fourier spectroscopy.

The basic geometrical parameters of a wire grid are the wire diameter s, the grid period D, and the grid fill factor $f = s/D$. In this study wire grids with fill factors 0.20 and 0.33 in the frequency range 0.1 -1.6 THz have been investigated.
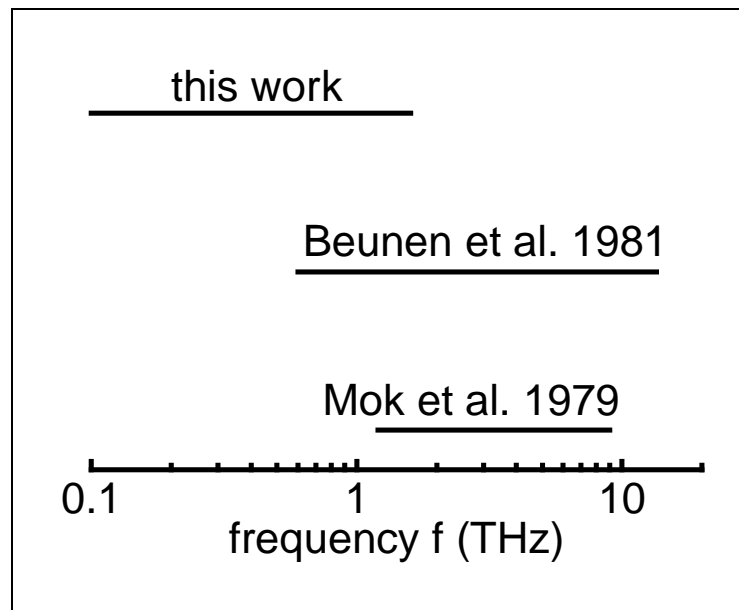
Fig VII.3.2.1. The frequency range covered by our study and some other works on wire grid transmission.

VII.3.2. The grids

The grids (Fig. VII.3.2.2) are constructed of fine cylindrical gold-coated tungsten wires. They are fabricated in the machine shop of the 2. Physikalische Institut of the RWTH Aachen. The dimensions of the two wire grids investigated are listed in Table VII.3.2.1.
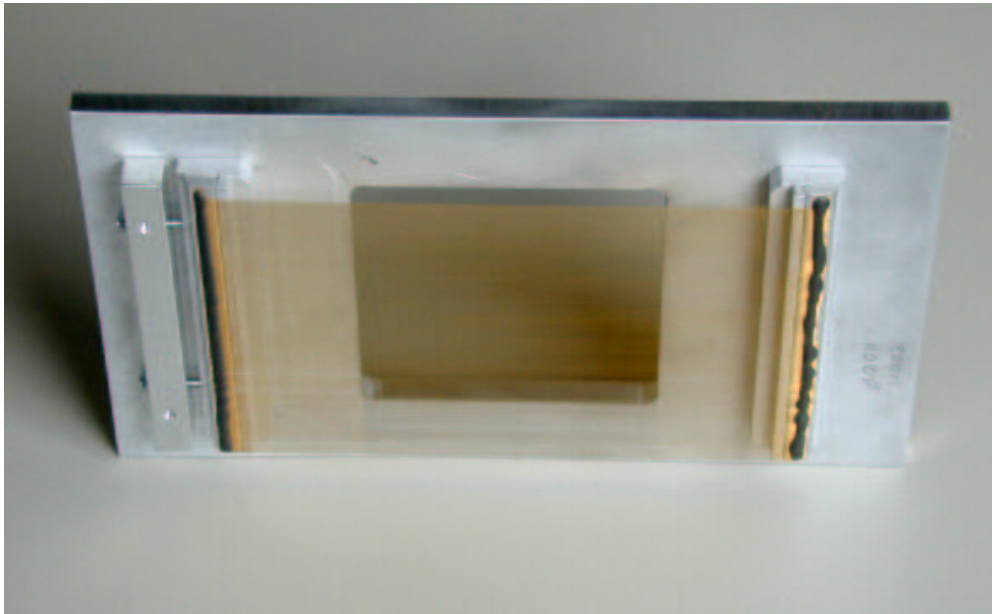
Fig VII.3.2.2. The wire grid

Table VII.3.2.1. Parameters of the wire grids.

grid #	aperture, mm	wire diameter s, μm	grid period D, μm	fill factor $f = s/D$
1	$\varnothing$=90mm	20	100	0.20
2	80mm x 80mm	10	33	0.33

VII.3.3. Experimental results and discussion

The wire grids were placed in the focus of the THz-beam between parabolic mirrors II and III (see Fig V.1.3.1) perpendicular to the propagation direction of the THz beam. The THz-radiation is linearly polarized. Like in the most of our experiments, the THz radiation was polarized horizontally.

The transmission of the wire grids has been measured for the polarization of the THz-electric field **E** parallel to the wires (**E** ∥ S) and **E** perpendicular to the wires (**E** ⊥ S). An example of measured time profiles and the corresponding Fourier spectra are shown in Fig. VII.3.5.1 and the complex transmittances are presented in Fig. VII.3.5.2. In case of **E** ⊥ S the transmission of wire grids is high. The temporal profile of the transmitted THz-pulse is almost identical to the freely propagating pulse.

In case of **E** ∥ S the transmission of the wire grid is lower. In addition, the temporal profile of the transmitted THz-pulse is changed significantly i.e. a grid acts a as a highly dispersive medium in this case.

In Fig. VII.3.6.1 the measured complex transmittance of the grids together with the theoretical curves by Beunen *et al.*[141] and Chambers *et al.*[143] A type of least-squares method developed by Davies[144] (called in the nomenclature of Petit[145] the *modal expansion method*) and then used by Mok *et al.*[140], Beunen *et al.*[141], and Volkov *et al.*[142] provides a good description of experimental results only for grids with very low fill factors. Even for $f = 0.2$, the deviation is significant, especially for **E** ⊥ S and at frequencies higher than 500 GHz. In the frequency range investigated (0.1 – 1.6 THz) the theory describes the grids as being almost perfect polarizers i.e. practically transparent at the **E** ⊥ S and almost opaque at the **E** ∥ S orientation. On the contrary, the exact theory of Chambers *et al.*[146] (often referred to as the *Green's function method*) is found again to give a much better description of the measured data.

The persisting deviations between theory and experiment are caused most probably by the disorder in the grid structure. As have been mentioned in the works cited (see, for example, Ref. 141) the irregularity of the grid structure is stronger for grids with larger fill factors. In our study we observe the same phenomenon. It can be explained by the relative deviation of the spacing between wires increasing with the grid density[140] since the denser is a grid, the greater is the difficulty to produce it evenly spaced[143]. Among other possible defects of the grid structure can be the poor flatness

or bad uniformity of wire diameter. Also, there can be significant ellipticity of the wire cross section.
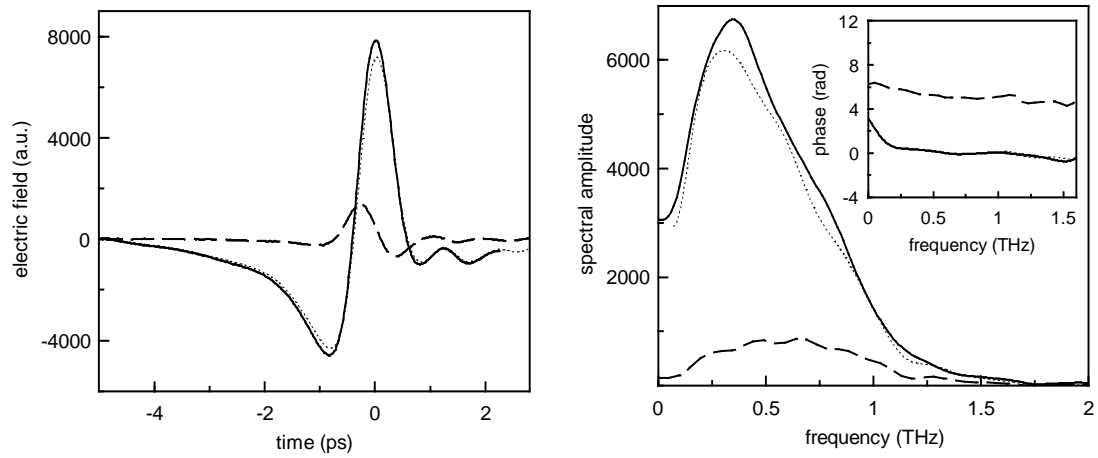
Fig. VII.3.5.1. *Waveforms (left panel) and complex Fourier spectra (right panel) of the THz pulses propagating in free space (solid lines) and passed through the grid #1 with **E** // S (dashed lines) and **E** ⊥ S (dotted lines).*
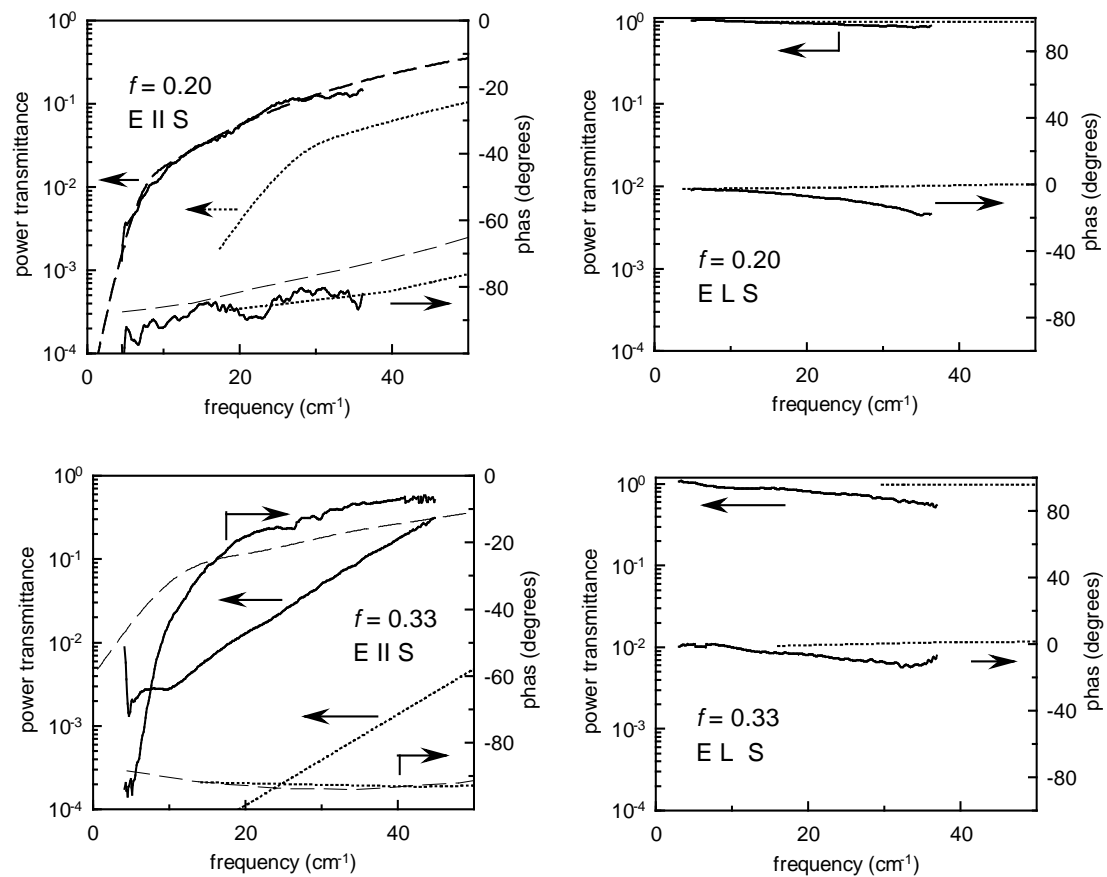
Fig. VII.3.5.2. *Complex transmittance of tungsten wire grids: experimental data (solid lines) and predictions of modal expansion[142] - (dashed lines) and Green's function[146] (dotted lines) methods.*
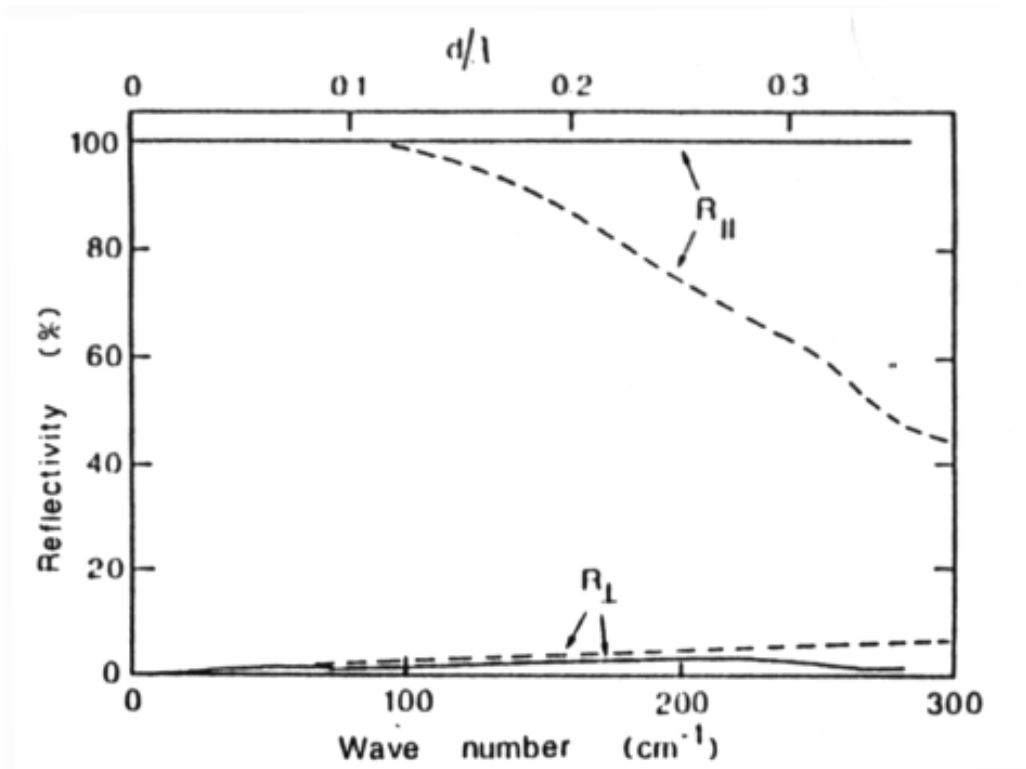
Fig. VII.3.5.2. Comparison of reflectivity spectra fo two grids constructed by using a coil winder with (solid line) and without (dashed line) the precise control of the wire spacing with a step motor. The picture is taken from Ref. 143.

In general, the quality of grids has a decisive impact on their performance. The construction of grids with the help of a modified coil winder where the grid spacing is precisely controlled with a step motor, leads to the significant suppression of random errors in the grid structure. Thus, the relative standard deviation of the wire spacing is reduced down to 0.17 (Ref. 143) against the typical 0.5 for grids created with a conventional coil winder. This leads to a spectacular improvement of the grid performance (see Fig. VII.3.5.3).

Superluminal effects

K. Wynne and coworkers[147,148] attributed the fact that the maximum of the THz pulse transmitted through a metallic patterned structure is getting shifted backwards in time with respect to a freely propagating pulse to the „superluminal effects" i.e. light propagation with velocities higher than c. Such an approach does not seem to be correct since a negative (as well as positive, of course) shift of pulse peak can be a

consequence of several other not so exotic effects e.g. pulse reshaping due to focusing/defocusing (see Chapter VI) or propagation through a dispersive medium. In our data in the case of **E** ∥ S configuration the peak of a pulse passed through a grid gets also shifted "backwards" but the pulse shape itself is very much different from the freely propagating pulse profile. In fact, our data on wire grids look similar to the results of Wynne *et al.* both in time and frequency domain. In Fourier space the phase curve for the pulse transmitted through the structure oriented perpendicular to the incident field polarization goes under the phase curve of the freely propagating pulse. Or, equally, the phase of the corresponding complex transmittance is negative, which was observed in all previously published works on wire grids when **E** ∥ S.

To our mind, the negative phase shift (at least in this particular case) can be explained without any references to superluminal effects but through the basic principles of electrodynamics. When electromagnetic wave strikes a wire the last starts to emit a wave in anti-phase (in order to satisfy the boundary condition i.e. the tangential component of the electric field equals to zero). But due to the wire having non-zero reactance, this secondary wave has a positive time shift with respect to the incident wave and its amplitude is smaller and the shape is changed due to the wire's resistance and the dispersion in its material. Even in its focal point the THz beam cross section is never smaller than at least few millimeter in diameter. This implies that its large part passes the wire in any case. So, the electric field at the detector is actually a superposition of that passed portion and the field of the anti-phase wave. It is valid for any frequency so that a sum-waveform (i.e. a pulse time profile) will always have a peak shifted backwards with respect to the pulse measured without the wire or, equally, the corresponding transmittance will have negative phase. All that is in a good agreement with the results reported previously (see, for example, Ref. 141).
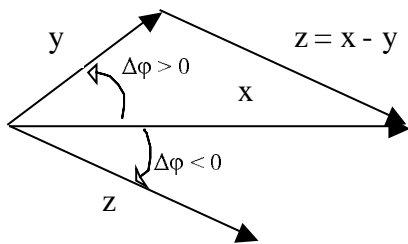
Fig. VII.3.6.2. Phase diagram of the signals measured without a wire (x), emitted by the wire (y), and measured when the wire is present (z).

VII.3.4. Conclusions

We have studied the complex transmission of the wire grids with the fill factors of 0.20 and 0.33 in the frequency range from 0.1 up to 1.6 THz with wires oriented perpendicular or parallel to the incident field polarization. In accordance with earlier observations, the agreement between experimentally measured and theoretically predicted complex transmittances is good for grids with lower fill factors f and is getting worse as f increases.

VII.4. Complex transmittance of $YBa_2Cu_3O_{6.95}$ patterned thin films

This section summarizes the results of the complex transmission measurements of the striped $YBa_2Cu_3O_{6.95}$ 80-nm films on 1-mm MgO substrates at the temperatures 25 – 300 K in the frequency range 0.1 – 1.0 THz. In order to extract the properties of the stripes material from the measured transmittances the Effective Medium Approximation have been employed.

VII.4.1. Motivation

Basic research

Mesoscopic superconductivity is a new and extremely exciting area of research. It covers superconductivity in the structures, which are smaller than 1 μm (Ref. 149,150,151), i.e. which are comparable to or shorter than the phase coherence length of the superconducting or normal conducting carriers[152]. In order to illustrate the size requirements for superconducting mesoscopic systems characteristic lengths for conventional (Al, Nb) and high temperature superconductors (YBCO) are summarized in Table VII.4.3.1.

Table VII.4.3.1. Comparison of some microscopic parameters of aluminum, niobium, and YBCO

	Al	Nb	YBCO
London penetration depth λ_L (nm) [Ref. 124]	40	50	140
coherence length ζ (nm) [Ref. 124]	550	39	1.8
mean free path of quasiparticles in the superconducting state l (nm) at T = 4.2 K			100-1000

The observation of superconducting mesoscopic phenomena in YBCO requires in principle samples with dimensions as small as nanometer. However, due to the rapid decrease of the quasiparticle scattering rate in the ab-plane of YBCO below T_c the mean free path of the unpaired carriers reaches 100-1000 nm in the ab-plane. Therefore, in patterned c-axis oriented YBCO thin films with the pattern dimensions around 1μm the scattering of the quasiparticles is expected to be different from that in solid thin films.

Applied research

YBCO thin films are used in fabrication of passive and active microwave and THz-electronic devices[153]. The microwave devices, e.g. bandpass filters, Josephson junction arrays, rapid-single-flux-quantum electronic circuits are based on patterned thin films. The dimensions of the pattern are 0.5 μm (RSFQ at 100 GHz clock rate) and 1-100 μm (filters, Josephson junctions arrays). The electromagnetic properties of μm patterned YBCO thin films like surface resistance and penetration depth are rather unexplored because conventional microwave spectroscopy is difficult to apply to patterned structures. The electromagnetic properties of patterned YBCO thin films are expected to be different from those of solid films due to the possible material degradation during the patterning process and/or mesoscopic effects.

VII.4.2. Experimental results and discussion

The $YBa_2Cu_3O_{6.95}$ films have been deposited on MgO substrate (1x10x10 mm^3) by laser ablation[154] with optical contact lithography and consequent patterning through

argon plasma etching. Parameters of the samples are presented in Table VII.4.4.1 and their structure is depicted on Fig. VII.4.4.1.

Table VII.4.4.1. Parameters of the samples

sample index	film thickness (nm)	T_c	stripes width s (μm)	structure period D (μm)
MgO1	80	84.5	5.6	7.9
MgO2		83.4		
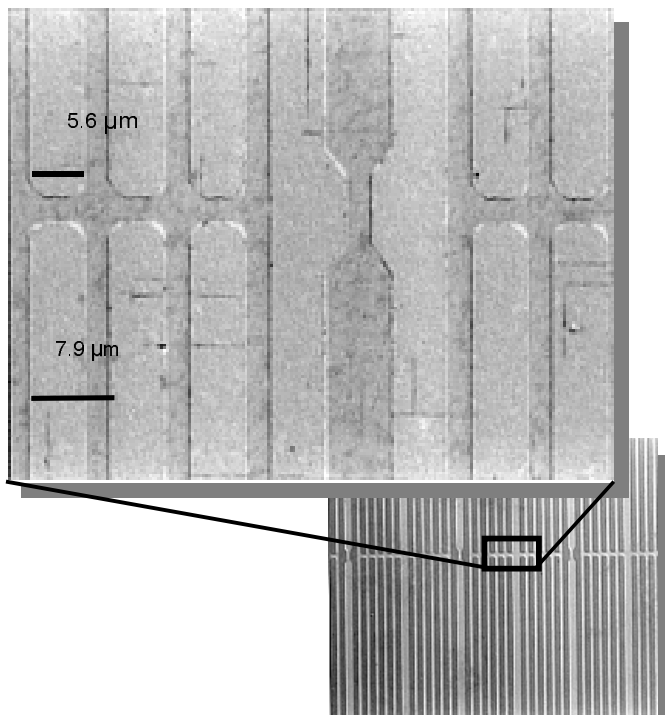
Fig. VII.4.4.1. Magnified view of samples structure

Fig.VII.4.4.2. *Time profiles of pulses transmitted through bare substrate and patterned thin film when the incident THz beam polarization oriented parallel and perpendicular to the stripes.*

Effective Medium Approximation
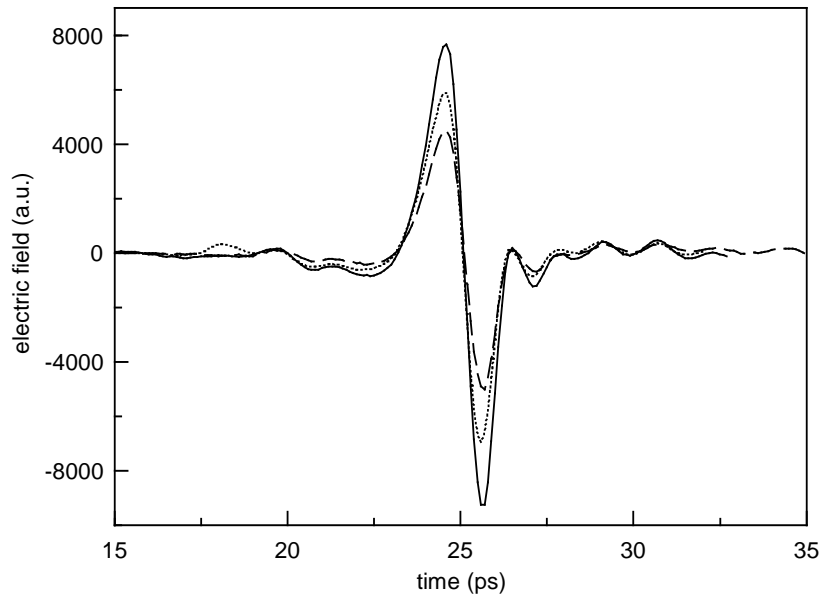
The diffraction of the THz radiation on the pattern gives rise to the strong dispersion that in the time domain manifests itself as a reshaping of transmitted pulses (Fig. VII.4.4.2).

To date, the complex transmittance of the simplest periodic structure i.e. free-standing wire grids had been studied thoroughly[155,156] (see also the references in Section VII.3). Infrared studies of planar metal strip gratings have been also reported[157]. The theory of metallic[158,159] or dielectric[160,161] gratings diffraction performance is well developed[162] and effective calculation procedures have been elaborated[163] including those for time-domain data treatment[164]. But these theories are namely diffractional i.e. they do not take the wave passed *through* a grating's material into account.

The extraction of material characteristics of a pattern structure from measured complex transmittance data is a big challenge. A rigorous approach requires the analysis of both THz radiation diffraction phenomena and transmission through the

stripes and also should take into account the Gaussian nature of the THz beam (see Chapter VI). To our knowledge, such a model is not available to date and its elaboration appears to be a serious theoretical task.

Thus, we applied a simplified model called *Effective Medium Approximation*[165,166] (EMA). Its basic principle is that a patterned structure made of *isotropic* material is treated as a solid but *anisotropic* film of the same thickness (Fig. VII.4.4.3). Naturally, the two "crystallographic" directions are chosen along and perpendicular to the stripes so that two dielectric permittivities are distinguished: for the polarization of the incident radiation collinear with the grating vector K and perpendicular to it (i.e. perpendicular and parallel to the stripes respectively). A general condition of the EMA applicability reads:

$$\frac{D}{\lambda} << \frac{1}{n_{film}} \qquad\qquad\qquad (VII.4.4.1)$$

where D is the structure period, λ is the wavelength of the incident radiation and, n_{film} is refractive index of the film's material. It can be understood like that the radiation wavelength must be optically long enough compared to the structure period so that the diffracted beams of higher orders are negligibly weak.
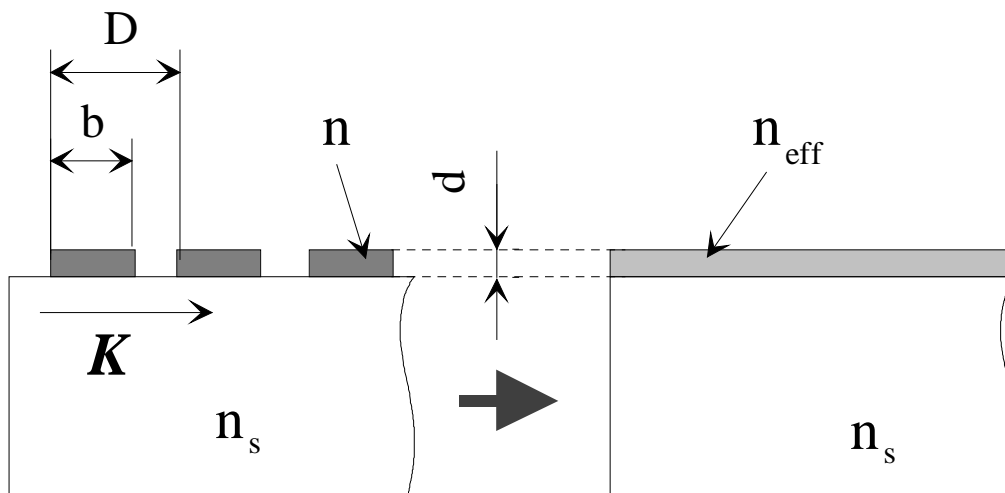
Fig VII.4.4.3. The Effective Medium Approximation.

The effective dielectric permittivities are given by the following expressions:

$$\varepsilon_{E\perp K}{}^{(2)} = \varepsilon_{E\perp K}{}^{(0)}\left[1 + \frac{\pi^2}{3}\left(\frac{D}{\lambda}\right)^2 f^2(1-f)^2 \frac{(\varepsilon-1)^2}{\varepsilon_0 \varepsilon_{E\perp K}{}^{(0)}}\right] \qquad \text{(VII.4.4.2)}$$

$$\varepsilon_{E||K}{}^{(2)} = \varepsilon_{E||K}{}^{(0)}\left[1 + \frac{\pi^2}{3}\left(\frac{D}{\lambda}\right)^2 f^2(1-f)^2(\varepsilon-1)^2 \frac{\varepsilon_{E\perp K}{}^{(0)}}{\varepsilon_0}\left(\frac{\varepsilon_{E||K}{}^{(0)}}{\varepsilon}\right)^2\right] \qquad \text{(VII.4.4.3)}$$

with the corresponding zero-order terms:

$$\varepsilon_{E\perp K}{}^{(0)} = f\varepsilon + (1-f) \qquad \text{(VII.4.4.4)}$$

$$\frac{1}{\varepsilon_{E||K}{}^{(0)}} = \frac{f}{\varepsilon} + (1-f), \qquad \text{(VII.4.4.5)}$$

where ε is the dielectric isotropic permittivity of the stripes material, $f = s/D$ is a fill factor of the structure, ε_0 is the permittivity of free space, and K is a grid vector.

Effective dielectric function of a patterned structure

The time-domain THz spectroscopic methods provide the complex transmittance of a sample that then is to be recalculated into the sample's material functions like, for example, complex index of refraction or conductivity. To apply the EMA to our results we calculated the effective dielectric permittivity spectra for the striped films, as they were solid films of the same thickness for the THz beam polarization oriented parallel or perpendicular to the stripes. The spectra calculated this way transmittances are shown on Fig. VII.4.4.4. The EMA fits (Fig. VII.4.4.5) have been performed according to the Eqs. (VII.4.4.2) - (VII.4.4.5) using the ε spectra measured separately on an $YBa_2Cu_3O_{6.95}$ solid film.
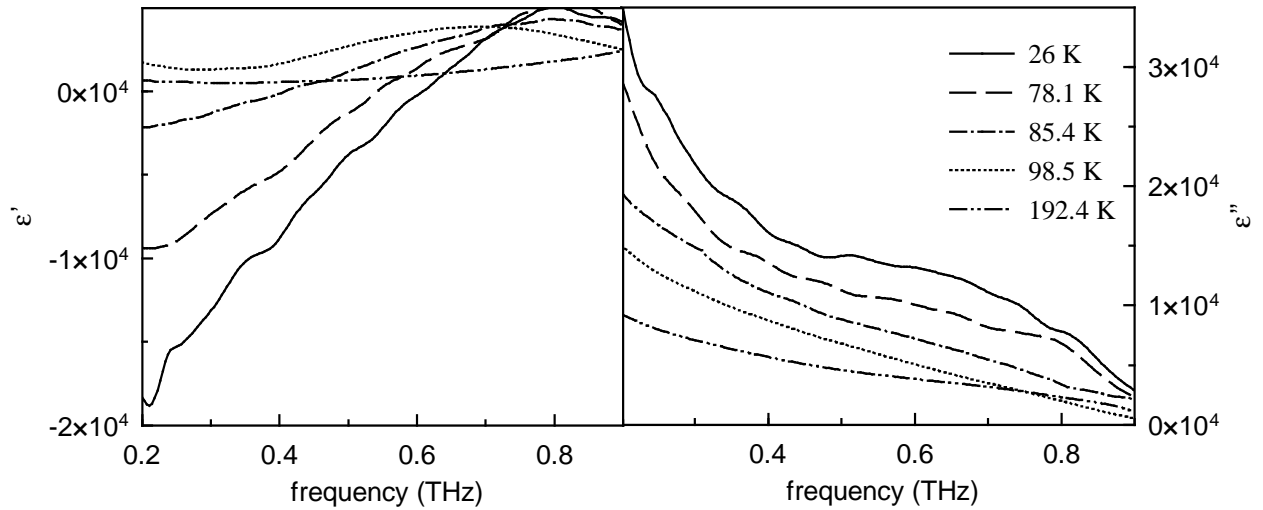
Fig VII.4.4.4. The effective complex dielectric function spectra of striped YBa$_2$Cu$_3$O$_{6.95}$ thin film.
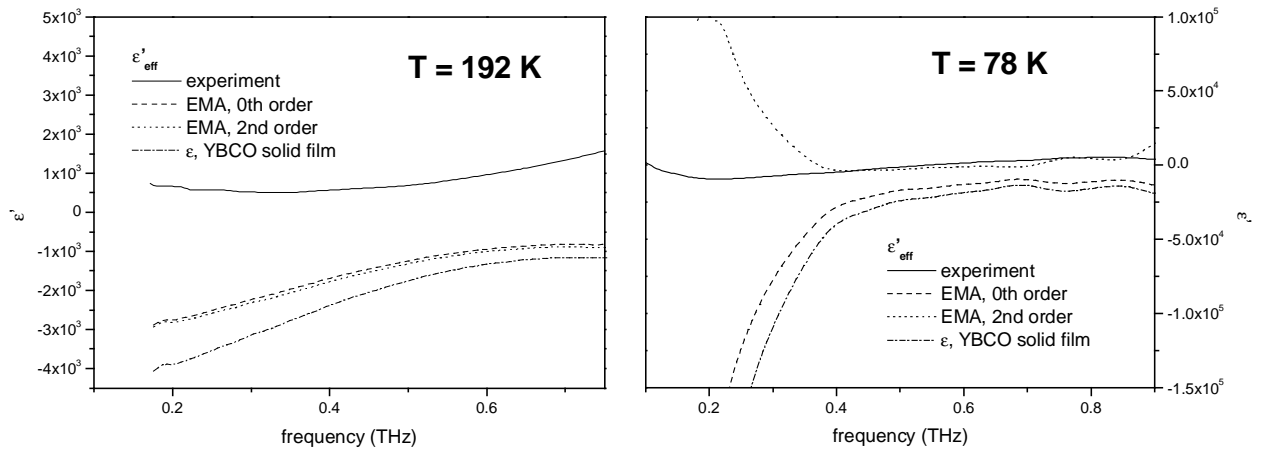
Fig. VII.4.4.5. *The real part of the effective dielectric function of a striped YBa$_2$Cu$_3$O$_{6.95}$ film compared to that of a solid film of the same composition and zero- and second order EMA fits.*

The fill factor f of the samples studied was quite high ($\sim$ 71%) so that at least at temperatures well above the T$_c$ the ε_{eff} of the striped film was of the same order of magnitude as the permittivity of the solid-film sample and could be fitted with simple zero-order EMA (VII.4.4.4) and (VII.4.4.5). But as the temperature decreases, especially when it falls below the T$_c$, zero-order fit gives values of ε_{eff} which are significantly higher than those observed experimentally. It would be too early to speak about observation of superconductivity-related dimensional effects since there could be several other reasons for such discrepancy:

- the films material could have got degraded while etched,

- the pattern of the samples used was not a set of fine parallel stripes but rather a complicated structure with some gaps in the central part i.e. where the THz beam's sensitivity reaches its maximum

- the striped structure had been elaborated from a $YBa_2Cu_3O_{6.95}$ film other than that used for reference measurements of ε to be put in EMA formulas

and, the most fundamental reason

- the refraction index of YBCO is very high at THz frequencies which makes the condition (VII.4.4.1) hard to satisfy with our values of D and λ.

The last is turning more obvious when one applies the second-order EMA (VII.4.4.2) and (VII.4.4.3). It yields ε_{eff} several times higher and of the opposite sign than measured. So, the EMA expansion is clearly divergent for our values of n_{film}, D, and λ in the THz frequency range.

VII.4.3. Conclusions

The complex transmittance of patterned thin $YBa_2Cu_3O_{6.95}$ films have been measured at frequencies from 0.1 – 1.5 THz in the temperature range from 20 to 300 K. The results have been analyzed in the framework to the Effective Medium Approximation model that considers a striped structure as a solid anisotropic effective medium. The analysis shows that the EMA in its simplest form can be hardly applied to our samples since their parameters drive us to the very edge or even beyond the area of its applicability.

VII.4.4. Outlook

On order to proceed with the study of patterned structures both theoretical and experimental difficulties should have been overcome:

To be able to describe precisely the observed behavior of the structures at THz frequencies, one should elaborate a complex theoretical model taking into account both diffractive and transmissive properties of patterned films as well as non-plane-wave nature of THz beams.

In order to apply the EMA effectively, the structures of much smaller period like tens or maximum few hundreds of nanometer and of a really fine pattern like a regular array of parallel YBCO stripes are needed. Important: the etching of the solid films must be done only after their complex conductivity have been measured.

VIII. SUMMARY

The main results of this work are briefly as folows:

- A reliable transmission time-domain terahertz spectrometer has been built. It allows measurements of complex transmittance of bulk and thin film samples of various materials in the frequency range 0.1 – 2.2 THz. The signal-to-noise ratio for a freely propagating pulse is over 1000:1 which implies that samples of the transparence as low as ~ 0.5% can already be studied with the setup. An integrated closed-cycle cryogenic system enables measurements on up to four samples at the temperatures from 25 K to 300 K.

- A completely new convertible transmission-reflection scheme of a THz spectrometer has been realized. The system allows measurements of a sample's complex transmittance as well as its complex reflectivity at the THz radiation incidence angle from 25° to 80°. A change of incident angle requires no major realignment of the spectrometer optics and takes together with measurement itself only around quarter an hour. This flexible scheme can serve as basis for many new THz experimental arrangements. Thus, the creation of a time-domain THz ellipsometer is now only a step away (see next Chapter).

- TTDTS has been successfully applied to the study of HTS thin films. The measured complex conductivity of $YBa_2Cu_3O_{6.95}$ films was analyzed in the framework of the two-fluid model with the normal carrier fraction behaving according to the Drude scenario. This allows the extraction of temperature dependent London penetration depth and quasiparticle scattering rate. The results on $Tl_2Ba_2CaCu_2O_8$ (Tl-2212) could not be fitted with simple Drude expressions so that the model in this case is either inapplicable, or has to be modified, e.g., by the introduction of more scattering rates or/and by making the rate(s) frequency dependent. At the frequencies around 1 THz and higher, Tl-2212 is characterized with unexpectedly high surface resistance. Moreover, the real part of dielectric function becomes positive at higher THz frequencies at $T < T_c$. Above the transition temperature, it stays positive in the whole frequency

range of our spectrometer. The phenomenon was also observed with traditional IR spectroscopic means and is probably caused by unusually high phonon contribution to the dielectric permittivity of the material.

IX. FUTURE WORK AND PROJECTS

IX.1. Development of new TDTS arrangements

As a very flexible experimental technique, the time-domain THz spectroscopy offers plenty of possibilities for further developments, involving the improvement of the existing arrangements and enhancement of their performance as well as the creation of brand new instrumentations. In this chapter some of such ideas and projects are presented.

IX.1.1. Time-domain THz ellipsometer

Ellipsometry is a well-developed and very precise means for surface and thin film measurements[167]. It is based on the analysis of the polarization changes, which incident light acquires as it is reflected off the surface of a sample. For the thin films study, ellipsometry allows in many cases not only the determination of optical constants but also of the film thickness on a sub-monolayer level.

Modern ellipsometers operate in the frequency range that extends from the deep UV (~200 nm) to the near-IR (~2 μm). The reflection time-domain THz spectroscopy (RTDTS, see Section V.3) is complementary to the optical ellipsometry as it covers much lower frequencies.

As the sources of electromagnetic radiation, Xe or Hg-Xe arc lamps are normally used, and the detector is typically a Si diode. In order to realize the spectroscopic ellipsometry, i.e. measurements of optical constants at various frequencies, it is necessary to employ optical filters or to change light sources and detectors. In this

respect, an advantage of RTDTS compared to conventional ellipsometry is that being a time-domain method, RTDTS provides complex reflectivity spectra immediately in a broad frequency range.

Ellipsometry is more accurate than intensity reflectance because not the absolute intensity of the reflected light but the relative change in its polarization has to be measured. It implies that ellipsometry is self-sufficient in the sense that there is no reference measurement necessary. On the other hand, the problem with reference surface, especially with its precise positioning with respect to a sample, is the major hardship for RTDTS. Therefore, the creation of an instrumentation that could combine the advantages of TDTS (broad bandwidth covering the frequencies so far unreachable for ellipsometers) and the precision of ellipsometry would be a remarkable breakthrough in the development of experimental methods of the surface science.

Basics of ellipsometry

Ellipsometry measures the change in polarization state of light reflected by the surface of a sample and relies on the difference of the reflectance for s- and p-polarized electromagnetic radiation. So, the incident light must not have any of these polarization states. A scheme of a typical ellipsometric arrangement is shown in Fig. IX.1.1.1. The unpolarized light emitted by a source passes through a polarizer that filters only one polarization. As s- and p-components of the incident light acquire different changes in their amplitude *and* phase, the linear polarization of the incident beam turns *elliptical* (Fig. IX.1.1.2), hence the name. Then the reflected light strikes an analyzer that allows only one certain polarization to pass through and reach the detector. By the rotation of the analyzer the whole polarization ellipse is read out[*].

---

[*] There are several schemes of ellipsometric measurements possible but only the one with rotating analyzer is considered here because it appears to be the best one for the use in a time-domain THz ellipsometer.

What an ellipsometer actually measures, are values Ψ and Δ which are related to the ratio of complex Fresnel reflectivities R^*_p and R^*_s:

$$\tan\Psi\exp(i\Delta) = \frac{R^*_P}{R^*_S} = \rho^*_{PS}.$$

(IX.1.1.1)

Geometrically one can interpret Ψ as the angle between one of the axes of the ellipse and the direction of incident beam polarization (Fig. IX.1.1.2.). *tan Ψ* equals to the ratio of *amplitude* reflectivities. Another ellipsometric parameter Δ is related to the ratio of the ellipse's main axes. Physically, it is a measure of a phase shift between s- and p-components due to the reflection off the sample.

In many cases, it is useful to perform several ellipsometric measurements at different incidence angles. It can help to ensure that for each wavelength Ψ and/or Δ are close to their optimum value, where the ellipsometer has maximum sensitivity. Such ellipsometric arrangement combined with the ability to measure at various frequencies is usually referred to as VASE® (Variable Angle Spectroscopic Ellipsometry*) scheme.
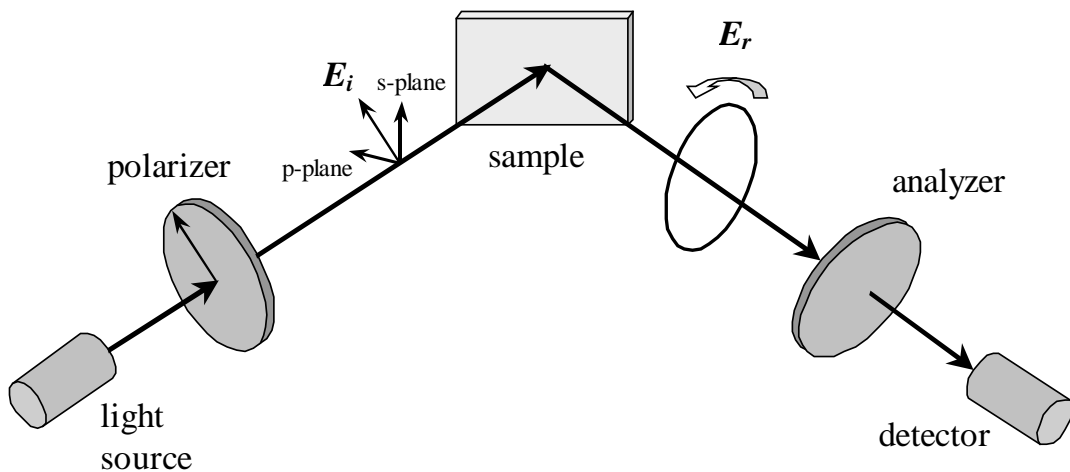
Fig. IX.1.1.1. *Geometry of an ellipsometric experiment. E$_i$ – electric field of linearly polarized incident light, E$_r$ – electric field of elliptically polarized light reflected by the sample surface.*

---

* VASE is a registered trademark of the J.A. Woollam Co., Inc.
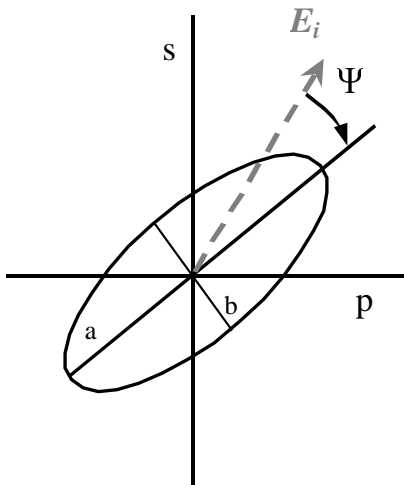
Fig. IX.1.1.2. *EM radiation polarized elliptically after the reflection off the surface of a sample. Propagation direction is perpendicular to the plane of the figure. E_i – initial linear polarization of incident light; a, b – the main axes of the polarization ellipse.*

RTDTS + VASE = TDTE !

The ratio of complex reflectivities (IX.1.1.1) is exactly the same complex function ρ^*_{PS} that is obtained in reference-free measurements with a reflection time-domain spectrometer (Eq. V.3.3.6). In the case of RTDTS, one has to measure separately the two waveforms of reflected pulses at both s- and p-polarizations. To do that, it is necessary to rotate both the emitter and the detector of THz radiation for 90° and readjust the spectrometer. In an ellipsometer, however, ρ^*_{PS} is measured without any disturbance of the light source or the detector but with a whole rotation of the analyzer.

And here comes the idea of a time-domain terahertz ellipsometer (TDTE). If having a polarization selective THz detector we were able to rotate it step-wise and to perform a scan of a THz waveform at every step, as a result we would obtain a continuous sequence of ellipses similar to that shown in Fig. IX.1.1.2 for every certain frequency from the THz spectrometer bandwidth.

In principle, a convertible THz spectrometer in its reflection configuration (see Fig. V.3.2.1) can be turned into an ellipsometer by simple turn of the THz emitter out of p-polarization and setting the receiver antenna on a rotary stage. The radiation emitted by a large aperture biased emitter is highly polarized. A dipole antenna detector has at least 90% selectivity to the polarization of the radiation detected[168]. Thus, the polarizer and analyzer could be dropped from the ellipsometer

arrangement. If the polarization selectivity of the emitter and the detector would not be sufficient, additional wire grid polarizers (see Section VII.3) could be installed after the emitter and before the detector.

But a technical realization of the scheme with rotating antenna would be very problematic. First, a sophisticated antenna holder with sliding electric contacts should be constructed. The second and the main hardship arises from the fact that an antenna is extremely sensitive to the adjustment of the optical probe beam. It is hardly possible to keep the probe beam spot focused with sub-micrometer accuracy on the photoconducting gap of the constantly rotating antenna.

The use of electro-optic sampling (EOS) detection system (Section IV.2) appears to be the right choice. An EO crystal can be easily rotated since it needs no electrical leads and the measured THz signal is not sensitive to the exact position where the probe beam strikes the crystal. Compared to an antenna detector, the EOS is somewhat less polarization selective (Fig. IX.1.1.3) so that a wire grid polarizer should be set before the crystal.

The proposed schematics of the TDTE is shown in Fig. IX.1.1.4. For setting the incidence angle, it employs the same adjustable frame as the convertible transmission-reflection THz spectrometer (CTRTS, Section V.3). It fact, the TDTE differs mechanically from the CTRTS with EOS only by the spinning holder for the EO crystal. The EO detection is arranged slightly different from that described in Section IV.2, namely the EO action is made by a probe pulse reflected from the back side if the EO crystal.

In optical ellipsometers, the analyzer is rotated at the speed of several tens of Hz and the result of the measurements is an average of hundreds of whole angular scans. In TDTE, however, the measurement sequence should be different. The EO crystal is installed on a motorized rotary stage. At every angular position of the stage, a several scans of THz waveform are made, which are then averaged and converted into a complex spectrum via the FFT routine (see Section VII.1.1). The procedure is repeated at every angular step of the rotary stage. After that, by doing a cross-section of the measured spectra, we obtain an ellipse similar to that shown in Fig. IX.1.1.2 at any frequency from the operation range.

The TDTE arrangement can be made even more flexible and enabling the reflectivity measurements at normal incidence. It can be done through integration of a *terahertz transceiver* into it, to which the next section is devoted.
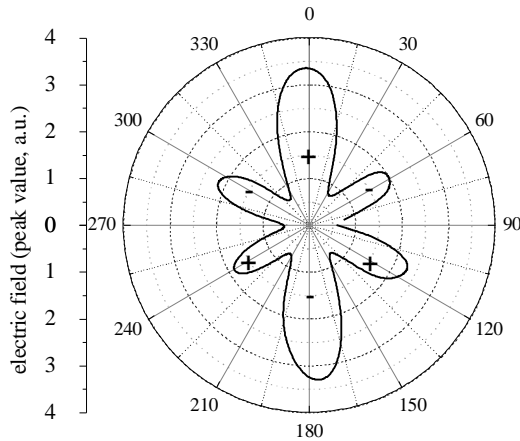
Fig. IX.1.1.3. Angular dependence the maximum of THz pulse measured with an EO crystal (ZnTe, 10x10x1 mm³). "+" and "-" indicate the sign of the main peak of a THz waveform.
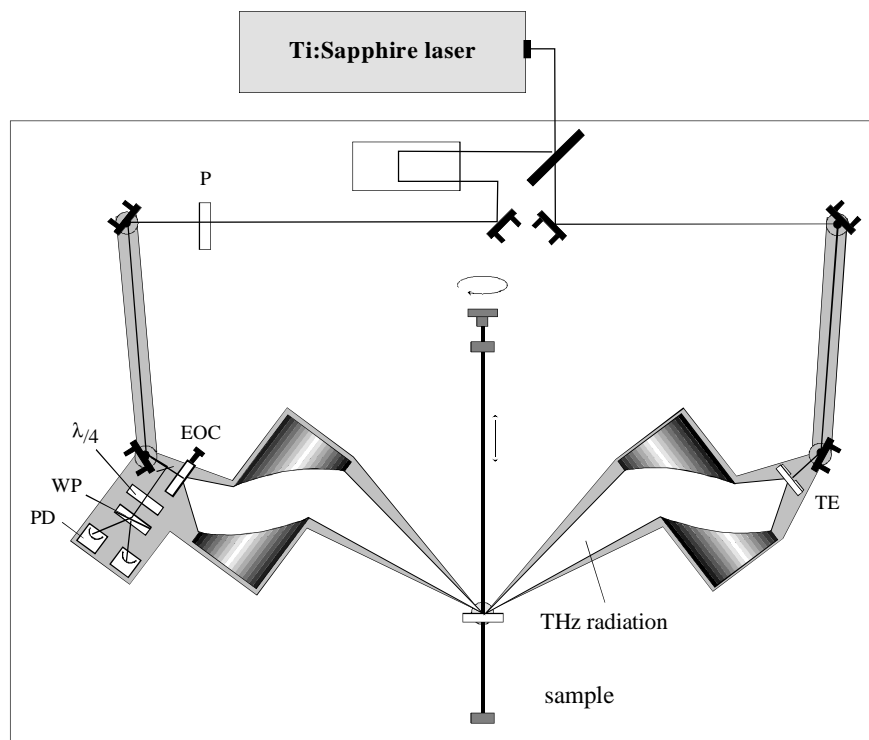
Fig. IX.1.1.4. The schematics of a time-domain THz ellipsometer (compare to Figs. V.3.1.1 and V.3.2.1). The legend: (TE) – terahertz emitter (high voltage biased semiconductor), (EOC) – electro-optic crystal, (λ/4) – quarter-wavelength plate, (WP) – Wollaston prism, (PD) – photodiode, (P) – polarizer for the optical probe beam. Other elements are identical to those of the CTRTS (Fig. V.3.1.1). The laser beam is polarized perpendicular to the plane of the picture.

IX.1.2. Terahertz transceiver

A TDTE described in the previous section solves the problem with the reference that is a serious hardship for RTDTS. What it cannot solve, is the problem of the multiple reflections within a bulk sample (or a substrate for a film). Unlike the transmission case, at an oblique incidence of THz radiation the reflections cannot be taken into account during the calculation of the sample's refractive index since they propagate different optical paths. Cutting away the reflections leads to shortening of a THz waveform and, according to Eq. VII.1.1.7, to the worsening of the frequency resolution of the spectrometer. The problem was already mentioned in Section III.3 in connection with the multiple reflections within a surface emitter. Furthermore, for the case of bulk samples, such cutting off the multiple reflections makes the precise determination of the sample thickness (Section VII.1.2) impossible.

Recently, Chen and coworkers[169] proposed a new time-domain THz arrangement that enables measurements of the complex reflectivity at the normal incidence and eliminates therefore the problem described above. They named it an *electro-optic terahertz transceiver*. Its main feature is that both THz emission and detection are made with the same EO crystal.

Fig. IX.1.2.1 shows one of the possible arrangements of a transceiver. A pump pulse travels through the EO crystal and causes a transient polarization. According to Eq. III.1.1, it results in the emission of a THz pulse whose amplitude is proportional to the second time derivative of this optically induced polarization. The emitted THz radiation is then collimated and focused on a sample by a pair of parabolic mirrors. After being reflected from the sample surface, the THz pulse travels back the same way a and reaches the EO crystal. A probe pulse is reflected by the back surface of the crystal and than propagates through it together with the THz pulse. Then follows a usual electro-optic sampling action (Section IV.2).
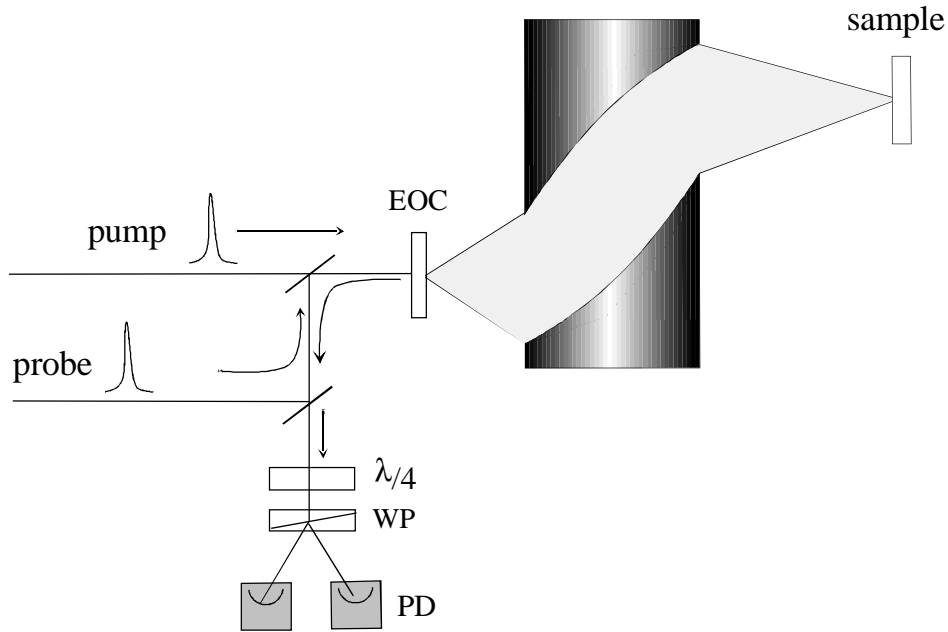
Fig. IX.1.2.1. *Schematics of an electro-optic THz transceiver. (EOC) – electro-optic crystal, (λ/4) – quarter-wavelength plate, (WP) – Wollaston prism, (PD) – photodiode. The pump and the probe beams are both s-polarized.*

Such a setup allows to acquire the THz reflectance data with the same frequency resolution as is provided by THz transmissivity measurements and to study much less transparent samples. Moreover, it makes possible the measurements on thin films, characterized by relatively low values of refractive index. As has been shown in Subsection VII.1.3, the phase shift, e.g., of a THz pulse due to the propagation through a 500 nm thick $YBa_2Cu_3O_6$ film does not exceed 50 fs which is close to the time resolution of the transmission THz spectrometer. As a result, the pulses passed trough the film on a substrate and the bare substrate look almost identical. The waveform measured in this case by a THz transceiver is, however, a superposition of the pulse reflected by the film surface and the film-substrate interface. Those time profiles have opposite phases so that the sum waveform differs significantly from the initial one[170].

The transceiver can be effectively used for THz imaging applications and contact-free surface testing. Its overall performance is, however, about 2 times lower[*] than for a conventional spectrometer with two separate crystals. The reason is that the maximum of THz emission and the maximum of the phase retardation by the EOS are reached at different angles between the laser beam (either pump or probe) and the crystallographic directions of the EO medium. So, the actual angle is trade-off between the effective THz generation and detection.

A THz transceiver can be easily integrated into the TDTE arrangement (Fig. IX.1.2.2). With the help of two flipper mirrors one can send the pump beam along the probe one. And additional delay stage must be set in the probe beam path in order to make the both probe an pump arms equally long.

In conclusion, an experimental arrangement is proposed that would enable measurements of THz transmittance, reflectance at both oblique and normal incidence (including the study of thin films with low indices of refraction and absorption), as well as ellipsometric measurements of optical constants and of the thickness of thin films.

---

[*] For (110) oriented ZnTe crystal. By other orientations the performance is even lower.
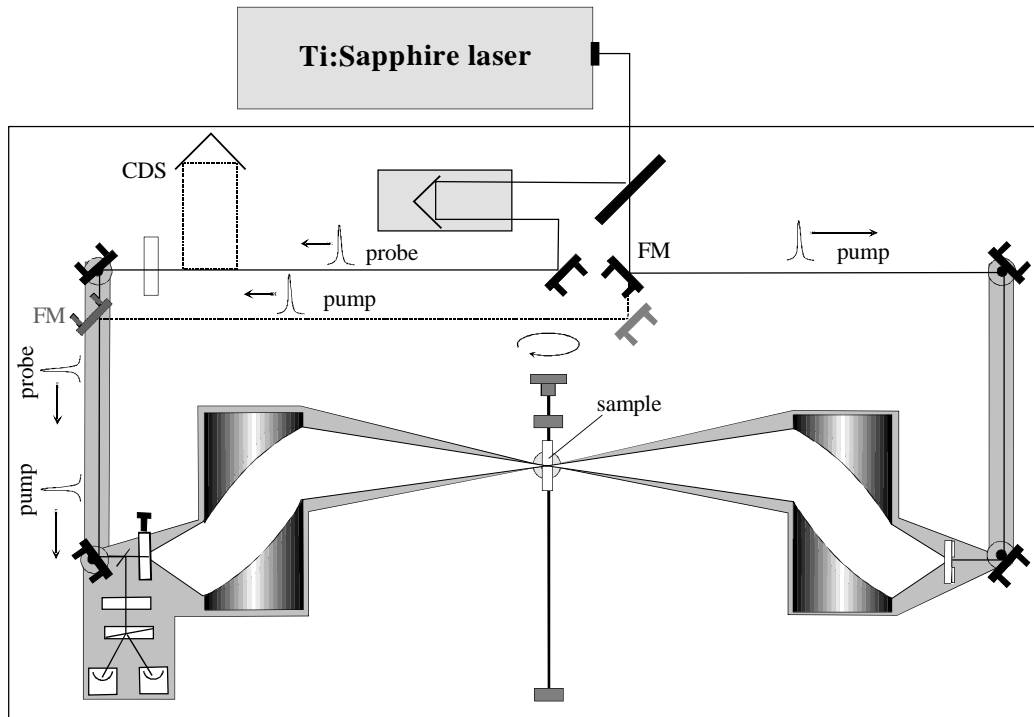
Fig. IX.1.2.2. *The three-in-one scheme combines the arrangements shown in Figs. V.3.1.1, IX.1.1.4, and IX.1.2.1. A convertible transmission-reflection THz spectrometer (CTRTS) in its reflection configuration can be used as a time-domain terahertz ellipsometer provided that both the EO crystal and the emitter are installed on rotary holders. In the transmission configuration, the CTRTS can be easily converted into a THz transceiver by sending with the help of flipper mirrors (FM) the pump beam (dashed line) along with the probe onto the EO crystal. The compensation delay stage (CDS, dotted line) ensures the equality of optical paths of the pump and probe beams for the transceiver.*

IX.2. Further study of HTS thin films

To date, THz properties of cuprate high-T_c superconductors remain to a large extent a scarcely explored area. Thus, the exact origin of the conductivity peak (Section VII.2.4) is still in the focus of lively discussions. The frequency behavior of the peak appears to be very sample-dependent, in particular, very sensitive to any doping and changes in the oxygen content or ordering (see, for example, Ref. 110). In this sense it would be interesting to investigate in detail the influence of the stoichiometry deviations on the dynamic conductivity of HTS materials.

Cuprate HTS are very anisotropic materials, and their electromagnetic properties along the *c*-axis differ drastically from those in the *ab*-plane. Thus, YBCO seems to never be in the clean limit in the *c*-direction[171]. The studies of the *c*-axis response have been reported for optical[171,172] and FIR[173] frequencies but not for THz range. In TBCCO (and related BSCCO) the extreme anisotropy and the consequent low conductivity along the *c*-direction makes possible the observation of *c*-axis plasma resonance[125] and even the interlayer Josephson Plasma Resonance[174] (JPR) at THz frequencies. In both cases, however, the measurements of *c*-axis electrodynamics reported so far have been done in indirect way, either with THz radiation propagating along the surface of the HTS film[125] or oblique incident onto the film's surface[174]. Such measurements provide therefore only the resonance frequency. As soon as corresponding *a*-axis thin films are available, a profound TDTS study of complex material functions of HTS in *c*-direction can be performed.

The knowledge of phonon structure of HTS cuprates in THz range could among other shed light on unusual behavior of dielectric function in TBCCO. In this respect it is very interesting to study THz dielectric spectra of non-superconducting members of the TBCCO family. Due to the reasons stated in Section VII.1.3, TTDTS can hardly be applied to the measurements on dielectric films with thickness below 100 nm. In this case, reflections measurements with a THz transceiver (Section IX.1.2) could provide reliable results.

ACKNOWLEDGMENTS

First of all, my great thanks go to all the people I worked together or collaborated with through these wonderful years.

Ingrid Wilke who supervised the major part of this work. I do admire her ability to spot the phenomena which were overlooked by many others and her real German diligence and perfectionism. I also appreciate her great help with my integration into German life during my first months in the country.

Prof. Jürgen Kötzler, the head of the Department of Superconductivity and Magnetism who was the official supervisor of my doctoral work. For me, he will always remain an example of a God-blessed scientist who, being an expert in his field, does not leave any other scientific area without his attention.

Petr Kužel, the founder and the leader of the THz group at the Institute of Physics in Prague where I have started to work in the field of TDTS. Being an outstandingly competent physicist and an excellent organizer, he carried me away with his personal energy. In the same time I must note his great patience that he revealed teaching me in various areas of applied physics.

Reinhold Meissner, the technician in our department who put my ideas, which were often just raw thoughts, on the paper as exact and concise technical drawings. He took the ideas of improvement of the experimental technique with a great enthusiasm and his proposals, corrections and comments were really priceless.

Chris Stevens of the Department of Engineering Science, Oxford University who provided us the samples of Tl-2212 thin films. I also appreciate his hospitality that I have enjoyed in Oxford, this scientific paradise.

Klaas Wynne of the University of Strathclyde (UK), Peter Uhd Jepsen of the Freiburg University, Ralf Rauer of the Hamburg University, Alexej Pashkin and Alexandre Deineka of the Institute of Physics in Prague for fruitful discussions about various aspects of THz spectroscopy and ellipsometry.

The guys from our department at the Institute of Applied Physics, University of Hamburg (Institut für Angewandte Physik, Universität Hamburg) who worked nearby and were always ready to help me with a fresh thought, good joke or a couple of strong hands: Frank Wiekhorst, Antonia Franke-Wiekhorst, Hanns Selig, Tobias Korn, and Dirk Dölling.

My wife Marcela Khazanová for her tender love and firm support. My parents Ludmila and Anatoli Khazans who have raised each of their five sons with so much love and care as he were the only one. I would like also to remember here my grandfather Petr Pererva († 1991) who taught me to be always curious and open to new ideas.

REFERENCES

[1] H. Mocker, R. Collins, *Mode competition and self-locking effects in a Q-switched ruby laser*, Appl. Phys. Lett. **7**, 270 (1965)

[2] C. Rullière (Ed.), *Femtosecond Laser Pulses*, Springer-Verlag, Berlin-Heidelberg, 1998

[3] D.H. Auston, *Picosecond photoconducting Hertzian dipoles*, Appl. Phys. Lett. **45**, 284 (1984)

[4] D.H. Auston and M.C. Nuss, *Electro-optical generation and detection of femtosecond electrical transients*, IEEE J. Quantum Electron. **24**, 184 (1988)

[5] M.C. Nuss, P.M. Mankiewich, M.L. O'Malley, E.H. Westerwick, and P.B. Littlewood, *Dynamic conductivity and coherence peak in YBa$_2$Cu$_3$O$_7$ superconductors*, Phys. Rev. Lett. **66**, 3305 (1991)

[6] M.C. Nuss and J. Orenstein, in *Millimeter an Submillimeter Wave Spectroscopy in Solids*, edited by G. Grüner (Topics in Applied Physics; v. 74, Springer-Verlag, Berlin Heidelberg New York, 1998), pp. 7-109

[7] D.M. Mittleman, R.H. Jakobsen, R. Neelamani, R.G. Baraniuk, and M.C. Nuss, *Gas sensing using terahertz time-domain spectroscopy*, Appl. Phys. B **67**, 379 (1998).

[8] R.A. Cheville and D. Grischkowsky, *Far-infrared foreign and self-broadened rotational linewidths of high-temperature water vapor*, J. Opt. Soc. Am. B **16**, 317 (1999).

[9] P. Kužel and J. Petzelt, *Time-resolved terahertz transmission spectroscopy of dielectrics*, Ferroelectrics 239, 949 (2000)

[10] Tae-In Jeon and D. Grischkowsky, *Characterization of optically dense, doped semiconductors by reflection THz time domain spectroscopy*, Appl. Phys. Lett. **72**, 3032 (1998).

[11] S.D. Brorson, R. Buhleier, I.E. Trofimov, J.O. White, Ch. Ludwig, F.F. Balakirev, H.-U. Habermeier, and J. Kuhl, *Electrodynamics of high-temperature superconductors investigated with coherent terahertz pulse spectroscopy*, J. Opt. Soc. Am. B **13**, 1979 (1996).

[12] I. Wilke, M. Khazan, C.T. Rieck, P. Kužel, T. Kaiser, C. Jaekel and H. Kurz, *Terahertz surface resistance of high temperature superconducting thin films*, Journal of Applied Physics **87**, 2984 (2000)

[13] R.A. Cheville, D. Grischkowsky, *Far-infrared terahertz time-domain spectroscopy of flames,* Optics Letters, 20, 1646 (1995)

[14] D.M. Mittleman, M. Gupta, R. Neelamani, R.G. Baraniuk, J.V. Rudd, M. Koch, *Recent advantages in terahertz imaging*, Appl. Phys. B 68, 1085 (1999)

[15] Proceedings of the IEEE Sixth International Conference on Terahertz Electronics, New York, NY, USA, 1998 (ISBN: 0-7803-4903-2)

[16] T. Ando, Y. Arakawa, K. Furuya, S. Komiyama, H. Nakashima, *Mesoscopic Physics and Electronics*, Springer-Verlag 1998

[17] F.W.J. Hekking, G. Schön, D.V. Averin (eds), *Mesoscopic Superconductivity*, Physica B **203**, 201 (1994)

[18] M.J.Lancaster, *Passive Microwave Device Application of HTS*, Cambridge University Press, Cambridge, England, 1997

[19] P. Kužel, M.A. Khazan and J. Kroupa, *Spatio-temporal transformations of ultrashort THz pulses*, Journal of Optical Society of America B 16, 1795 (1999)

[20] H. Selig, *Elektro-optisches Sampling von Terahertz-Pulsen,* Diploma thesis, Universität Hamburg 2000

[21] M. Khazan, R. Meissner, and I. Wilke, *Convertible transmission-reflection time-domain terahertz spectrometer*, Rev. Sci. Instr. **72**, 3247 (2001)

[22] M. Khazan, I. Wilke, C. Stevens, *Surface impedance of Tl-Bi-Ca-Cu-O films at THz frequencies*, IEEE Transactions on Applied Superconductivity **11**, 3537 (2001)

[23] D. H. Auston, and M. C. Nuss, *Electro-optical generation and detection of femtosecond electrical transients*, IEEE J. Quantum Electron., **24**, 184 (1988)

[24] P.Y. Han, M. Tani, F. Pan, X.-C. Zhang, *Use of the organic crystal DAST for terahertz beam applications*, Opt. Lett. **25**, 675 (2000)

[25] K. Kawase, M. Mizuno, S. Sohma, H. Takahashi, T. Taniuchi, Y. Urata, S. Wada, H. Tashiro, and H. Ito, Difference-frequency terahertz-wave generation from 4-dimethylamino-N-methyl-4-stilbazolium-tosylate by use of an electronically tuned Ti:sapphire laser, Optics Letters, **24**, 1065 (1999)

[26] B.B. Hu, X.-C. Zhang, D.H. Auston, P.R. Smith, *Free-space radiation from electro-optic crystals*, Appl. Phys. Lett. **56**, 506 (1990)

[27] R. Martini, G. Klose, H. G. Roskos, H. Kurz, H. T.Grahn, and R. Hey, *Superradiant emission from Bloch oscillations in semiconductor superlattices*, Phys. Rev. B, **54**, 14325 (1996)

[28] K. Wundke, U. Neukirch, J. Gutowski, and D. Hommel, *Heavy-hole-light-hole quantum beats in nonlinear transmission spectroscopy*, Phys. Rev. B 53, 10973 (1996)

[29] H. G. Roskos, M. C. Nuss, J. Shah, K. Leo, D. A. B. Miller, A. M. Fox, S. Schmitt-Rink, and K. Kohler, *Coherent submillimeter-wave emission from charge oscillations in a double-well potential*, Phys. Rev. Lett. 68, 2216 (1992)

[30] S. Hughes, D. S. Citrin, *Tunable terahertz emission through multiple Rabi flopping in a dc-biased quantum well: a new strategy*, Optics Letters 24, 1242 (1999)

[31] N.Tanichi, N. Wada, T. Nagashima, M. Tonouchi, M. Hangyo, M. Tani, B. Sakai, *Terahertz radiation from a-axis oriented YBCO thin films*, Physica C 293, 229 (1997)

[32] H. Hamster, A. Sullivan, S. Gordon, and R. W. Falcone, *Short-pulse terahertz radiation from high-intensity-laser-produced plasmas*, Phys. Rev. E 49, 671 (1994)

[33] T. Löffler, F. Jacob, and H. G. Roskos, *Generation of terahertz pulses by photoionization of electrically biased air*, Appl. Phys. Lett. **77**, 453 (2000)

[34] X.-C. Zhang, B. B. Hu, J. T. Darrow, and D. H. Auston, *Generation of femtosecond electromagnetic pulses from semiconductor surfaces*, Applied Physics Letters **56**, 1011-1013 (1990)

[35] B. B. Hu, X.-C. Zhang, and D. H. Auston, *Temperature dependence of femtosecond electromagnetic radiation from semiconductor surfaces*, Appl. Phys. **57**, 2629 (1990)

[36] X.-C. Zhang and D. H. Auston, *Optoelectronic measurement of semiconductor surfaces and interfaces with femtosecond optics*, J. Appl. Phys. **71**, 326 (1992)

[37] D. You, R. R. Jones, P. H. Bucksbaum, D. R. Dykaar, *Generation of high-power sub-single-cycle 500-fs electromagnetic pulses*, Opt. Lett. **18**, 290 (1993)

[38] C.W. Siders, J.L.W. Siders, A.J. Taylor, S.-G. Park, M.R. Melloch, A.M. Weiner, *Generation and characterization of terahertz pulse trains from biased, large-aperture photoconductor*, Opt. Lett., **24**, 241 (1999)

[39] H. Ibach, H. Lüth, *Feskörperphysik*, 3. Auflage, Springer (1993)

[40] M. Born and E. Wolf, *Principles of Optics*, 7th ed., Cambridge University Press, Cambridge, 1999, p. 87

[41] J.T. Darrow, X.-C. Zhang, D.H. Auston, J.D. Morse, *Saturation properties of large-aperture photoconducting antennas*, IEEE J. Quantum Electron **28**, 1607 (1992)

[42] N. Sarukura, H. Ohtake, S. Izumida, and Z. Liu, *High average-power THz radiation from femtosecond laser-irradiated InAs in a magnetic field and its elliptical polarization characteristics*, J. Appl. Phys. **84**, 654 (1998)

[43] D. H. Auston, A. M. Johnson, P. R. Smith, and J. C. Bean, *Picosecond optoelectronic detection, sampling, and correlation measurements in amorphous semiconductors*, Appl. Phys. Lett. **37**, 371 (1980)

[44] H. Hertz, Ann. d. Physik **36**, 1 (1889); see also Ref. 42, p. 84, 730

[45] K.-H. Hellwege, *Einführung in die Festkörperphysik*, Springer-Verlag, Berlin, Heidelberg, 1994

[46] H. Němec, P. Kužel, A. Pashkin, M. Khazan, S. Schnüll, and I. Wilke, *Carrier dynamics in low-temperature grown GaAs studied by THz emission spectroscopy*, J. Appl. Phys. **90**, 1303 (2001)

[47] D.H. Auston, *Ultrafast Optoelectronics* in *Ultrafast Laser Pulses: Generation an Applications*, Ed. W. Kaiser, Topics in Applied Physics vol. 60, Springer-Verlag, 1993

[48] M. Schall, *Aufbau eines Terahetrz-Spectrometers und Bestimmung optischer Eigenschaften von Materialen im Frequenzbereich zwischen 100 GHz und 1.5 THz*, Diploma thesis, Albert-Ludwigs University, Freiburg im Breisgau, 1996

[49] *Handbook of Optical Constants of Solids*, Ed. E.D. Palik, Academic Press, 1985

[50] M. C. Nuss, D. H. Auston, and F. Capasso, *Direct subpicosecond measurement of carrier mobility of photoexcited electrons in gallium arsenide*, Phys. Rev. Lett. **58**, 2355 (1987)

[51] A.G. Markelz and E. J. Heilweil, *Temperature-dependent terahertz output from semi-insulating GaAs photoconductive switches*, Appl. Phys. Lett. **72**, 2229 (1998)

[52] T. Korn, *Femtosekunden-Spektroskopie an LT-GaAs und Microcavities*, Diploma thesis, University of Hamburg, 2000

[53] G. Rodriguez, A. J. Taylor, *Screening of the bias field in terahertz generation from photoconductors*, Opt. Lett., **21**, 1046 (1996)

[54] J.-H. Son, T. B. Norris, J. F. Whitaker, *Terahertz electromagnetic pulses as probes for transient velocity overshoot in GaAs and Si*, J. Opt. Soc. Am. B **11**, 2519 (1994)

[55] D. Krökel, D. Grischkowsky, and M. B. Ketchen, *Subpicosecond electrical pulse generation using photoconductive switches with long carrier lifetimes*, Appl. Phys. Lett. **54**, 1046 (1989)

[56] X.-C. Zhang, J. T. Darrow, B. B. Hu, D. H. Auston, M. T. Schmidt, P. Tham, and E. S. Yang, *Optically induced electromagnetic radiation from semiconductor surfaces*, Appl. Phys. Lett. **56**, 2228 (1990)

[57] N. Katzenellenbogen and D. Grischkowsky, *Efficient generation of 380 fs pulses of THz radiation by ultrafast laser pulse excitation of a biased metal-semiconductor interface*, Appl. Phys. Lett. **58**, 222 (1991)

[58] V.L. Bonch-Bruevich, S.G. Kalashnikov, *The Physics of Semiconductors*, 2nd ed., Nauka, Main Editorial board for Physical and Mathematical Literature, Moscow, 1990 (in Russian)

[59] J. Shah, *Ultrafast Spectroscopy of Semiconductors and Semiconductor Nanostructures*, Springer, Berlin, 1996

[60] D. Côté, J. M. Fraser, M. DeCamp, P. H. Bucksbaum, H. M. van Driel, *THz emission from coherently controlled photocurrents in GaAs*, Appl. Phys. Lett., **75**, 3959 (1999)

[61] P.U. Jepsen, private communication (2001).

[62] H.G. Roskos, *Time-resolved terahertz spectroscopy – an overview*, Lithuanian Journal of physics **34**, 175 (1994)

[63] S.-G. Park, M.R. Melloch, and A.M. Weiner, *Comparison of terahertz waveforms measured by electro-optic and photoconductive sampling*, Appl. Phys. Lett. **73**, 3184 (1998)

[64] J. A. Valdmanis, G. A. Mourou, and C. W. Gabel, *Subpicosecond electrical sampling*, IEEE J. Quant. El. **QE-19**, 664 (1983)

[65] P. U. Jepsen, C. Winnewisser, M. Schall, V. Schyja, S. R. Keiding, and H. Heim, *Detection of THz pulses by phase retardation in lithium tantalate*, Phys. Rev. E **53**, 3052 (1996)

[66] Q. Wu and X.-C. Zhang, *Free-space electro-optic sampling of terahertz beams*, Appl. Phys. Lett. **67**, 3523 (1995)

[67] Q. Wu and X.-C. Zhang, *Ultrafast electro-optic field sensors*, Appl. Phys. Lett., **68**, 1604 (1996)

[68] A. Nahata, D. H. Auston, and T. F. Heinz, *Coherent detection of freely propagating terahertz radiation by electro-optic sampling*, Appl. Phys. Lett., **68**, 150 (1996)

[69] B.E.A. Saleh and M.C. Teich, *Fundamentals of photonics*, John Wilez & Sons, Inc., New York, 1991

[70] C. Winnewisser, *Elektrooptische Detektion von ultrakurzen elektromagnetischen Pulsen*, PhD thesis, Albert-Ludwigs-Universität Freiburg i. Brsg., 1999

[71] J. Herrmann, *Theory of Kerr-lens mode locking: role of self-focusing and radially varying gain*, J. Opt. Soc. Am. B **11**, 498 (1994)

[72] C. Hirlimann, *Pulsed Optics*, in *Femtosecond Laser Pulses*, Ed. C. Rulliere, Springer, 1998

[73] Tsunami, Mode-Locked Ti:sapphire Laser. User's manual, Spectra-Physics, 1995

[74] M. Born, E. Wolf, *Principles of Optics*, 7th ed., Cambridge University Press, Cambridge, 1999, p. 200

[75] M.E. Parks, *High Frequency Electrodynamics of the Cuprate Superconductors in the Vortex State*, PhD thesis, University of California at Berkeley, 1995

[76] *Coolstar Coldheads, Installation and Operation Manual*, Edwards High Vacuum International, 1991

[77] S. Spielman, B. Parks, J. Orenstein, D.T. Nemeth, F. Ludwig, J. Clarke, P. Merchant, and D.J. Lew, *Observation of the quasiparticle Hall effect in superconducting $YBa_2Cu_3O_{7-delta}$*, Phys. Rev. Lett. 73, 1537 (1994).

[78] Q. Chen and X.-C. Zhang, *Polarization modulation in optoelectronic generation and detection of terahertz beams*, Appl. Phys. Leet. **74**, 3435 (1999)

[79] D.M. Mittleman, M. Gupta, R. Neelamani, R.G. Baraniuk, J.V. Rudd, and M. Koch, *Recent advantages in terahertz imaging*, Appl. Phys. B 68, 1085 (1999).

[80] D.M. Mittleman, S. Hunsche, L. Boibin, and M.C. Nuss, *T-ray tomography*, Opt. Lett. 22, 904 (1997).

[81] S.C. Howells and L.A. Schlie, *Transient terahertz reflection spectroscopy of undoped InSb from 0.1 to 1.1 THz*, Appl. Phys. Lett. 69, 550 (1996).

[82] P.P. Woskov, D.R. Cohn, S.C. Han, A. Gatesman, R.H. Giles, and J. Waldman, *Precision terahertz relative reflectometry using a blackbody source and heterodyne receiver*, Rev. Sci. Instrum. 65, 438 (1994).

[83] E.D. Palik (Ed.), *Handbook of Optical Constants of Solids*, Academic Press, 1985

[84] M. Born, E. Wolf, *Principles of Optics*, 7th ed., Cambridge University Press, Cambridge, 1999, p. 42

[85] D. Grischkowsky, private communication (2000).

[86] R.W. Ziolkowski and J.B. Judkins, *Propagation characteristics of ultrawide-bandwidth pulsed Gaussian beams*, JOSA A **9**, 2021-2030 (1992)

[87] A.E. Kaplan, *Diffraction-induced transformation of near-cycle and subcycle pulses*, J. Opt. Soc. Am B **15**, 951-956 (1998)

[88] P.U. Jepsen, R.H. Jacobsen, and S.R. Keiding, *Generation and detection of terahertz pulses from biased semiconductor antennas,* J. Opt. Soc. Am. B **13**, 2424 (1996).

[89] D. You and P.H. Bucksbaum, *Propagation of half-cycle far infrared pulses*, J. Opt. Soc. Am. B **14**, 1651 (1997).

[90] S. Feng, H.G. Winful, and R.W. Hellwarth, *Gouy shift and temporal reshaping of focused single-cycle electromagnetic pulses*, Opt. Lett. **23**, 385 (1998)

[91] A. Gürtler, C. Winnewisser, H. Helm, P.U. Jepsen, *Terahertz pulse propagation in the near field and the far field*, J. Opt. Soc. Am. A, **17**, 74 (2000)

[92] H. Kogelnik, and T. Li, Appl. Opt. **5**, 1550 (1966).

[93] D. H. Auston, K. P. Cheung, and P. R. Smith, *Picosecond photoconducting Hertzian dipoles,* Appl. Phys. Lett. **45**, 284–286 (1984).

[94] B.B. Hu, J.T. Darrow, X.-C. Zhang, D.H. Auston, and P.R. Smith, *Optically steerable photoconducting antennas*, Appl. Phys. Lett., **56**, 886 (1990)

[95] R.T. Hall, D. Vrabec, and J.M. Dowling, *A high-resolution, far infrared double-beam lamellar grating interferometer*, Appl. Opt. **5**, 1147 (1966)

[96] W.H. Press, B.P. Flannery, S.A. Teukolsky, W.T. Vetterling, *Numerical Recipes in Pasca.The Art of Scientific* Computing, Cambridge University Press, 1989

[97] The PKGraph © 1998-2001 by P. Kužel, e-mail: kuzelp@fzu.cz

[98] A. Pashkin, E. Buixaderas, P. Kužel, M.-H. Liang, C.-T. Hu, I-N. Lin, *THz transmission spectroscopy applied to dielectrics and microwave ceramics*, Ferroelectrics **254**, 113 (2001)

[99] L. Duvillaret, F. Garet, and J.-L. Coutaz, *Highly Precise Determination of Optical Constants and Sample Thickness in Terahertz Time-Domain Spectroscopy*, Applied Optics, **38**, 409-415 (1999)

[100] A.C.S. Van Heel (Ed.), *Advanced Optical Techniques*, North-Holland, Amsterdam, 1967, p. 268

[101] M.C. Nuss, P.M. Mankiewich, M.L. O'Malley, E.H. Westerwick, and P.B. Littlewood, *Dynamic conductivity and coherence peak in $YBa_2Cu_3O_7$ superconductors*, Phys. Rev. Lett. **66**, 3305 (1991)

[102] J.G. Bednorz and K.A. Müller, Z. Phys. B **64**, 189 (1986)

[103] M. A. Hein, *High temperature superconducting thin films at microwave frequencies*, in Springer Tracts in Modern Physics vol. 155, G. Höhler, Ed., Heidelberg: Springer, 1999.

[104] M. Kenward, *Superconductors get ready to transform industry*, Physics World, June 1996

[105] M. J. Lancaster, *Passive microwave device application of HTS*, Cambridge, University Press, 1997

[106] A.P. Bramley, J.D. O'Connor, and C.R.M. Grovenor, *Thallium-based HTS thin films, processing, properties and applications*, Supercond. Sci. Technol. **12**, R57 (1999)

[107] M. N. Eddy, J. Z. Sun, R. D. Hammond, L. Drabeck, I. B. Ferreira, K. Holczer *et al.*, J. Appl. Phys. **70**, 496 (1991)

[108] G.B. Lubkin, *Power applications of high-temperature superconductors*, Physics Today, March 1996

[109] D.A. Bonn, R. Liang, T.M. Riseman, D.J. Baar, D.C. Morgan, K. Zhang, P. Dosanjn. T.L. Duty, A. MacFarlane, G.D. Morris, J.H. Brewer, W.N. Hardy, C. Kallin, and A.J. Berlinsky, *Microwave determination of the quasiparticle scattering time in $YBa_2Cu_3O_{6.95}$*, Phys. Rev. B **47**, 111314 (1993)

[110] I. François, C. Jaekel, G. Kyas, D. Dierickx, O. Van der Bies, R.M. Heeres, V.V. Moshchalkov, Y. Bruynseraede, H.G. Roskos, G. Borghs, H. Kurz, *Influence of Pr doping and oxygen deficiency on the scattering behavior of $YBa_2Cu_3O_7$ thin films*, Phys. Rev. B **53**, 12502 (1996)

[111] N. Dieckmann, R. Kürsten, M. Löhdorf, A. Bock, *Epitaxial quality of c-axis and a-axis oriented $YBa_2Cu_3O_7$ films. Characterization by Raman spectroscopy*, Pysica C **245**, 212 (1995)

[112] A. Hosseini, R. Harris, S. Kamal, P. Dosanjn, J. Preston, R. Liang, W.N. Hardy, and D.A. Bonn, *Microwave spectroscopy of thermally excited quasiparticles in $YBa_2Cu_3O_{6.99}$*, Phys. Rev. B **60**, 1449 (1999)

[113] S. Hensen, G. Müller, C.T. Rieck and K. Scharnberg, *In-plane surface impedance of epitaxial $YBa_2Cu_3O_{7-\delta}$ films: Comparison of experimental data taken at 87 GHz with d- and s-wave models of superconductivity*, Phys. Rev. **56**, 6237-6264 (1997)

[114] M.C. Nuss, P.M. Mankiewich, M.L. O'Malley, E.H. Westerwick, and P.B. Littlewood, *Dynamic conductivity and coherence peak in $YBa_2Cu_3O_7$ superconductors*, Phys. Rev. Lett. **66**, 3305-3308 (1991)

[115] C. Ludwig, Q. Jiang, J. Kuhl, J. Zegenhagen, *Electrodynamic properties of oxygen reduced $YBa_2Cu_3O_{7-x}$ thin films in the THz regime*, Physica C, **269** (1996), 249-254

[116] A. Frenkel, F. Gao, Y. Liu, J. F. Whitaker, and C. Uher, S. Y. Hou and J. M. Phillips, *Conductivity peak, relaxation dynamics, and superconducting gap of YBa2Cu3O7 studied by terahertz and femtosecond optical spectroscopies*, Phys. Rev. B **54**, 1355-1365 (1996)

[117] F. Gao, G.L. Garr, C.D. Porter, D.B. Tanner, G.P.Williams, C.J. Hirschmugl, B. Dutta, X.D. Wu, and S. Etemad, *Quasiparticle damping and the coherence peak in $YBa_2Cu_3O_{7-\delta}$*, Phys. Rev. B **54**, 700 (1996)

[118] A.Pimenov, A.Loidl, G.Jakob, H.Adrian, *Optical conductivity in $YBa_2Cu_3O_{7-\delta}$ thin films*, Phys. Rev. B **59**, 4390 (1999)

[119] P.C. Hammel, M. Takigawa, R.H. Heffener, Z. Fisk, and K.C. Ott, Phys. Rev. Lett. **63**, 1992 (1989)

[120] C. T. Rieck, K. Scharnberg, and J. Ruvalds, *Microwave spectra of d-wave superconductors*, Physical Review **60**, 12432-12442 (1999)

[121] C.J. Gorter and H.G.B. Casimir, Z. Phys. **35**, 963 (1934)

[122] M. Sigrist and K. Ueda, Rev. Mod. Phys. 63, 239 (1991)

[123] P. Monthoux and D. Pines, Phys. Rev. B 47, 6069 (1993)

[124] R. Buhleier, S.D. Brorson, I.E. Trofimov, J.O. White, H.-U. Habermeier, and J. Kuhl, *Anomalous behavior of the complex conductivity of $Y_{1-x}Pr_xBa_2Cu_3O_7$ observed with THz spectroscopy*, Phys. Rev. B, **50**, 9672 (1994)

[125] R. Mallozzi, J. Corson, J. Orenstein, J.N. Eckstein and I. Bozovic, *Terahertz conductivity and c-axis plasma resonance in $Bi_2Sr_2CaCu_2O_{8+\delta}$*, J.Phys.Chem. Solids, **59,** 2095 (1998)

[126] Ch.P. Poole, Jr., H.A. Farach, R.J. Creswick, *Superconductivity*, Academic Press, San Diego CA, 1995

[127] D.B. Tanner, H.L. Liu, M.A. Quijada, A.M. Zibold, H. Berger, r.j. Kelley, M. Onellion, F.C. Chou, D.C. Johnston, J.P. Rice, D.M. Ginsberg, J.T. Markert, *Superfluid and normal fluid density in high-T_c superconductors*, Physica B **244**, 1 (1998)

[128] A. Schilling, F. Hulliger, and H.R. Ott, *In-plane London penetration depths near the critical temperature of $Tl_2Ba_2Ca_{n-1}Cu_nO_{2n+4}$ and $(Bi, Pb)_2Sr_2Ca_{n-1}Cu_nO_{2n+4}$*, Z. Phys. B **82**, 9 (1991)

[129] B. A. Willemsen, K. E. Kihlstrom, T. Dahm, D. J. Scalapino, B. Gowe, D. A. Bonn et al., *Microwave loss and intermodulation in $Tl_2Ba_2CaCu_2O_8$ thin films*, Phys. Rev. B **58**, 6650 (1998)

[130] R. B. Hammond, G. V. Negrete, L. C. Bourne, D. D. Strother, A. H. Cardona, M. M. Eddy, *Epitaxial $Tl_2Ba_2CaCu_2O_8$ thin films with low 9.6 GHz surface resistance at high power and above 77 K*, Appl. Phys. Lett. **57**, 825 (1990)

[131] W. L. Holstein, L. A. Parisi, Z.-Y. Shen, C. Wilker, M. S. Brenner, J. S. Martens, *Surface resistance of large-area $Tl_2Ba_2CaCu_2O_8$ thin films at microwave and millimeter wave frequencies measured by three noncavity techniques*, J. Supercond. **6**, 191 (1993)

[132] S. Huber, M. Manzel, H. Bruchlos, S. Hensen, G. Müller, *Thallium-based high-T_c films with very low surface impedance*, Physica C **244**, 337 (1995)

[133] J. D. O'Connor, A. P. Jenkins, D. Dew-Hughes, M. J. Goringe, C. M. R.Grovenor, *Microstructural and microwave characterization of low temperature processed $Tl_2Ba_2CaCu_2O_8$ thin films*, IEEE Trans. Appl. Supercond. **7**, 1899 (1997)

[134] J. Halbritter, *On surface resistance of superconductors*, Z. Physik **266**, 209 (1974)

[135] M.C. Nuss, K.W. Goosen, P.M. Mankiewich, M.L. O'Malley, J.L. Marshall, and R.E. Howard, IEEE Trans. Magn. **27**, 863 (1991)

[136] C.M. Foster, K.F. Voss, T.W. Hagler, D. Mihailović, A,J. Heeger, M.M. Eddy, W.L. Olson, and S.J. Smith, *Infrared reflection of epitaxial $Tl_2Ba_2CaCu_2O_8$ thin films in the normal and superconducting states,* Solid. State Comm. **76**, 651 (1990)

[137] A.M. Zibold, D.M. Tanner, H. Berger, *Far-infrared study of superconducting $Tl_2Ba_2CaCu_2O_8$*, Physica B **244**, 27 (1998)

[138] C. Thomsen and M. Cardona, in *Physical Properties of High-Temperature Superconductors* (D. Ginsberg, Ed.), Vol. 1, Chap. 8, World Scientific, Singapore, 1989

[139] M.A. Geitz, *Investigation of the transverse and longitudinal beam parameters at the TESLA test facility linac*, DESY-thesis-1999-033, ISSN 1435-8085 (1999)

[140] C.L. Mok, W.G. Chambers, T.J. Parker, A.E. Costley, *The far-infrared performance and application of free-standing grids wound from $5\mu m$ diameter tungsten wire*, Infrared Physics **19**, 437 (1979).

[141] J.A.Beunen, A.E.Costley, G.F.Neill, C.L.Mok, T.J.Parker, G.Tait, *Performance of free-standing grids wound from 10-μm-diameter tungsten wire at submillimeter wavelengths: computations and measurements*, J. Opt. Soc. Am. **71** 184 (1981).

[142] A.A. Volkov, B.P. Gorshunov, A.A. Irisov, G.V. Kozlov, and S.P. Lebedev, *Electrodynamic properties of plane wire grids*, Int. J. of Infrared and Millimeter Waves **3**, 19 (1982)

[143] W.G. Chambers, T.J. Parker, A.E. Costley, *Freestanding fine-wire grids for use in millimeter and submillimeter-wave spectroscopy*, Infrared and Millimeter Waves **16**, p.77, ed. K. Button, Academic Press 1986.

[144] J.B. Davies, IEEE Trans. Microwave Theory Tech. **21**, 99 (1973)

[145] R. Petit, *Electromagnetic theory of gratings*, Springer, Berlin, 1980

[146] W.G. Chambers, C.L. Mok, T.J. Parker, *Theoretical studies of the frequency response of some far-infrared interferometers with wire-grid beam dividers*, J. Phys. D: Appl. Phys. **13**, 515 (1980).

[147] Wynne, K., Jaroszynsky, D.A., *Superluminal terahertz pulses*, Opt.Lett, **24**, 25 (1999)

[148] K. Wynne, J.J. Carey, J. Zawadzka, D.A. Jaroszynsky, *Tunneling of single-cycle terahertz pulses through waveguides*, Optics communications **176**, 429 (2000)

[149] F.W.J. Hekking, G. Schön, D.V. Averin (Eds.), *Mesoscopic Superconductivity*, Physica B **203**, 201 (1994)

[150] C. Bruder, Superconductivity Review 1, 261 (1996)

[151] C.J. Lambert, R. Raimondi, J. Phys.: Condens. Matter **10**, 901 (1998)

[152] T. Ando, Y. Arakawa, K. Furuya, S. Komiyama, H. Nakashima, *Mesoscopic Physics and Electronics*, Springer, 1998

[153] M.J. Lancaster, *Passive Microwave Device Application of HTS*, Cambridge University Press, Cambridge, England, 1997

[154] J.K. Heinsohn, D. Reimer, A. Richter, K.-O. Subke, and M. Schilling, Physica C **245**, 212 (1995)

[155] W.G.Chambers, C.L.Mok, T.J.Parker, *Theory of the scattering of electromagnetic waves by a regular grid of parallel cylindrical wires with circular cross section*, J. Phys. A: Math. Gen. **13**, 1433 (1980).

[156] R. Petit, *Electromagnetic grating theories: limitations and successes*, Nouv. Rev. Optique **6**, 129 (1975).

[157] T. Schimert, R. Magnusson, *Diffraction from metal strip gratings with high spatial frequency in the infrared spectral region*, J. Opt. Soc. Am. A **7**, 1719 (1990)

[158] M.G. Moharam, T.K. Gaylord, *Rigorous coupled-wave analysis of metallic surface-relief gratings*, J. Opt. Soc. Am. A **3**, 1780 (1986).

[159] J.J. Kuta, H.M. van Driel, D. Landheer, Y. Feng, *Coupled-wave analysis of lamellar metal transmission for the visible and the infrared*, J. Opt. Soc. Am. A **12**, 1118 (1995)

[160] M.G. Moharam, T.K. Gaylord, *Diffraction analysis of dielectric metallic surface-relief gratings*, J. Opt. Soc. Am. **72**, 1385 (1982)

[161] R. Petit, G. Tayeb, *Theoretical and numerical study of gratings consisting of periodic arrays of thin and lossy strips*, J. Opt. Soc. Am. A **7**, 1686 (1990)

[162] T.K. Gaylord and M.G. Moharam, *Analysis and applications of optical diffraction by gratings*, Proc. of the IEEE **73**, 894 (1985).

[163] M. McClure, D. Kralj, T.-T. Hsu, L. Caren, L.B. Felsen, *Frequency-domain scattering by nonuniform truncated arrays: wave-oriented data processing for inversion and imaging*, J. Opt. Soc. Am. A **10**, 2675 (1994)

[164] D. Kralj, M. McClure, L. Caren, L.B. Felsen, *Time-domain wave-oriented data processing of scattering by nonuniform truncated gratings*, J. Opt. Soc. Am. A **10**, 2685 (1994)

[165] S.M. Rytov, *Electromagnetic properties of a finely stratified medium*, Sov. Phys. JETP **2**, 466 (1956)

[166] D.H. Raguin and G.M. Morris, *Antireflection structured surfaces for the infrared spectral region*, Appl. Optics, **32**, 1154 (1993)

[167] R.M.A. Azzam and M. Bashara, *Ellipsometry and polarized light*, North-Holland Publishing Company, 1977

[168] Y. Cai, I. Brener, J. Lopata, J. Wynn, L. Pfeiffer, and J. Federici, *Design and performance of singular electric field terahertz photoconducting antennas*, Appl. Phys. Lett. **71**, 2076 (1997)

[169] Q. Chen, M. Tani, Z. Jiang, and X.-C. Zhang, *Electro-optic transceivers for terahertz-wave applications*, J. of Opt. Soc. Am. B **18**, 823 (2001)

[170] M. Li, G.C. Cho, T.-M. Lu, X.-C. Zhang, S.-Q. Walg, and J.T. Kennedy, *Time-domain dielectric constant measurement of thin film in GHz-THz frequency range near the Brewster angle*, Appl. Phys. Lett. 74, 2113 (1999)

[171] J. Schützmann, S. Tajima, S. Miyamoto, and S. Tanaka, *C-axis optical response of fully oxygenated $YBa_2Cu_3O_{7-\delta}$: observation of dirty-limit-like superconductivity and residual unpaired carriers*, Phys. Rev. Lett. **73**, 174 (1994)

[172] C.C. Homes, T. Timusk, D.A. Bonn, R. Liang, and W.N. Hardy, *Optical properties along the c-axis of $YBa_2Cu_3O_{6+x}$ for x = 0.50 -> 0.95: evolution of the pseudogap*, Physica C **254**, 265 (1995)

[173] C. Bernhard, R. Henn, A. Wittlin, M. Kläser, Th. Wolf, G. Müller-Vogt, C.T. Lin, and M. Cardona, *Electronic c-axis response of $Y_{1-x}Ca_xBa_2Cu_3O_{7-\delta}$ studied by far-infrared ellipsometry*, Phys. Rev. Lett. **80**, 1762 (1998)

[174] V.K. Thorsmølle, R.D. Averitt, M.P. Maley, L.N. Bulaevskii, C. Helm, and A.J. Taylor, *Observation of the Josephson plasma resonance in $Tl_2Ba_2CaCu_2O_8$ using THz spectroscopy, International Terahertz Workshop*, Sandbjerg Castle, Danmark, 17-20 September 2000